PATIENT-SPECIFIC ORTHOPEDIC IMPLANT DESIGN AND PRODUCTION WITH TISSUE ENGINEERING METHOD

A THESIS SUBMITTED TO
THE GRADUATE SCHOOL OF NATURAL AND APPLIED SCIENCES
OF
MIDDLE EAST TECHNICAL UNIVERSITY

BY

SENEM BÜYÜKSUNGUR

IN PARTIAL FULFILLMENT OF THE REQUIREMENTS
FOR
THE DEGREE OF DOCTOR OF PHILOSOPHY
IN
BIOTECHNOLOGY

SEPTEMBER 2019

Approval of the thesis:

PATIENT-SPECIFIC ORTHOPEDIC IMPLANT DESIGN AND PRODUCTION WITH TISSUE ENGINEERING METHOD

submitted by **SENEM BÜYÜKSUNGUR** in partial fulfillment of the requirements for the degree of **Doctor of Philosophy in Biotechnology Department, Middle East Technical University** by,

Prof. Dr. Halil Kalıpçılar
Dean, Graduate School of **Natural and Applied Sciences** _____

Assoc. Prof. Dr. Can Özen
Head of Department, **Biotechnology** _____

Prof. Dr. Vasıf Hasırcı
Supervisor, **Dept. of Biological Sciences, METU** _____

Prof. Dr. Nesrin Hasırcı
Co-Supervisor, **Dept. of Chemistry, METU** _____

Examining Committee Members:

Prof. Dr. Cemil Yıldız
Dept. of Orthopedics and Traumatology, SBU _____

Prof. Dr. Vasıf Hasırcı
Dept. of Biological Sciences, METU _____

Prof. Dr. Kezban Ulubayram
Dept. of Pharmaceutical Sciences, Hacettepe University _____

Prof. Dr. Ayşen Tezcaner
Dept. of Engineering Sciences, METU _____

Assoc. Prof. Dr. İrem Erel Göktepe
Dept. of Chemistry, METU _____

Date: 03.09.2019

I hereby declare that all information in this document has been obtained and presented in accordance with academic rules and ethical conduct. I also declare that, as required by these rules and conduct, I have fully cited and referenced all material and results that are not original to this work.

Name, Surname: Senem Büyüksungur

Signature :

ABSTRACT

PATIENT-SPECIFIC ORTHOPEDIC IMPLANT DESIGN AND PRODUCTION WITH TISSUE ENGINEERING METHOD

Büyüksungur, Senem
Doctor of Philosophy, Biotechnology
Supervisor: Prof. Dr. Vasıf Hasırcı
Co-Supervisor: Prof. Dr. Nesrin Hasırcı

September 2019, 128 pages

Customized and patient specific, tissue engineered constructs are needed for the treatment of irregular shaped bone defects. This study presents the preparation of two different 3D printed scaffolds. 1) PCL-based scaffolds modified with nanohydroxyapatite (HAp) and poly(propylene fumarate) (PPF), and 2) Cell carrying hybrid scaffolds of PCL/GelMA.

3D printed, PCL-based scaffolds were coated with HAp or HAp/PPF before cell seeding and their presence enhanced osteoconductivity and compressive mechanical strength of the scaffold, respectively. Cytotoxicity, irritation and implantation tests showed the biocompatibility of the scaffolds. These scaffolds were implanted into femurs of rabbits either with or without seeding Rabbit Bone Marrow Stem Cells (BMSCs). Bone regeneration was studied with micro CT, and mechanical and histological tests after 4 and 8 weeks of implantation. Tissue regeneration on BMSC seeded PCL/HAp/PPF scaffolds was improved significantly, and after 8 weeks of implantation, compressive and tensile stiffness of femurs (394±25 and 463±10 N/mm) were significantly higher than that of the healthy rabbit femur (316±10 and 392±10 N/mm). The results demonstrate compatibility of the scaffold with bone, and the

potential of the scaffold for use in the production of patient-specific implants for effective bone regeneration.

PCL/GelMA hybrid scaffolds were fabricated by printing the polymers side-by-side. The compressive moduli of the scaffolds (102±10 MPa) were comparable with that of human trabecular bone (50–100 MPa). Dental pulp stem cells (DPSCs) were loaded in GelMA and printed between PCL fibers. After printing, 90% of DPSCs were alive and mineralized nodules were observed on day 21 demonstrating osteogenic differentiation.

Keywords: PCL, Poly(propylene fumarate), GelMA, 3D printing, Bone tissue engineering.

ÖZ

DOKU MÜHENDİSLİĞİ YÖNTEMİ İLE HASTAYA ÖZEL ORTOPEDİK İMPLANT TASARIMI VE ÜRETİMİ

Büyüksungur, Senem
Doktora, Biyoteknoloji
Tez Danışmanı: Prof. Dr. Vasıf Hasırcı
Ortak Tez Danışmanı: Prof. Dr. Nesrin Hasırcı

Eylül 2019, 128 sayfa

Kişiselleştirilmiş ve hastaya özel doku mühendisliği ürünleri düzensiz kemik hasarlarını tedavi etmek için gereklidir. Bu çalışma, 3B basılmış iki farklı doku iskelesinin hazırlanışını sunmaktadır. 1) PCL bazlı, nanohidroksiapatit (HAp) ve poli(propilen fumarat) (PPF) ile modifiye edilmiş iskeleler ve 2) Hücre taşıyan 3B basılmış PCL/GelMA hibrid iskeleler.

3B basılmış PCL bazlı iskeleler, HAp veya HAp/PPF ile kaplanmış ve bu kaplamalar sırasıyla osteokondüktiviteyi ve basma mekanik dayanımını arttırmıştır. Sitotoksisite, irritasyon ve implantasyon testleri iskelelerin biyouyumlu olduklarını kanıtlamıştır. Bu iskeleler tavşan kemik iliği kök hücreleri (BMSC) eklenerek ve eklenmeyerek tavşan femurlarına implante edilmiştir. Kemik rejenerasyonu, implantasyon sonrası 4. ve 8. haftalarda mikro BT, mekanik testler ve histolojik açıdan incelenmiştir. BMSC ekilmiş PCL/HAp/PPF iskelelerinin doku rejenerasyonunu oldukça arttırdığı ve implantasyondan 8 hafta sonra implante edilmiş femurların basma ve çekme direngenlik değerlerinin (394 ve 463 N/mm), sağlıklı tavşan femurunun basma ve çekme direngenlik değerinden (316 ve 392 N/mm) anlamlı derecede yüksek olduğu gözlenmiştir. Bu sonuçlar iskelelerin kemik ile uyum içinde olduğunu ve kemik rejenerasyonu için hastaya özgü iskelelerin üretiminin potansiyelini ortaya koymuştur.

PCL/GelMA 3B hibrid iskeleler, her iki polimerin yan yana basılmasıyla üretilmiştir. Bu iskelelerin basma elastik modülü (102±10 MPa) insan trabeküler kemiğiyle (50-100 MPa) karşılaştırılabilir düzeydedir. Diş Pulpa Kök Hücreleri (DPSC) GelMA içerisine yüklenmiş ve PCL fiberler arasına basılmıştır. Basımdan sonra, DPSC hücreleri % 90 oranında canlı kalmış ve 21. günde osteojenik farklılaşmayı gösteren mineralize olmuş nodüller gözlenmiştir.

Anahtar Kelimeler: PCL, Poli(propilen fümarat), GelMA, 3B basım, Kemik doku mühendisliği.

Dedicated to my beloved family, Arda and Çınar Büyüksungur

ACKNOWLEDGMENTS

I would like to express my special thanks and gratitude to my thesis supervisor, Prof. Dr. Vasıf Hasırcı for his continuous guidance, support, encouragement and insight throughout my thesis. I am grateful for his patience, time and effort he has spent to improve my scientific experience.

I am very grateful to my co-supervisor Prof. Dr. Nesrin Hasırcı who has been a significant role model to me and has kind consideration regarding my academic requirements. I was fortunate for her mentoring and valuable advices.

I would also like to thank my thesis monitoring committee members, Prof. Dr. Kezban Ulubayram and Assoc. Prof. Dr. İrem Erel Göktepe for all their collaboration, suggestions, and useful discussions.

I am grateful for all the support that I have received from Seher Büyüksungur. I would like to express my special thanks to İnan Büyüksungur who gave me endless love and made me feel his precious little girl. I would like to thank Anıl Büyüksungur for his friendship and great moments we have shared with.

I offer my deepest blessings to my family. I owe my deepest gratitude to my mother Seval Heper, my father Ali Heper and my precious beloved brother Ogün Heper for their endless love and continuous help in every possible way. I feel very lucky to be raised in their hands.

I would like to express my deepest love and blessings to my loving husband, Arda Büyüksungur for his endless love, patience, support, and understanding. He is all what I desire in my life, my best friend, my family, and the best gift of my life. I would like to thank my lovely baby, Çınar Büyüksungur who gives me the most precious moments in my life.

I gratefully acknowledge TUBITAK for BIDEB 2211-C Ph.D. scholarship and 1003 research fellowship (213M708) programmes.

TABLE OF CONTENTS

ABSTRACT v

ÖZ vii

ACKNOWLEDGEMENTS x

TABLE OF CONTENTS xi

LIST OF TABLES xv

LIST OF FIGURES xvi

LIST OF ABBREVIATIONS xx

CHAPTERS

1. INTRODUCTION 1

1.1. Structure of Bone 1

1.2. Bone Cells 3

1.3. Mechanical Properties of Bone 5

1.4. Bone Repair and Regeneration Mechanism 6

1.5. Clinical Needs and Current Treatments in Bone Replacement Therapy 8

1.5.1. Conventional Treatments 8

1.5.2. Bone Tissue Engineering 8

1.5.2.1. Cells 9

1.5.2.2. Scaffolds 11

1.6. Approach, Aim, and Novelty of The Study 21

2. MATERIALS AND METHODS 25

2.1. Materials 25

2.2. Methods 26

2.2.1. Synthesis and Characterization of Polypropylene fumarate (PPF) 26
2.2.2. PCL Scaffold Fabrication by 3D Plotting 27
2.2.3. Preparation of PCL/HAp and PCL/HAp/PPF Composite Scaffolds 28
2.2.4. Synthesis and Characterization of Methacrylated Gelatin (GelMA) 29
2.2.5. GelMA Slab Preparation 30
2.2.6. Hybrid Scaffold Fabrication by 3D Printing 30
2.2.7. Physical and Chemical Characterization of the Scaffolds 32
2.2.7.1. Scanning Electron Microscopy (SEM) Analysis 32
2.2.7.2. Micro Computed Tomography (Micro CT) Analysis 32
2.2.7.3. Contact Angle Measurements 32
2.2.7.4. Mechanical Analysis 32
2.2.7.5. Evaluation of *In situ* Degradation 33
2.2.7.6. Equilibrium Water Content (EWC) of GelMA Hydrogels 34
2.2.8. *In Vitro* Studies 34
2.2.8.1. Determination of Cytotoxicity of PCL, PCL/HAp and PCL/HAp/PPF Scaffolds 34
2.2.8.2. Isolation of Bone Marrow Mesenchymal Stem Cells (BMSCs) and Dental Pulp Stem Cells (DPSCs) 36
2.2.8.3. Characterization of Dental Pulp Stem Cells (DPSCs) with Flow Cytometry 36
2.2.8.4. BMSC Seeding on PCL, PCL/HAp and PCL/HAp/PPF Scaffolds ... 37
2.2.8.5. Preparation of L929 Loaded 3D Bioprinted GelMA Hydrogels 37
2.2.8.6. Preparation of DPSC Loaded, 3D Bioprinted PCL/GelMA Hybrid Scaffolds 38

2.2.8.7. Determination of BMSC Proliferation on PCL, PCL/HAp and PCL/HAp/PPF Scaffolds....38
2.2.8.8. Determination of Osteoblastic Differentiation....38
2.2.8.9. Microscopical Studies....41
2.2.9. *In vivo* Studies....42
2.2.9.1. *In vivo* Biocompatibility Tests....42
2.2.9.2. Orthotopic Implantation of PCL, PCL/HAp and PCL/HAp/PPF scaffolds....44
2.2.10. Statistical Analysis....47
3. RESULTS AND DISCUSSION....49
3.1. 3D Printed PCL, PCL/HAp, and PCL/HAp/PPF Scaffolds....49
3.1.1. Poly(propylene) fumarate (PPF) Characterization....49
3.1.2. Physical and Chemical Characterization of the Scaffolds....50
3.1.3. Evaluation of *In Situ* Degradation....55
3.1.4. Mechanical Analysis....56
3.1.5. *In Vitro* Studies....58
3.1.5.1. Cytotoxicity of the Scaffolds....58
3.1.5.2. BMSCs Proliferation on The Scaffolds....59
3.1.5.3. SEM Analysis of BMSCs on 3D Scaffolds....61
3.1.5.4. Osteogenic Differentiation....62
3.2. 3D Printed GelMA and PCL/GelMA Hybrid Scaffolds....68
3.2.1. ^{1}H-NMR of GelMA....68
3.2.2. Microscopic Evaluation of PCL/GelMA Hybrid Scaffolds....69
3.2.3. *In situ* Degradation....71

3.2.4. Equilibrium Water Content (EWC) of GelMA 72
3.2.5. Compressive Mechanical Test 73
3.2.6. *In vitro* studies 74
3.2.6.1. Flow Cytometry of DPSCs 74
3.2.6.2. L929 Fibroblast Loaded, 3D Printed GelMA Scaffolds 75
3.2.6.3. DPSC Loaded, 3D Printed PCL/GelMA Hybrid Scaffolds 77
3.3. *In vivo* Studies 81
3.3.1. *In vivo* Biocompatibility Tests 81
3.3.1.1. Intracutaneous Irritation Test 81
3.3.1.2. Implantation Test 81
3.3.2. Evaluation of *In vivo* Bone Tissue Regeneration 84
3.3.2.1. Micro CT Analysis 84
3.3.2.2. Biomechanical Analysis 86
3.3.2.3 Histological Analysis 88
4. CONCLUSION 91
REFERENCES 93
A. L929 ALAMAR BLUE CALIBRATION CURVE 121
B. BMSCs ALAMAR BLUE CALIBRATION CURVE 122
C. ALP CALIBRATION CURVE 123
D. ETHICS COMMITTEE REPORT FOR DPSC ISOLATION 124
E. ETHICS COMMITTEE REPORT FOR *IN VIVO* STUDIES 125
CURRICULUM VITAE 127

LIST OF TABLES

TABLES

Table 1.1. Extracellular Matrix Proteins in Bone. 3
Table 1.2. Mechanical properties of human compact and trabecular bones. 6
Table 2.1. Real-time PCR primer details. 41
Table 3.1. Scores of *in vivo* biocompatibility tests of PCL, PCL/HAp and PCL/HAp/PPF scaffolds. 83

LIST OF FIGURES

FIGURES

Figure 1.1. Structure and organization of the long bone. 2
Figure 1.2. Specific cell types of bone. 4
Figure 1.3. Schematic representation of femur fracture healing. 7
Figure 1.4. Self-renewal, proliferation, and potential lineage specific differentiation pathways of MSCs. 10
Figure 1.5. Stages of manufacturing patient-specific implants. 16
Figure 1.6. Additive manufacturing techniques. 18
Figure 1.7. 3D Bioprinting methods. 20
Figure 2.1. The synthesis of polypropylene fumarate. 26
Figure 2.2. Schematic representations of the organization of the B and BS (0.10, 0.15, 0.20, 0.25 and 0.50 mm) PCL scaffolds in cross sectional views. 27
Figure 2.3. Schematic presentation of the PCL based 3D scaffold fabrication process. 28
Figure 2.4. The binding of methacrylate groups to the primary NH_2 groups of gelatin. 29
Figure 2.5. Schematic representation of 3D Hybrid scaffold fabrication. 31
Figure 2.6. Crosslinking mechanism of GelMA by UV radiation in the presence of Irgacure 2959. 31
Figure 2.7. Subcutaneous injection regions in the dorsal area of the rabbits. 43
Figure 2.8. Implantation of scaffold into the femur of a New Zealand rabbit. 44
Figure 2.9. Four point bending test of rabbit femurs. 46
Figure 3.1. FTIR spectra of uncrosslinked (UN-XL) and crosslinked (XL) PPF..... 50
Figure 3.2. Physical characterization of 3D printed B (0 mm) and BS (shifted 0.10, 0.15, 0.20, 0.25, 0.50 mm) PCL scaffolds. 52

Figure 3.3. Physical and chemical characterization of the PCL, PCL/HAp and PCL/HAp/PPF scaffolds designed in BS 0.15 form. 54
Figure 3.4. Weight loss of BS 0.15 scaffolds of PCL, PCL/HAp and PCL/HAp/PPF in aqueous lipase solution (180 U/L) in 35 days (n=3). 55
Figure 3.5. Stress-strain curves of A) PCL, B) PCL/HAp and C) PCL/HAp/PPF scaffolds before and after gamma irradiation (n=5).....56
Figure 3.6. Compressive modulus of PCL (B and BS 0.15), and BS 0.15 scaffolds of PCL/HAp and PCL/HAp/PPF (n=5). 57
Figure 3.7. Cytotoxicity of PCL, PCL/HAp and PCL/HAp/PPF scaffolds using fibroblasts (L929) in accordance with ISO 10993-5 using the extracts after incubation of the scaffolds in the complete medium at 37^{o}C for 24 h (n=3). Control: L929 fibroblasts grown in DMEM High medium. Statistical analysis was carried out by using one-way ANOVA. ns: not significant. 58
Figure 3.8. The change in the number of BMSC on PCL scaffolds (B and BS 0.15) as determined by Alamar cell viability test (n=3). 60
Figure 3.9. Viability of BMSC on PCL, PCL/HAp and PCL/HAp/PPF scaffolds as determined by Alamar cell viability test (n=3). 60
Figure 3.10. SEM of BMSCs seeded scaffolds. 62
Figure 3.11. Stereomicrographs of the PCL, PCL/HAp and PCL/HAp/PPF scaffolds stained with Alizarin Red.....63
Figure 3.12. ALP concentration of BMSCs on PCL, PCL/HAp and PCL/HAp/PPF scaffolds (n=3). 64
Figure 3.13. Quantitative RT-PCR results for RUNX2 gene expression of the BMSCs on PCL, PCL/HAp and PCL/HAp/PPF scaffolds (n=3). 66
Figure 3.14. Quantitative RT-PCR results for COL1A1 gene expression of the BMSCs on PCL, PCL/HAp and PCL/HAp/PPF scaffolds (n=3). 67
Figure 3.15. Quantitative RT-PCR results for SPP1 gene expression of the BMSCs on PCL, PCL/HAp and PCL/HAp/PPF scaffolds (n=3). 68
Figure 3.16. ^{1}H-NMR spectra of A) gelatin, and B) uncrosslinked gelatin methacrylamide (GelMA). 69

Figure 3.17. Stereomicrograph and SEM micrographs of PCL/GelMA hybrid scaffold. 70
Figure 3.18. MicroCT images of PCL/GelMA hybrid scaffold. 70
Figure 3.19. *In situ* degradation of 3D printed PCL/GelMA (10x10x1.5 mm^3), 3D printed GelMA scaffolds (10x10 x1.5 mm^3) and GelMA slabs (diameter: 10 mm, height: 1.5 mm) in PBS at 37ºC (n=3). 71
Figure 3.20. Equilibrium water content of 3D printed GelMA, PCL/GelMA scaffolds and slab GelMA after 24 h incubation in distilled water (n=3). 72
Figure 3.21. Compressive modulus of 3D printed GelMA, PCL and PCL/GelMA scaffolds (n=5). 73
Figure 3.22. Flow cytometry analysis of the expression of surface markers by DPSCs stained with CD45, CD31, antimouse IgG1 isotype control, CD90 and CD105 antibodies along with the controls (n=3). 75
Figure 3.23. Live/Dead Assay of L929 fibroblast loaded GelMA, studied with CLSM. 76
Figure 3.24. Live/Dead Assay of DPSC loaded PCL/GelMA, studied with CLSM. 77
Figure 3.25. Phalloidin staining of DPSC loaded PCL/GelMA, studied with CSLM. 78
Figure 3.26. Stereomicrographs of the Alizarin Red staining of DPSC loaded PCL/GelMA and the control (cell free PCL/GelMA). Black arrow heads show CaP deposition. 79
Figure 3.27. EDS analysis of the Alizarin Red staining of DPSC loaded PCL/GelMA on days 7, 14 and 21. 80
Figure 3.28. Evaluation of *in vivo* bone tissue regeneration with Micro CT images of the rabbit femurs at the end of 4 and 8 weeks after implantation. 85
Figure 3.29. Bone mineral density (BMD) values of the the newly formed bone in untreated empty defect (control), the scaffold implanted defects and healthy bone (control). (n_{empty}=3, $n_{scaffold\ implanted}$=4) 86
Figure 3.30. Stiffness values of the femurs at the position of compression at 4 and 8 weeks (n=4). 87

Figure 3.31. Stiffness values of the femurs at the position of tension at 4 and 8 weeks (n=4).....87
Figure 3.32. Histological study of the BMSCs seeded and unseeded PCL/HAp and PCL/HAp/PPF scaffolds (both BS 0.15) after 4 weeks of implantation.....88

LIST OF ABBREVIATIONS

3D	3 Dimensional
ALP	Alkaline Phosphatase
AM	Additive Manufacturing
ANOVA	One-Way Analysis of Variance
AR	Alizarin Red
B	Basic printing
BMP	Bone Morphogenetic Protein
BMSCs	Bone Marrow Mesenchymal Stem Cells
BS	Basic Shift printing
BSA	Bovine Serum Albumin
CAD/CAM	Computer Aided Design/Computer Aided Manufacturing
CLSM	Confocal Laser Scanning Microscope
COL1A1	Collagen Type I
CT	Computed Tomography
DCM	Dichloromethane
DM	Degree of Methacrylation
DMEM	Dulbecco's Modified Eagle Medium
DMSO	Dimethyl Sulfoxide
DPSCs	Dental Pulp Stem Cells
ECM	Extracellular Matrix

EDS	Energy Dispersive X-ray spectroscopy
FBS	Fetal Bovine Serum
FDA	Food and Drug Administration
FDM	Fused Deposition Modeling
FITC	Fluorescein Isothiocyanate
GelMA	Methacrylated Gelatin
HAp	Hydroxyapatite
^{1}H-NMR	^{1}H-Nucleic Magnetic Resonance
Irgacure 2959	2-(Hydroxyl)-4-(2-hydroxyethoxy)-2-methylpropiophenone
MRI	Magnetic Resonance Imaging
MSCs	Mesenchymal Stem Cells
PBS	Phosphate Buffer Saline
PCL	Poly(ε-caprolactone)
Pen/Strep	Penicillin/Streptomycin
PFA	Paraformaldehyde
PPF	Poly(propylene fumarate)
RGD	Arginine-Glycine-Aspartic Acid Sequence
RUNX2	Runt-Related Transcription Factor 2
SEM	Scanning Electron Microscopy
SPP1	Osteopontin
WCA	Water Contact Angle

CHAPTER 1

INTRODUCTION

1.1. Structure of Bone

Bone is a highly specialized form of connective tissue and it is a dynamic organ which serves several important functions in human body such as providing mechanical support, protection of the internal organs, being a metabolic reservoir of minerals for systemic mineral homeostasis, regulation of blood pH, the housing of multiple progenitor cells and also the production of blood (Porter et al., 2009).

Bone can be classified as cortical (compact) bone (80% of the total mass of the skeleton) and cancellous (trabecular) bone (20% of the total mass of the skeleton). Cortical bone is denser with a low degree of porosity (5-10%) and found at the outer region of bones. In contrast, cancellous bone has a porosity of around 50-90% and is located mostly in the inner cavity of bones. The structure of human femur which is a long bone is presented in Figure 1.1. The cortical bone consists of basic structural unit called Haversian system or osteons. Each osteon has concentric rings of lamellae which are composed of mineralized collagen fibrils. They are located around a central canal, the Haversian canal, which contains blood vessels and nerves that service the bone. There are spaces (lacuna) between the rings where osteocytes (mature bone cells) are located. Nutrients and waste products are transported by microscopic channels, called canaliculi. Conversely, the structure of cancellous bone is a lattice of thin plates, called trabeculae. The cavities between trabeculae are filled with bone marrow.

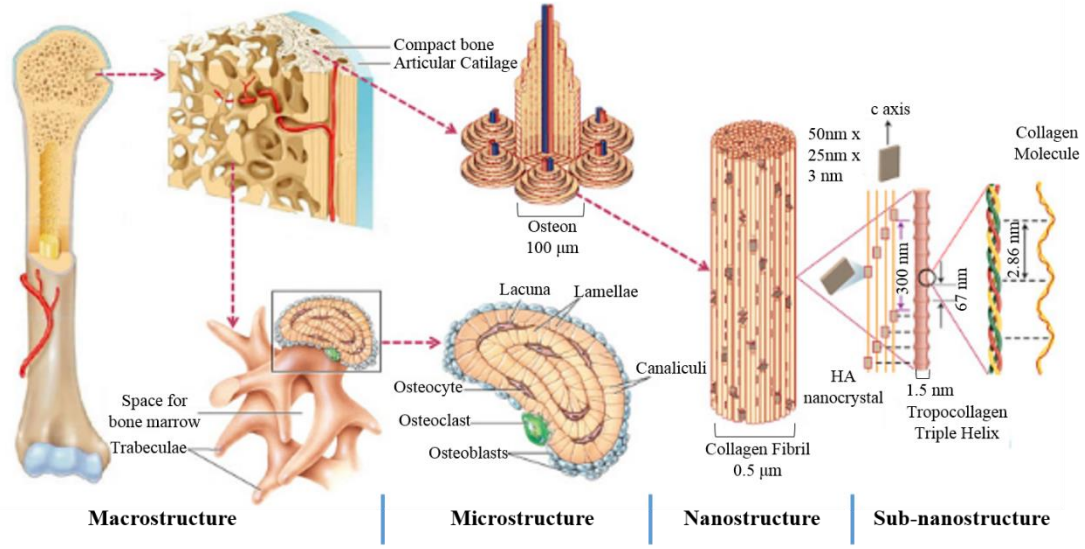

Figure 1.1. Structure and organization of the long bone.
(Adapted from Wang et al., 2016).

Bone has both organic and inorganic phases. The organic phase (20-25% of the dry weight) is composed of collagen fibers (mainly collagen type I, but also type III and type V) and other noncollagenous proteins (glycoproteins, growth factors and bone specific proteoglycans). The organic phase provides the elasticity, and fracture toughness to the bone matrix. The collagenous and noncollagenous proteins present in the extracellular matrix of the bone and important roles in bone remodeling and osteogenesis are presented in Table 1.1.

Inorganic phase (65-75% of the dry weight) of the bone is mainly calcium phosphate crystals in the form of hydroxyapatite (HAp) with a molecular formula of $Ca_{10}(PO_4)_6(OH)_2$. The HAp crystals in the collageneous matrix give the hardness and rigidity to the structure and enhance the mechanical strength of the bone.

Table 1.1. *Extracellular Matrix Proteins in Bone.*
(Adapted from Lindahl et al., 2015).

Collagenous protein	**Function**
Type I	Binds and orientates other proteins
Type III	Trace, may regulate collagen fibril diameter
Type V	Trace, may regulate collagen fibril diameter
Noncollagenous protein	**Function**
Alkaline Phosphatase	Hydrolyzes inhibitors of mineral deposition; Increases local PO_4 concentration
Osteonectin	Regulates collagen organization and growth factors; May regulate HAp deposition
Hyaluronan	May define space destined to ossify
Osteocalcin	Regulates osteoclasts; Inhibits mineralization; May coordinate bone turnover
Thrombospondin	Enhance cell attachment; Binds to collagens, platelets, thrombin, fibrinogen, laminin, plasminogen, and PAI
Fibronectin	Enhance cell attachment; Binds to fibrin, heparin, gelatin, collagens
Vitronectin	Enhance cell attachment; Binds: collagens, plasminogen, PAI, heparin
Osteopontin	Binds to cells, controls proliferation; May regulate mineralization; Inhibits nitric oxide synthase
Bone sialoprotein	Binds to cells; May initiate mineralization
Albumin	Inhibits HAp crystal growth

1.2. Bone Cells

Bone has the capability of repairing itself with a high regenerative capacity due to the presence of four specific types of cells: osteoblasts, osteocytes, osteoclasts and osteogenic (stem) cells (Figure 1.2). Osteogenic cells are undifferentiated cells that are located in the deep layers of periosteum (outer membrane of bone) and bone marrow. They differentiate into osteoblasts during bone remodelling and fracture healing via biochemical signalling. Since the bone has a dense, mineralized structure, oxygen cannot diffuse over long distances, so that high vascularity is required for the growth of healthy bone. If osteogenic cells are surrounded by highly vascularized

environment, like in healthy bone, the cells differentiate into osteoblasts which will develop bone (Hing et al., 2004).

Osteoblasts are fully differentiated, mononuclear cells that are originated from mesenchymal stem cells (MSCs). They are located on the surface of the bone. Osteoblasts have a significant role in extracellular matrix deposition and regulation of its mineralization. Collagen type I, osteonectin, osteopontin, vitronectin, fibronectin alkaline phosphatase and bone sialoproteins are secreted by osteoblasts to produce ECM.

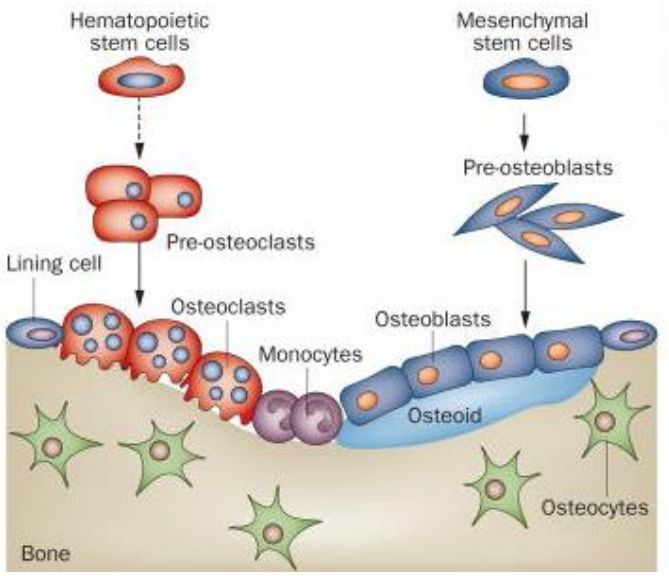

Figure 1.2. Specific cell types of bone.
(Lian et al., 2012).

A proportion of osteoblasts in the bone matrix matures, changes in structure and become osteocyte. Osteocytes are located in lacunae and they have a significant role in the maintenance of mineral concentration of matrix via secretion of enzymes. They can sense the mechanical load via fluid movements through the canaliculi system.

Therefore, they can activate the bone generation or resorption after a mechanical load or tissue damage.

Osteoclasts are multinucleated cells that are differentiated from hematopoietic stem cells (HSCs). They are found at the surface of bone and are responsible for bone resorption, and breakdown. Bone resorption process comprises of dissolving of the mineral phase and digestion of the organic macromolecules by proteases (e.g matrix metalloproteinases) and glycosidases. Bone homeostasis is maintained by the balance between the activities of osteoblasts (bone deposition) and osteoclasts (bone resorption).

1.3. Mechanical Properties of Bone

The unique hierarchical structure of bone, that is composed of collagen and HAp crystals, is responsible for the mechanical properties of it. The HAp crystals provide strength and stiffness to the bone, while collagen fibers give adequate toughness and elasticity. The mechanical properties of the bone are affected by the composition, size and orientation of the mineral crystals, and organization of the collagen fibers. Biomechanical properties of the bone (stiffness, strength, creep and fatigue, elastic modulus) can be measured by many test techniques such as uniaxial compressive or tensile tests, three or four-point bending tests and micro or nanoindentation tests. Age, species, testing conditions (testing dry/wet samples) are factors that affect the mechanical test results. Mechanical properties of the compact and the trabecular bones are different since they have different microstructures and organization (Table 1.2).

Table 1.2. *Mechanical properties of human compact and trabecular bones. (Wang et al., 2016).*

Sample	Porosity	Modulus (GPa)		Strength (MPa)	
Compact Bone	3–5%	Longitudinal	17.9±3.9	Tension	135±15.6
				Compression	205±17.3
		Transverse	10.1±2.4	Tension	53±10.7
				Compression	131±20.7
		Shear	3.3±0.4	Shear	65±4.0
Trabecular Bone	Up to 90%	Vertebra	0.067±0.045		2.4±1.6
		Tibia	0.445±0.257		5.3±2.9
		Femur	0.441±0.271		6.8±4.8

1.4. Bone Repair and Regeneration Mechanism

Bone is a dynamic tissue that is constantly remodelling throughout the life of the person and can repair itself after injury. Bone remodelling relies on the balance between the activities of osteoblasts (bone deposition) and osteoclasts (bone resorption). Every year, about 5% of cortical bone and 20% of trabecular bone are renewed as a result of remodelling (Parra-Torres et al., 2013). The bone healing process after damage involves 4 stages: inflammation, soft callus formation, hard callus formation, and bone remodeling (Figure 1.3). Inflammatory response is required for the bone healing to be initiated. A hematoma occurs immediately after the trauma and platelets, macrophages and other inflammatory cells are accumulated at the site of injury. These cells secrete cytokines and growth factors such as FGF, BMP, and VEGF. Clot is formed and then new capillaries are produced in the clot by endothelial cells. Macrophages and giant cells remove the degenerated cells and other debris. Although the acute inflammatory response reaches the maximum level within the first 24h and continues in the following 7 days, proinflammatory molecules have a significant role in bone regeneration at later stages (Marsell et al., 2011).

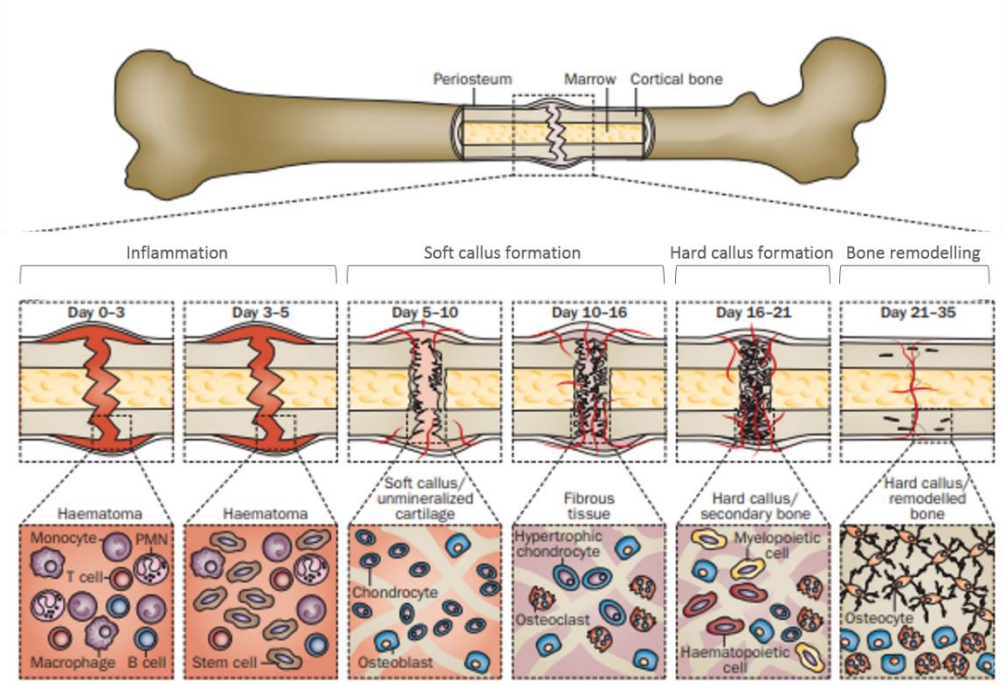

Figure 1.3. Schematic representation of femur fracture healing.
(Adapted from Einhorn et al., 2015).

After the acute inflammatory response, soft callus and hard callus are formed, sequentially. During the soft callus formation, chondrocytes and fibroblasts synthesize cartilaginous matrix as a temporary plug between the bone fragments to provide a semi-rigid support for the fracture. Then, osteoblasts produce the woven mineralized bone matrix in the stable areas of the soft callus and the unstable regions are removed for the formation of the hard callus. Meanwhile, revascularization occurs to provide oxygen for development of osteoblasts from progenitor cells. Soft callus formation occurs between days 5-16. Bone remodelling is the final stage where the hard callus is replaced with new cortical or trabecular bone by the coordinated actions of osteoclasts (resorption) and osteoblasts (new bone formation). Bone healing process continues for months depending on the health conditions of the patient.

1.5. Clinical Needs and Current Treatments in Bone Replacement Therapy

Although bone has a unique self-repairing capacity, this ability is limited to small fractures few millimeters in size. Delayed healing or non-union fractures occurs for the defects above critical size and extensive bone reconstructions are required. Diabetes and genetic factors lead to poor and/or disrupted vascularization and insufficient number of progenitor cell accumulation, and this results in delayed healing or non-union fractures (Ho-Shui-Ling et al., 2018).

1.5.1. Conventional Treatments

Autologous bone grafts are the "gold standard" for the treatment of bone defects due to their osteoconductive and osteoinductive property. Since autografts are obtained from the patient's own body, and they do not induce any immune response. Iliac crest is the most widely used donor tissue site because of the available bone volume and the quality of the bone. However, donor-site morbidity at the harvest site, tissue quantity, and surgery for harvesting tissue that cause pain and expense for patients are the limitations (García-Gareta et al., 2015). Alternatively, allografts (tissue from other humans or typically cadavers) can be used to eliminate the drawbacks of donor site morbidity, pain, cost and the limited quantity that can be harvested. However, risks of infection and immune response are important limitations of allograft use (Turnbull et al., 2018). Besides, the osteoinductive potential of allografts decrease upon the preservation, storage, and sterilization procedures due to the elimination of osteogenic cells and damaged structural integrity of the grafts which leads to reduction in mechanical strength. Consequently, bone graft substitutes are being developed to eliminate all the limitations of autografts and allografts.

1.5.2. Bone Tissue Engineering

The term of tissue engineering (TE) was defined by Langer and Vacanti in 1993 as an interdisciplinary field that combines life sciences and principles of engineering to develop biological substitutes that replace, restore or improve tissue function (Langer and Vacanti, 1993). TE combines cells, scaffolds (cell carriers) and bioactive agents

(e.g. growth factors, drugs) to develop a construct. The first step in TE is the isolation of the cells from the patient and expanding them under *in vitro* conditions. Then, the cells are seeded onto biocompatible and biodegradable scaffolds to meet the structural and mechanical requirements of the defect site. Growth factors might be added to guide the cellular functions such as adhesion, proliferation, differentiation and vascularization (Santos et al., 2010). Tissue engineered constructs are implanted after *in vitro* maturation. Cells produce their own ECM while the scaffold is resorbed and the construct is gradually replaced by the regenerated tissue. Bone tissue engineering is a promising approach for significant clinical challenges such as cranial and maxillofacial defects, bone tumor resections and critical sized bone defects.

1.5.2.1. Cells

Tissue specific cells (e.g., osteoblasts) or stem cells can be used for bone tissue engineered constructs. The possible source of the cells can be autogenic, allogenic or xenogenic. There are important considerations in choosing the cell source. These are ease of harvesting with minimal donor site morbidity, homogeneity of the isolated cells, having sufficient number of cells after expansion, the potential of the differentiation of the cells, and lack of immunogenicity, tumorigenicity and risk of disease transmission (Marolt, 2015; Ercal et al., 2018).

Primary Osteoblasts from the Bone Tissue

Primary osteoblasts isolated from adult bone tissue have been used for bone tissue engineered constructs and clinical studies have been carried out by seeding them onto scaffolds (Springer et al., 2006), hydroxyapatite scaffolds (Mangano et al., 2009), and collagen matrix (Pradel et al., 2006; Pradel et al., 2012). In general, primary osteoblasts obtained from passages 1 and 5 were used in the studies (Tuli et al., 2003).

Mesenchymal Stem Cells

Mesenchymal stem cells (MSCs) are the most commonly used cell source in TE since they have a great potential for differentiation into various types of tissues including

bone, cartilage, muscle and fat (Figure 1.4). MSCs can be isolated from a variety of sources such as bone marrow, adipose tissue, skeletal muscle, synovial membrane and dental tissues.

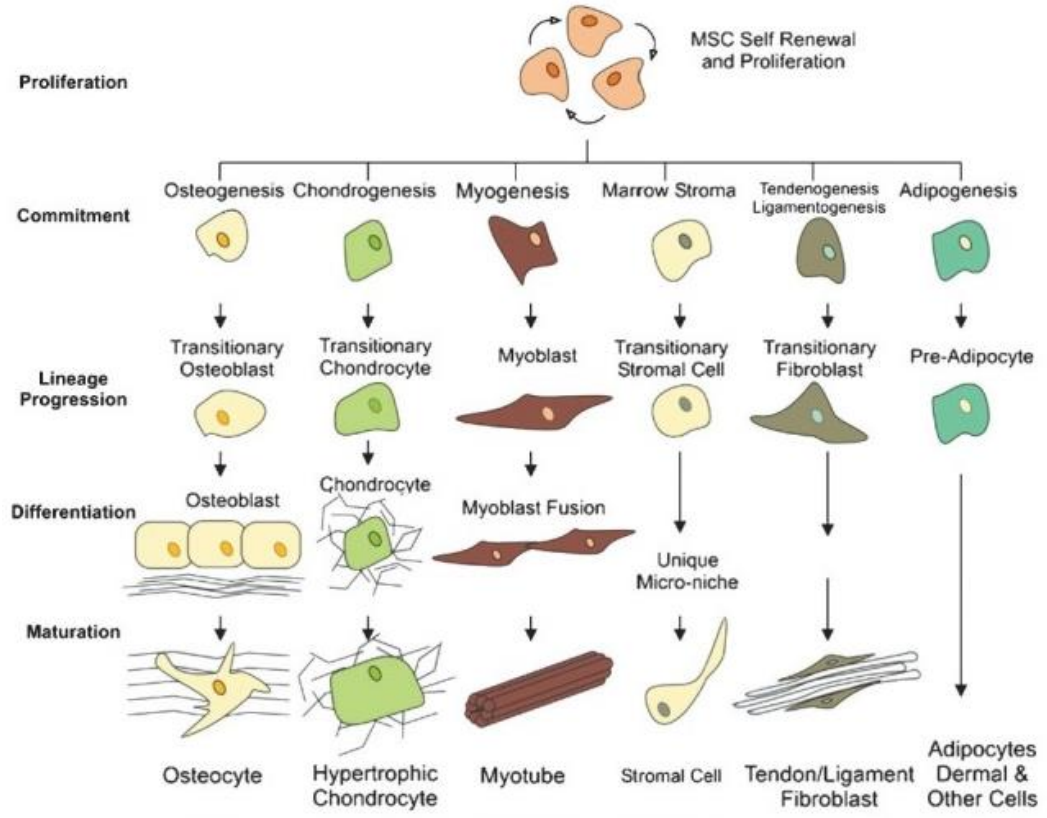

Figure 1.4. Self-renewal, proliferation, and potential lineage specific differentiation pathways of MSCs. (Firth et al., 2012).

Bone marrow derived mesenchymal stem cells (BMSCs) are the most commonly used source for adult MSCs since they are isolated easily and demonstrate regenerative potential with high proliferative capacity. It was shown that BMSCs differentiate into osteoblasts more effectively than adipose derived stem cells (ADSCs) (Han et al., 2014). Clinical trials were performed with BMSCs by seeding them on ceramics (Marcacci et al., 2007), hydroxyapatite scaffolds (Quarto et al., 2001), hydroxyapatite-beta tricalcium phosphate scaffolds (Shayesteh et al., 2008), hydroxyapatite particles

(Meijer et al., 2008), or by local injection after mixing with fibrin (Zhao et al., 2012; Kim et al., 2009; Giannotti et al., 2013). Adipose derived stem cells (ADSCs) have drawn attention for tissue engineering applications since they have multi-lineage differentiation capacity and ease of harvesting from abundant adipose tissue (Ho-Shui-Ling et al., 2018). There are several reports of clinical studies with ADSCs seeded on TE constructs (Lendeckel et al., 2004; Mesimaki et al., 2009 and Sandor et al., 2013).

Dental pulp stem cells (DPSCs) were isolated enzymatically from adult tooth pulp tissue and were found to have similarities with BMSCs (Gronthos et al., 2000). They are harvested easily compared to BMSCs, have very low rates of morbidity and extensive differentiation ability into adipogenic, chondrogenic, and osteogenic lineages. Osteogenic differentiation of DPSCs has been shown *in vitro* with increased expression of bone related markers (Kanafi et al., 2014; Akkouch et al., 2014) and *in vivo* as new bone formation (d'Aquino et al., 2007; Maraldi et al., 2013).

1.5.2.2. Scaffolds

Scaffolds serve as 3D structural templates made of biocompatible and biodegradable materials with mechanical properties similar to the target tissue. Scaffolds are designed as temporary support materials where the cells deposit their ECM and takes the place of the scaffold over time while the scaffold itself is absorbed by the biological system. An ideal scaffold for bone tissue replacement should allow cell adhesion, proliferation, migration and differentiation (Venkatesan et al., 2015) with adequate porosity to allow nutrient transport and oxygen diffusion for the cells (Turnbull et al., 2018). The size and distribution of pores are important features for bone tissue regeneration and should be balanced with the required mechanical properties of the scaffold for the intended clinical application. The ideal pore diameter of the scaffold for bone tissue engineering applications should be similar to that observed in normal bone which is reported to be about 220 μm (Wu et al., 2017). According to the literature, pore sizes should be in the range of 200-900 μm. Smaller

sizes of 200-400 μm (Ji et al., 2018) and 300-500 μm (Nandi et al., 2018) have also been reported for osteogenesis and angiogenesis.

1.5.2.2.1. Materials

The choice scaffold material is very crucial for the performance of the tissue engineered construct which should meet the minimum requirements of the desired tissue. Materials that have been used in bone tissue regeneration include biodegradable polymers, ceramics, metals and related composites. Biodegradable polymers are the preferable ones because of variety, biodegradability and compatibility and they can be of natural or synthetic origin.

Natural polymers have the advantages of being biocompatible, biodegradable and some are highly bioactive which enables cells to attach, integrate and differentiate on the scaffolds. However, they also have some limitations including poor mechanical properties, presence of pathogenic impurities, being immunogenic and batch-to-batch variability (Liu et al., 2004; Ko et al., 2010). Natural polymers that have been used for bone tissue engineering include collagen (Sayin et al., 2017; Baheiraei et al., 2018), fibrin (Heo et al., 2019), gelatin (Celikkin et al., 2019), starch (Mirab et al., 2018), hyaluronic acid (Yuan et al., 2019) and chitosan (Dhivya et al., 2018). Among them, collagen and gelatin have been widely used in TE applications since they contain biological recognition sites including arginine-glycine-aspartic acid (RGD) amino acid sequences, and target sequences for matrix metalloproteinases (MMPs) that allow for ECM remodeling (Posritong et al., 2019). Methacrylated gelatin (GelMA) is a photopolymerizable hydrogel, which is obtained by the modification of the amine containing side groups with methacrylic anhydride, can be crosslinked upon UV exposure. Since the RGD sequences and target sequences for MMP are maintained, biocompatibility and bioactivity of gelatin are not affected after modification with methacrylic anhydride (Sun et al., 2018). GelMA has been widely used in bone tissue engineering (Paul et al., 2016; Thakur et al., 2016; Bymbaa et al., 2017; Wenz et al., 2018; Zheng et al., 2018; Shao et al., 2018).

Synthetic biodegradable polymers are also widely used in bone tissue engineering since they possess numerous advantages such as reproducibility, high mechanical properties, processability. In addition, they are not immunogenic and they can be synthesized with the desired properties. Their main disadvantage is absence of recognition sites, so they are generally used with secondary modification to improve bioactivity (Wang et al., 2016). The most commonly used synthetic polymers are poly(glycolic acid) (PGA), poly(lactic acid) (PLA) and their copolymers poly(lactic acid-co-glycolic acid) (PLGA) (Yang et al., 2018), poly(ε-caprolactone) (PCL) (Malikmammadov et al., 2018; Bruyas et al., 2018; Bao et al., 2019) and poly(propylene fumarate) (PPF) (Olthof et al., 2017; Wu et al., 2018;). PCL is FDA approved material for use in medical devices such as sutures (Monocryl®), drug release systems (Capronor®, SynBiosys®), and nerve guides (Neurolac®). PCL is a semi-crystalline, thermoplastic polymer which has a low glass transition temperature (-60^{o}C), low melting temperature (60^{o}C), and high decomposition temperature (350^{o}C). PCL has been preferred in long term implantable systems, since it maintains its mechanical properties up to 6 months and then degrades gradually in about 2 years (Perez et al., 2018). Poly(propylene fumarate) (PPF) is biodegradable and photocrosslinkable polymer due to unsaturated bonds in its structure. PPF degrades into its original fumaric acid and propylene glycol subunits which are known to be nontoxic and can be metabolized as a constituent of the Krebs cycle (Kasper et al., 2009). Besides, PPF has excellent mechanical properties for load bearing and bone conduction grafts (Yaszemski et al., 1995; Wang et al., 2006).

Calcium phosphate ceramics are widely used in bone tissue engineering, since they have favorable bioactivities such as osteoconductivity and osteoinductivity. These are most frequently utilized ceramics due to their prevalence in the native bone tissue. Hydroxyapatite (HAp) and β-tricalcium phosphate (β-TCP) are the preferable calcium phosphate based bioceramics in biomedical applications (Hasirci V. and Hasirci N., 2018). Chemistry of HAp is similar to the natural apatite in bone with Ca/P ratio of 1.67 which is higher than the other calcium phosphate ceramics. CaP materials enhance osteointegration via forming a bioactive apatite layer on the surface of the

scaffolds which induces the binding of cytokines and adhesive proteins, such as fibronectin, to CaP materials (García-Gareta et al., 2015). Ceramics are highly brittle. *Composite biomaterials* that consist of polymers and ceramics are appropriate combinations which possess bioactivity and mechanical properties suitable for bone tissue engineering applications. Polymer/ceramic based composite scaffolds mimic the native bone which is also a composite material that consists of HAp as the main ceramic component and collagen as the main natural protein based polymer.

1.5.2.2.2. Scaffold Fabrication Techniques

Target application area, the material type and processing conditions are 3 important factors that affect the choice of the scaffold fabrication technique. Some materials (e.g natural polymers) cannot withstand high pressure or heat, while some others (e.g synthetic polymers) can be processed in harsh conditions. There are a large variety of fabrication techniques including solvent casting, particulate leaching, gas foaming, freeze drying, phase separation, electrospinning and 3D printing.

1.5.2.2.2.1 Conventional Techniques for Scaffold Fabrication

1.5.2.2.2.1.2 Solvent Casting/Particulate Leaching

Solvent casting/particulate leaching method is used for fabrication of porous polymeric scaffolds. A polymer solution containing particles (salt or porogen) is poured in a mold and after solidification of the polymer, particulates are removed with a liquid which dissolves the porogen but not the polymer. A polymeric scaffold with a porous network is left behind. However, difficulty in controlling of pore shape and interconnectivity is a drawback of this method. This technique has been used to fabricate PCL (Thadavirul et al., 2014; Intranuovo et al., 2014) and PMMA (Sola et al., 2019) scaffolds for bone tissue engineering.

1.5.2.2.2.1.3 Gas Foaming

In the gas foaming method, gas bubbles are used instead of porogens. Therefore, the use of a solvent is avoided in this method. A porous structure is created upon nucleation of the gas bubbles dispersed in the polymer. Carbon dioxide, which is

formed upon the chemical reaction between an acid and sodium carbonate, is generally used (Hasirci et al., 2016). Although it is difficult to control the pore sizes and interconnectivity, pore sizes of up to 10 cm with porosities of up to 93% can be obtained (Turnbull et al., 2018). Gas foaming has been used to fabricate biphasic calcium phosphate scaffolds (Kim et al., 2012) and calcium phosphate cement with chitosan (Chen et al., 2012).

1.5.2.2.2.1.4 Freeze Drying (Lyophilization)

Freeze drying is a technique in which phase separation occurs between the solvent and the polymer upon freezing of a polymer solution. Solvent is sublimated under low temperature and vacuum conditions. A porous foam or sponge with interconnected porous structure is obtained at the end of the process. Freeze drying is widely used for the fabrication of PLLA/TCP (Xiong et al., 2002), hydroxyapatite (Deville et al., 2006) and collagen-glycosamioglycan (Murphy et al., 2010) scaffolds for bone tissue engineering applications.

1.5.2.2.2.1.5 Electrospinning

Electrospinning is another popular technique used in the fabrication micro and nanofibrous scaffolds. In this method, potential is applied between the metal needle of a syringe (filled with a polymer solution) and a metal collector. A polymer jet is formed due to the voltage created by the electric field, the solvent evaporates and polymer filaments are collected. Applied potential, nozzle diameter, distance between the tip and the collector, and type of the solvent are the main parameters that affect properties of the fibers (Li and Xia, 2004). This technique has been used to produce silk fibroin (Li et al., 2006), hydroxyapatite/chitosan (Zhang et al., 2008), and PLLA/HAp (Prabhakaran et al., 2009) scaffolds.

1.5.2.2.2.2 Additive Manufacturing (AM) Techniques

Production of 3D scaffolds with precisely controlled inner or exterior microarchitectures by using conventional scaffold production techniques is difficult. Additive manufacturing (also known as 3D printing) is used to build complex

structures by layer-by-layer deposition of a material using computer aided design (CAD) data, which improves the precision and repeatability of scaffold production. Additive manufacturing was first used in the early 1980s and by the biomedical researchers in the 1990s to produce custom made prosthesis for patients (Webb, 2000). The production process starts with the imaging of the damaged region with computed tomography (CT) or magnetic resonance imaging (MRI) scans, then raw data of the images are converted into a CAD model and 3D solid structure is generated by using 3D printers (Figure 1.5). Since the technique uses the data obtained from CT or MRI, scaffolds with well determined 3D shape which perfectly fit into an irregular defect site can be produced. Another advantage of the technique is that the complex structures with predefined pore size and geometry can be fabricated (Hasirci et al., 2016). The 3D printing technology can be classified according to the technique used in production such as stereolithography (SLA), selective laser sintering (SLS), inkjet printing (IP), and fused deposition modeling (FDM).

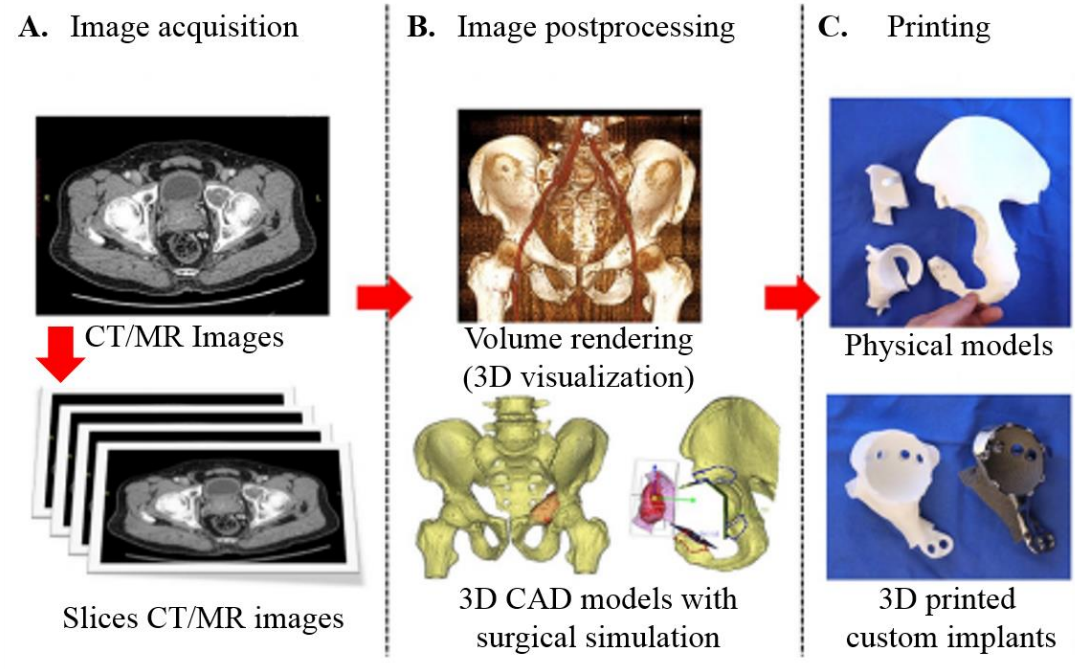

Figure 1.5. Stages of manufacturing patient-specific implants.
A) Image acquisition, B) image processing, and C) 3D printing (Adapted from Wong, 2016).

Stereolithography (SLA)

Stereolithography (SLA) is a liquid-based process that involves polymerization of a photosensitive resin in layer-by-layer fashion upon ultraviolet (UV), infrared (IR) or visible light irradiation (Figure 1.6A). SLA allows fabrication of 3D scaffolds with controlled architecture and micrometer level resolution (e.g traditional SLA: 25 μm and micro SLA: 10 μm in z direction, thickness). However, SLA has important limitations such as extensive postprocessing and washing steps, poor mechanical properties, limited number of biocompatible and biodegradable materials suitable for the technique, and the need to use of UV-based crosslinking (Guvendiren et al., 2016). In the literature, 3D poly(propylene fumarate)/diethyl fumarate (PPF/DEF) (Lan et al., 2009; Lee et al., 2009) and functionalized poly(D,L-lactide)/nanosized hydroxyapatite composite (PDLLA/HAp) (Ronca et al., 2013) scaffolds were fabricated with SLA method.

Selective laser sintering (SLS)

Selective laser sintering (SLS) is based on using a laser beam to sinter a powdered material layer-by-layer (Figure 1.6B). Ceramics, metals and thermoplastic polymer powders are used in SLS to produce 3D structures. In this method, laser binds the beads of the powdered material to each other. 3D PCL/HAp composite scaffolds with mechanical properties similar to trabecular bone were obtained by using SLS (Williams et al., 2005; Xia et al., 2013). However, the process has limitation of providing of printing cells due to elevated temperature.

Inkjet Printing (IP)

Inkjet printing process is based on using thermal or acoustic forces to eject droplets from a nozzle (Figure 1.6C). In thermal inkjet printers, heat is used to generate pressure pulse causing ejection of a droplet of bioink, while other systems use piezoelectric crystals that are mechanically stressed by the application of potential (Turnbull et al., 2016). 3D structures are obtained after cooling, crosslinking or solvent evaporation following the deposition of the material. Cell loaded polymer solutions

can be dispensed with very high accuracy (100 μm) and speed (Sears et al., 2016). However, the process has some limitations such as frequent nozzle clogging, exposing cells thermal and mechanical stress and nonuniform droplet size. It was reported that MSCs loaded PEG-GelMA constructs with satisfactory mechanical properties (Gao et al., 2015), and calcium phosphate and collagen scaffolds were printed successfully by this method for bone tissue engineering (Inzana et al., 2014).

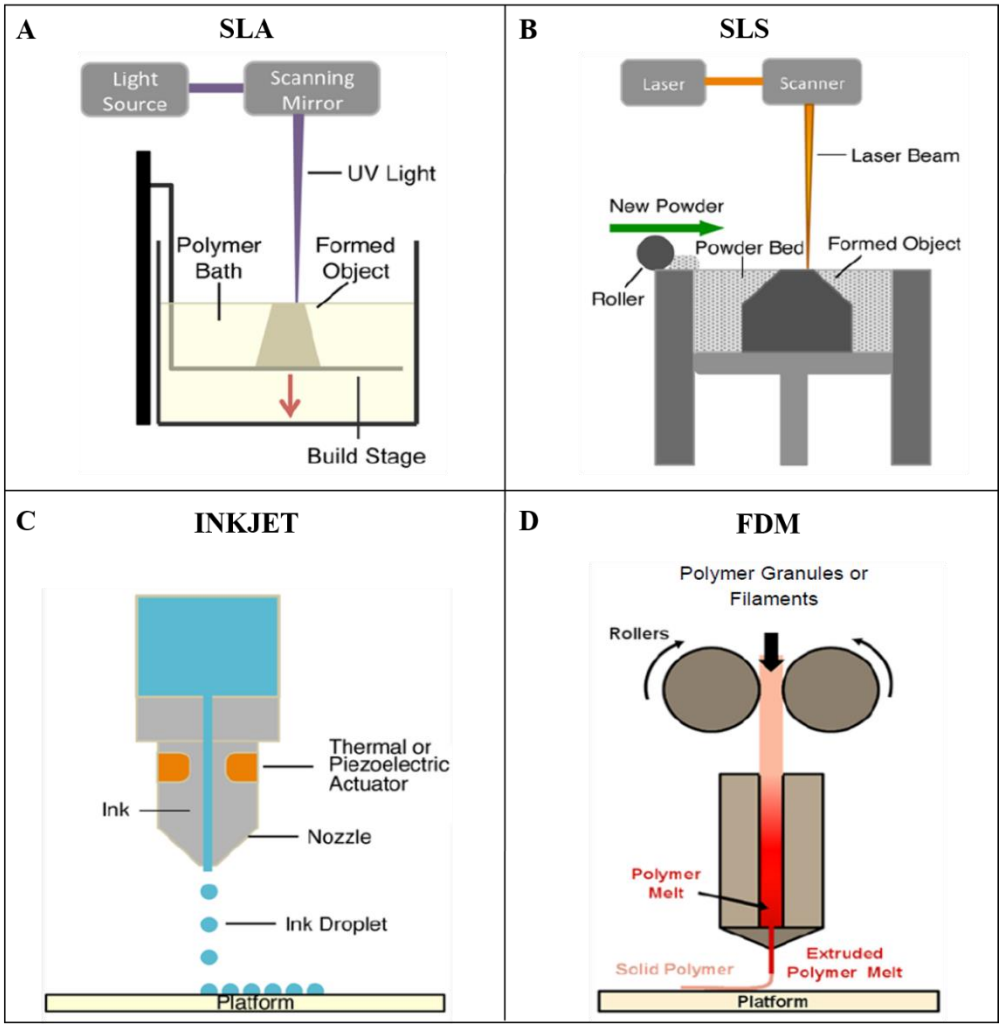

Figure 1.6. Additive manufacturing techniques.
A) Stereolithography, B) Selective laser sintering, C) Inkjet printing, D) Fused deposition modeling (Adapted from Guvendiren et al., 2016).

Fused Deposition Modeling

Fused deposition modeling (FDM) is based on the deposition of molten thermoplastic polymer, through a nozzle (Figure 1.6D). The filaments fuse together and cool after printing and create the construct. FDM is the most commonly preferred 3D printing technique because its simplicity and high mechanical strength of the fabricated materials (Turner et al., 2014). PCL is an ideal thermoplastic polymer to be used for FDM due to its low melting temperature (60^{o}C), biocompatibility and moderate mechanical properties after production (Buyuksungur et al., 2017). Polymethylmethacrylate (PMMA) (Espalin et al., 2010), PLA (Kao et al., 2015), PLGA (Ge et al., 2009) and composites such as polycaprolactone/hydroxyapatite (PCL/HAp) blend (Lee et al. 2014), PCL/PLGA/β-TCP (Shim et al., 2014) have also been processed with this approach.

3D Bioprinting

3D Bioprinting is a promising 3D printing technology by which cells, extracellular matrices and growth factors can be deposited layer-by-layer in user defined patterns to produce highly organized 3D constructs. In contrast to conventional tissue engineering techniques of seeding cells onto the scaffold, 3D bioprinting allows precise 3D placement of cells or biological contents because the cells are entrapped within hydrogels which are 3D printed (Shafiee et al., 2016). Cells are isolated from biopsies or blood samples and expanded through cell culture to maximize the cell density for bioprinting. Following culture, cells are loaded in selected bioinks which is then deposited in a predetermined 3D geometry by using a CAD model. The main technologies used for bioprinting are inkjet, extrusion and laser based printing systems (Figure 1.7).

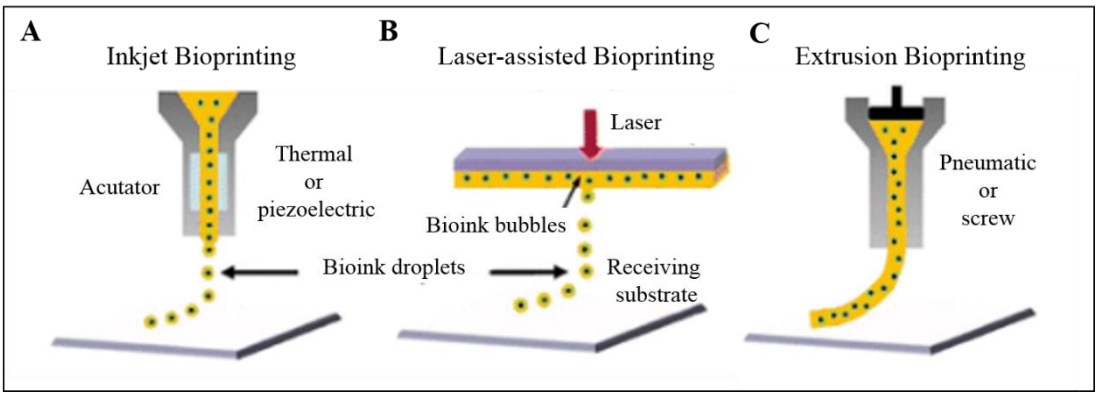

Figure 1.7. 3D Bioprinting methods.
A) Inkjet bioprinting, B) Laser-assisted bioprinting, and C) Extrusion bioprinting.
(Adapted from Tasnim et al., 2018).

Hydrogels are networks of hydrophilic polymers that can absorb and retain large amounts of water (Hasirci et al., 2016). They are highly permeable to oxygen and nutrients which makes them suitable for cell growth. It has been reported that certain hydrogels facilitate cell adhesion, matrix integration, angiogenesis, and osteoconductivity in bone tissue engineering applications (Fellah et al., 2006; Kim et al., 2007; Chimene et al., 2016). Collagen, gelatin, GelMA, alginate, agarose and dual or triple combinations of these hydrogels have been used as composite bioinks in bone tissue engineering (Park et al., 2014; Gao et al., 2015; Campos et al., 2016). Among them, GelMA hydrogel has been preferred since it induces osteogenic differentiation and calcium deposition *in vitro* and enhances endochondral bone formation *in vivo* (Kang et al., 2014; Visser et al., 2015; Celikkin et al., 2018). There are many studies showing the suitability of GelMA hydrogels for 3D bioprinting (Yue et al., 2015; Celikkin et al., 2019).

Hybrid Printing

Although low viscosity hydrogels support cell function and viability, their low mechanical integrity is often unsuitable for bone tissue engineering applications. Therefore, many strategies have been developed by which cell loaded hydrogels are

deposited together with synthetic biodegradable polymers to improve the mechanical strength of the scaffold. According to the study of Kang et al. (2016) a hybrid scaffold containing human amniotic fluid-derived stem cells (hAFSCs) loaded hydrogel consisting of gelatin, fibrinogen, hyaluronic acid and glycerol was printed with PCL and Pluronic F127 hydrogel. Fibrinogen was crosslinked with thrombin, and uncrosslinked materials (gelatin, HA, glycerol and Pluronic F127) in the hydrogel were washed out to create microchannels in the construct. After 24 h of culture high cell viability (91±2%) was observed. Also, osteogenic differentiation of hAFSCs in the printed scaffold was confirmed by Alizarin Red staining of deposited calcium phosphate. Daly et al. (2016) printed BMSCs loaded RGD incorporated alginate bioink with PCL. The compressive modulus of the scaffold was 350-fold increased with the addition of PCL. The construct was printed in the geometry of vertebral body and implanted subcutaneously into the back of nude mice and after 12 weeks of implantation it was observed that the vascularized bone was developed.

1.6. Approach, Aim, and Novelty of The Study

The aim of the current study was to prepare patient specific (pre-determined shape) tissue engineered constructs to be used in the treatment of bone defects. Two different strategies were used in the preparation of 3D constructs. First, cell loaded PCL/GelMA hybrid structures were fabricated. As a second strategy, PCL based composite scaffolds with nanohydroxyapatite (HAp) and poly(propylene fumarate) (PPF) were prepared.

Low cell seeding efficiency and non-uniform cell distribution throughout the scaffold is still a problem in post-fabrication cell seeding as reported in the literature (Martin et al., 2004). Prototyping techniques can be combined with high water content polymers and cell encapsulation strategies in hydrogels to overcome these problems. Printing cell loaded hydrogels together with synthetic biodegradable polymers is the recent approach used to overcome the limitations of low mechanical strength, low cell seeding efficiency and non-homogenous distribution of the cells. In this study, 3D

hybrid structure of PCL and dental pulp stem cells (DPSCs) loaded GelMA were fabricated. PCL fibers and cell loaded GelMA hydrogel were printed side-by-side. PCL had 2 main roles in this study: 1) to enhance the mechanical strength of the cell loaded construct which is suitable for bone tissue, and 2) to protect the cells in the hydrogel from the mechanical loads when implanted in bone. Therefore, the hybrid scaffold possesses high mechanical strength due to PCL presence in each layer. Also, cells were distributed homogeneously throughout the scaffold. This is a novel approach for bioprinting that yields constructs in which the mechanical stiffness is provided by thermoplastic polymers and homogeneous distribution or placement of multiple cell types embedded in hydrogels.

Custom designed 3D PCL scaffolds were produced by FDM printing and then, PCL/HAp and PCL/HAp/PPF composite scaffolds were prepared by sequential surface modification of the PCL to increase the biological functionality of the scaffolds. The main advantage of PPF is to enhance the mechanical strength for use in load bearing applications. Since degradation of PCL scaffolds starts from the surface, PPF coated scaffolds provide extra strength to the reconstructed region during healing. Also, excellent osteoconductivity has been reported when PPF is used with the calcium phosphate particles (Dadsetan et al., 2015). Scaffolds were produced with 2 different architectures achieved by changing the configuration of the deposited fibers: basic (B) and basic shift (BS). Physical and chemical properties of the 3D scaffolds were characterized and bone marrow derived mesenchymal stem cell behavior on the scaffolds was investigated *in vitro* conditions. *In vivo* bone regeneration capability of the PCL/HAp and PCL/HAp/PPF scaffolds was assessed after orthotopic implantation in femoral defects of rabbits.

Although there are many studies in the literature with PCL and PCL/HAp scaffolds to use in bone tissue engineering field, this is the first study in which the PCL/HAp/PPF composite scaffold was prepared and investigated. Surface modification of 3D printed PCL scaffolds increase biological functionality by coating them with nano HAp and HAp/PPF. Besides, HAp nanoparticles can be entrapped in the PPF and the structure

can be stabilized due to post crosslinking feature of the PPF. This study is significant for its potential to fabricate biologically and mechanically functional PCL based tissue engineering constructs, which have the potential to go into clinical trials for the treatment of bone defects.

The content of this theses was previously published by RSC [Buyuksungur, S., Tanir, T. E., Buyuksungur, A., Bektas, E. I., Kose, G. T., Yucel, D., Beyzadeoglu T., Cetinkaya E., Yenigun C., Tönük E., Hasirci, V., and Hasirci, N. (2017). 3D printed poly(ε-caprolactone) scaffolds modified with hydroxyapatite and poly(propylene fumarate) and their effects on the healing of rabbit femur defects. Biomaterials Science, 5(10), 2144-2158)]. The journal stated that there was no need for a permission for the authors to reproduce material contained in the article (https://www.rsc.org/journals-books-databases/journal-authors-reviewers/licences-copyright-permissions/#reuse-permission-requests).

CHAPTER 2

MATERIALS AND METHODS

2.1. Materials

Poly(ε-caprolactone) (PCL) (MW 80,000 g/mol), hydroxyapatite (HAp) nanopowder (<200 nm), Irgacure 2959 (2-(hydroxy)-4'-(2-hydroxyethoxy)-2-methylpropiophenone), fumaric acid, porcine skin gelatin type A (100 bloom), methacrylic anhydride, β-glycerophosphate disodium salt hydrate, dexamethasone, L-ascorbic acid, *pseudomonas* lipase, bovine serum albumin (BSA) were purchased from Sigma-Aldrich (USA). PCL (MW 50,000 g/mol) was obtained from Polysciences (USA). Potassium dihydrogen phosphate dihydrate, dipotassium hydrogen phosphate and sodium chloride were products of Merck (Germany). Trypsin/EDTA, Live-Dead cell viability/cytotoxicity kit, Alexa Fluor™ 488 phalloidin, dimethyl sulfoxide (DMSO) and GeneJET RNA purification kit were obtained from Thermo Fisher Scientific (USA). Fetal bovine serum (FBS) was obtained from Biowest (France). Alizarin Red was obtained from Cyagen (USA). Penicillin/streptomycin (100 U/mL-100 μg/mL) was the product of Fluka (Switzerland). Alamar Blue cell proliferation assay solution was purchased from Invitrogen Inc. (USA). Dulbecco's Modified Eagle Medium (DMEM) High glucose (glucose concentration: 4.5 g/L) and L-glutamine (200 mM in 0.85% NaCl solution) were purchased from Lonza (Switzerland). DMEM:F12 was obtained from BI (USA). NucleoCasette was from ChemoMetec (Denmark). Triton-X 100 was purchased from PanReac Applichem (Germany). Alkaline phosphatase (ALP) kit was from Anaspec (USA). MEM-α (1X)+GlutaMAX™ was purchased from Gibco (USA). Alexa Fluor® 488 anti-human CD31, CD45 and Mouse IgG1κ; and Alexa Fluor® 647 CD90 and CD105 antibodies were purchased from BioLegend (USA).

2.2. Methods

2.2.1. Synthesis and Characterization of Polypropylene fumarate (PPF)

PPF was synthesized by the condensation reaction of fumaric acid and propylene glycol (1.5:1.65 moles) using the method modified from Lee et al. (2007) (Figure 2.1). As a radical inhibitor, 0.1% (w/w) hydroquinone and as a catalyst, 0.4% (w/w) p-toluene sulfonic acid were used where the amounts were based on the total weight of propylene glycol and fumaric acid mixture. Water was produced as a by-product of the reaction.

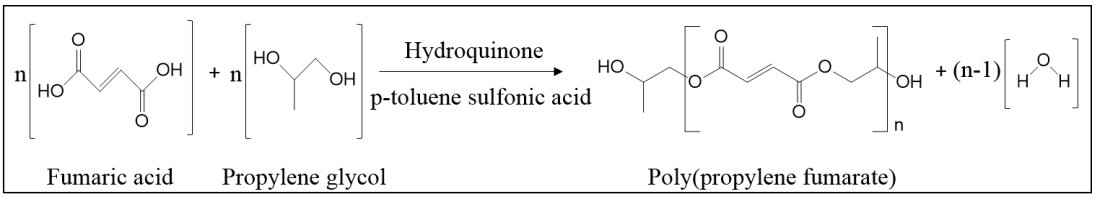

Figure 2.1. The synthesis of polypropylene fumarate.

For the purification process, PPF was dissolved in dichloromethane (DCM) and vacuum filtration was applied to eliminate the unreacted solid fumaric acid. Residual water was eliminated by adding anhydrous calcium chloride and PPF was obtained in liquid form. PPF was dissolved in chloroform (1 %, v/v) and the molecular weight of the PPF was determined by using Gel Permeation Chromatography (GPC) (CTO-10ASVP, Shimadzu, Japan). In order to crosslink, PPF was dissolved in acetone (PPF:Acetone, 50:50, w/w), and Irgacure 2959 (5%, w/w) was added as the photoinitiator. Then PPF was exposed to UV (365 nm, distance 15 cm, 0.120 $J.cm^{-2}$) in a UV crosslinking chamber (BIO-LINK-UV Crosslinker BLX-365, USA) for 30 min to crosslink the PPF. The chemical structures of the uncrosslinked and crosslinked PPF were analyzed with Fourier Transform Infrared Spectroscopy (FTIR) (Frontier, Perkin Elmer, USA).

2.2.2. PCL Scaffold Fabrication by 3D Plotting

3D printed PCL scaffolds were fabricated with Bioscaffolder® (SYS+ENG, Germany). PCL pellets (80,000 g/mol, mp: 60°C, d=1.145 g/mL at 25°C) were placed in the stainless steel syringe and heated to 170°C. When melting was completed, the polymer was extruded through a nozzle with 210 μm (27 gauge) inner diameter. Cylindrical 3D PCL scaffolds (10 mm in diameter and 1.5 mm in height were used in the characterization and *in vitro* studies; 5 mm diameter and 2.5 mm height samples for *in vivo* studies) were plotted by extrusion of the polymer as a fiber, in a layer-by-layer fashion, up to 10 layers. Scaffolds with different architectures were produced by changing the respective position of the deposited fibers. 3D PCL scaffolds were produced in two different architectures, namely: basic (B) and basic shift (BS) structures (Figure 2.2). The B scaffold was produced by the consecutive deposition of two-dimensional (2D) layers which have fibers that are 90° to each other and 1 mm apart. The BS scaffolds were produced similarly, but each 2D layer was deposited with in a shift distance (0.10, 0.15, 0.20, 0.25 and 0.50 mm) relative to the previous layer.

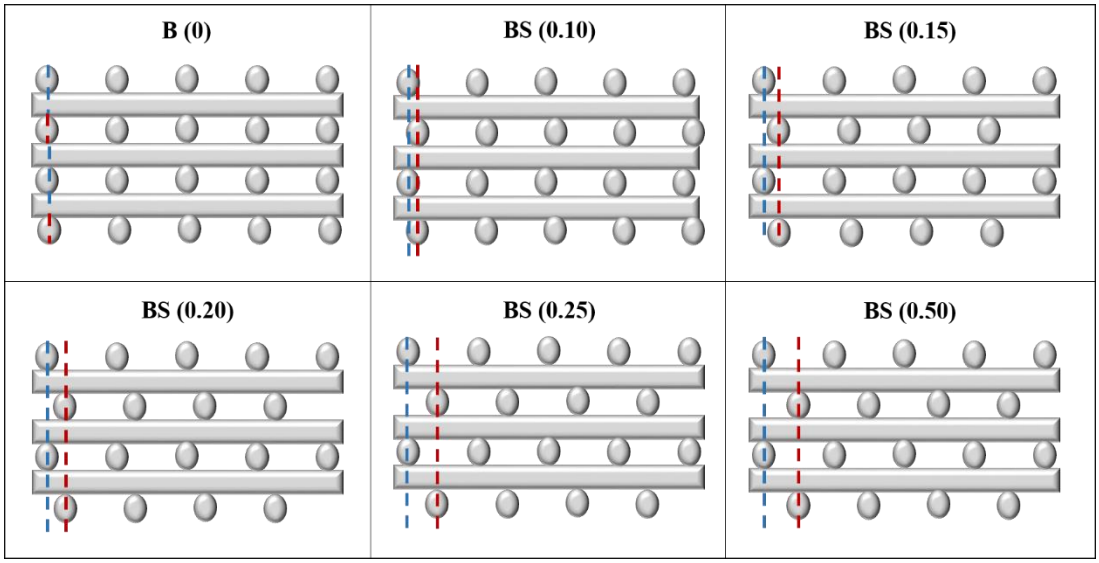

Figure 2.2. Schematic representations of the organization of the B and BS (0.10, 0.15, 0.20, 0.25 and 0.50 mm) PCL scaffolds in cross sectional views.
Blue and red dotted lines are aligned to show the positions of the fibers to compare the shift between subsequent layers.

2.2.3. Preparation of PCL/HAp and PCL/HAp/PPF Composite Scaffolds

In order to prepare PCL/HAp and PCL/HAp/PPF composite scaffolds nanohydroxyapatite (HAp) (5%, w/w) was suspended in the mixture of DCM:Acetone (20:80, v/v) and then the scaffolds were immersed in the suspension (Figure 2.3B). The solvent was allowed to evaporate at room temperature, forming a layer of HAp on the 3D PCL scaffolds.

For the preparation of PCL/HAp/PPF scaffolds, PPF was dissolved in acetone (PPF:Acetone, 50:50, w/w), Irgacure 2959 (5%, w/w) was added as the photoinitiator, and HAp was added to the organic solvent to yield (5%, w/w) solution. The scaffolds were dipcoated (Figure 2.3B) in this suspension and then were exposed to UV (365 nm, distance 15 cm, 0.120 $J.cm^{-2}$) in a UV crosslinker chamber (BIO-LINK-UV Crosslinker BLX-365, USA) for 30 min to crosslink the PPF.

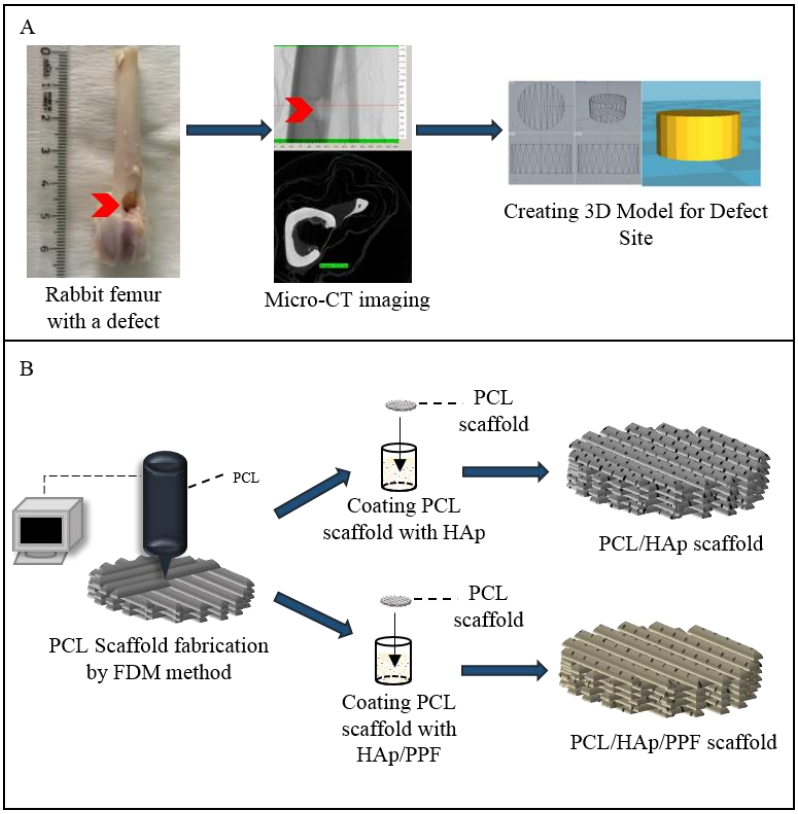

Figure 2.3. Schematic presentation of the PCL based 3D scaffold fabrication process. A) Creating 3D model for defect site of the rabbit femur by using Micro CT. B) Fabrication of PCL/HAp and PCL/HAp/PPF composite. Red arrowhead shows the defect site on the femur.

2.2.4. Synthesis and Characterization of Methacrylated Gelatin (GelMA)

Methacrylated gelatin was synthesized according to the method reported by Lee et al., (2015). The reaction between gelatin and methacrylic anhydride is shown in Figure 2.4. Briefly, porcine skin gelatin type A (20%, w/v) was dissolved in carbonate buffer (0.25 M, pH 9.0) at 50°C. Methacrylic anhydride (2%, v/v) was added into the gelatin solution and stirred for 3 h at 50°C. Then, the reaction was stopped by adjusting the pH to 7.4. Solution was filtered, dialyzed against dH_2O (SnakeSkin, 10K MWCO, ThermoFisher) for 1 day and lyophilized after freezing at -80°C.

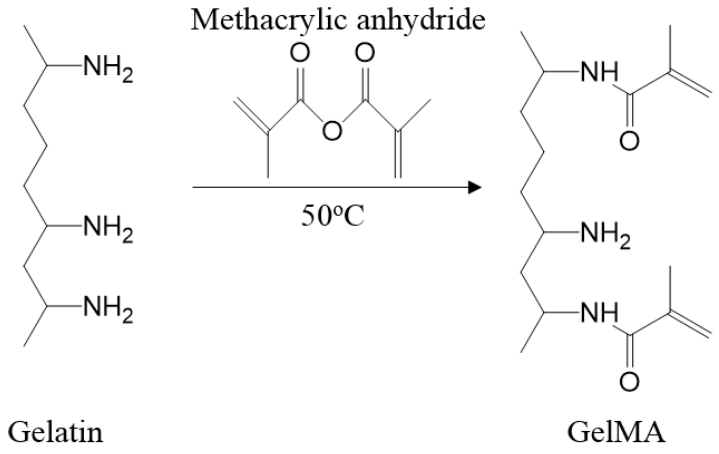

Figure 2.4. The binding of methacrylate groups to the primary NH_2 groups of gelatin.

In the characterization of GelMA, a high resolution proton nuclear magnetic resonance (^{1}H NMR) spectrometer was used at room temperature. Bruker DPX 400 spectrometer operating at ^{1}H resonance frequency of 400 MHz, 16 scans were made. The methacrylated gelatin samples were dissolved in D_2O (30 mg/mL). The degree of methacrylation (DM) was calculated by using MestreNova NMR analysis program (version 6.0.2, Mestrelabs Research, SL, Spain). The degree of methacrylation (DM) of gelatin is defined as follows:

$$\mathrm{DM}(\%) = \left(1 - \frac{\text{Lysine methylene of GelMA}}{\text{Lysine methylene of Gelatin}}\right) \mathrm{X100}$$

2.2.5. GelMA Slab Preparation

GelMA (20%, w/v) solution containing 1% Irgacure 2959 photoinitiator (w/v) was prepared. The GelMA precursor solution was poured into poly(dimethylsiloxane) (PDMS) mold (diameter: 1 cm, height: 1.5 mm) and exposed to UV (365 nm, 15 W/cm^2, 3 cm distance) for 5 s by using OmniCure S2000 UV lamp. GelMA slabs were used as controls in *in situ* degradation and swelling tests.

2.2.6. Hybrid Scaffold Fabrication by 3D Printing

The hybrid structure of PCL and GelMA was printed with EnvisionTec 3D Bioplotter (Germany). The schematic presentation of the scaffold fabrication is presented in Figure 2.5. Square shaped 3D hybrid scaffolds (10x10x1.5 mm^3, 5 layer scaffolds for *in situ* and *in vitro* experiments, and 10x10x3 mm^3, 10 layer scaffolds for the compressive mechanical test) were printed layer-by-layer, through the extrusion of the PCL and GelMA in each layer with different extrusion heads.

PCL powder (50,000 g/mol) was placed in a stainless steel high temperature head and heated to 160^{o}C. The rate of the nozzle movement in the x-y axis was 2 mm/s and the pressure was 7.3 bar for PCL printing. GelMA precursor solution was prepared as mentioned in Section 2.2.5 and placed in a disposable plastic syringe and temperature was set to 22^{o}C. The temperature of the lab was set to 24^{o}C and the printing platform was cooled to 10^{o}C. Both PCL and GelMA were extruded through needles with 400 μm (22 gauge) inner diameter. For GelMA printing, the rate of the syringe movement in the x-y axis was set as 10 mm/s and the pressure was 1.8 bar.

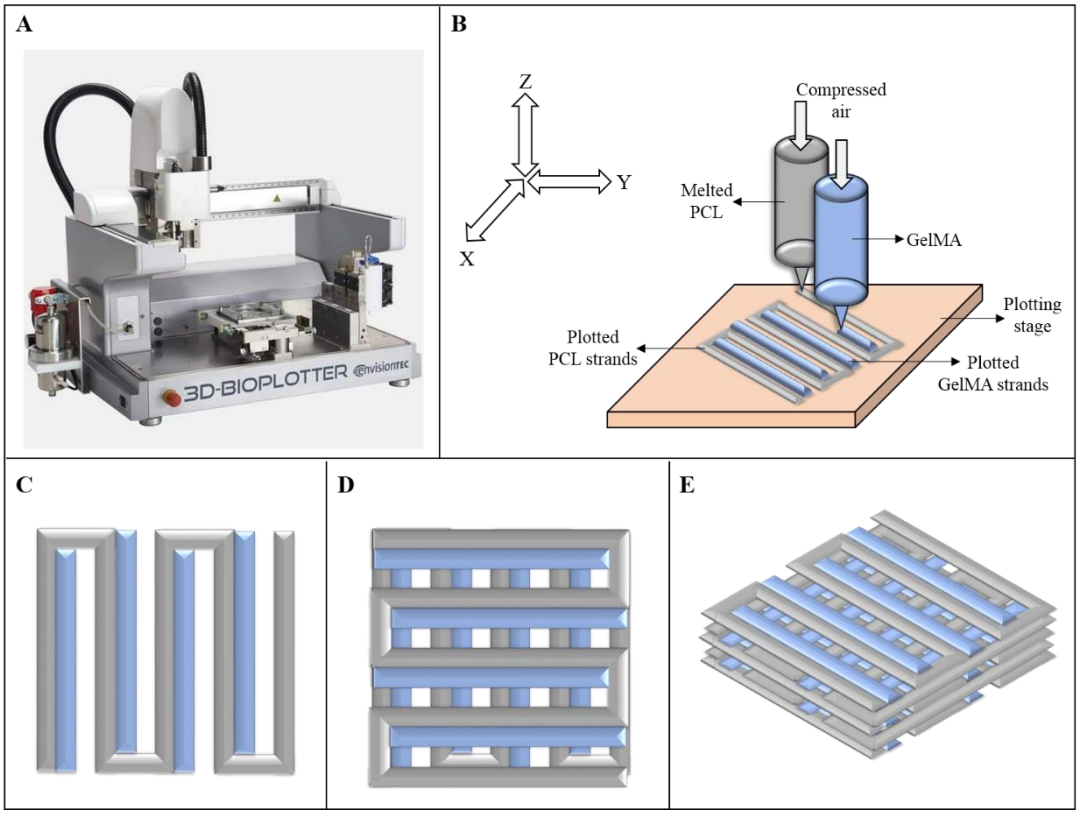

Figure 2.5. Schematic representation of 3D Hybrid scaffold fabrication.
A) EnvisionTec 3D Biplotter, B) Fabrication of PCL/GelMA scaffold, C) Top view of the first layer, D) Top view of the first 2 layers, and E) Side view of the scaffold (5 layers).
Gray fibers: PCL, and blue fibers: GelMA.

After the completion of printing process, the scaffolds were crosslinked under OmniCure S2000 UV lamp (Lumen Dynamics, Canada) (365 nm, 15 W/cm^2, 3 cm distance) for 5 sec. The crosslinking mechanism of GelMA is shown in Figure 2.6.

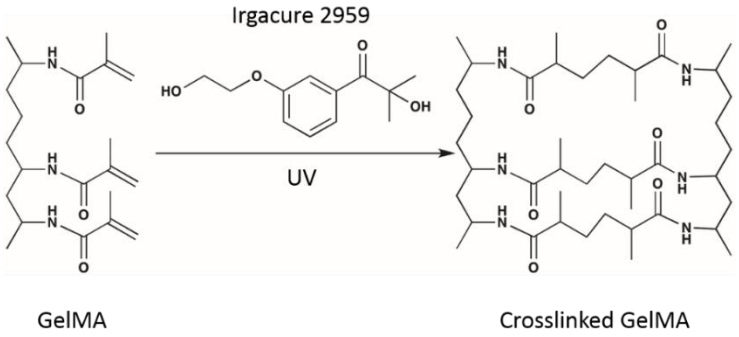

Figure 2.6. Crosslinking mechanism of GelMA by UV radiation in the presence of Irgacure 2959.

2.2.7. Physical and Chemical Characterization of the Scaffolds

2.2.7.1. Scanning Electron Microscopy (SEM) Analysis

Physical and chemical properties of the PCL, PCL/HAp and PCL/HAp/PPF scaffolds were examined with Scanning Electron Microscope (SEM, FEI Quanta 400F, Holland) at the Central Lab of METU. PCL/GelMA hybrid scaffolds were examined with SEM (SEC, NanoEye, South Korea) at BIOMATEN (METU). Chemical structures of PCL, PCL/HAp and PCL/HAp/PPF scaffolds were analyzed with Energy Dispersive X-ray spectroscopy (EDS). In all tests, the samples were mounted on aluminum stubs and sputter coated with gold (Au) under an argon atmosphere before analysis.

2.2.7.2. Micro Computed Tomography (Micro CT) Analysis

Scaffolds were scanned with Micro Computed Tomography (Bruker μ-CT, 1172, Belgium) with the application of 11 μm/pixel size, using aluminum filters. Samples were rotated 0.7^{o} throughout 360^{o}. Porosity and pore size distributions were calculated by using CTAn software (Bruker μ-CT, Belgium). For Micro CT analysis of hybrid scaffolds, PCL/GelMA scaffolds were printed after adding HAp into GelMA in order to make the hydrogel visible during MicroCT analysis.

2.2.7.3. Contact Angle Measurements

Water contact angles (WCA) of the PCL, PCL/HAp and PCL/HAp/PPF scaffolds were measured using a goniometer by the sessile drop method (Attension, Biolin Scientific, Sweden). The measurements were performed with distilled water with a drop volume of 7 μL.

2.2.7.4. Mechanical Analysis

The mechanical properties of the rigid PCL, PCL/HAp and PCL/HAp/PPF scaffolds were studied with Mechanical Tester (Shimadzu AGS-X Universal Test Machine, Japan). The compressive speed was arranged as 1 mm/min. The compressive modulus was calculated from the initial linear elastic region of the stress-strain curve. Scaffolds

were irradiated with a dose of 25 KGy, a ^{60}Co gamma ray, in order to determine the effect of gamma irradiation (which is applied for sterilization) on the mechanical property of the scaffolds. Also, PCL, PCL/HAp and PCL/HAp/PPF scaffolds were compared in order to observe the effect of chemical composition on mechanical properties of the scaffolds.

The compressive mechanical properties of the 3D printed PCL, GelMA and PCL/GelMA scaffolds (10x10x3 mm^3) were studied by using Mechanical Tester (CellScale Univert, Canada). Pure GelMA and hybrid PCL/GelMA scaffolds were kept in PBS (10 mM, pH 7.4) for 24 h to swell before testing. The displacement rate was set as 1 mm/min. The compressive modulus was calculated from the initial linear elastic region of the stress-strain curve.

2.2.7.5. Evaluation of *In situ* Degradation

The stability of the PCL based scaffolds was evaluated by incubating the scaffolds in aqueous media in the presence of *Pseudomonas* lipase enzyme according to ASTM F-1635 standard of USA. Samples were placed into Falcon tubes containing 5 mL of PBS (10 mM, pH 7.4) having 180 U/L lipase, a concentration similar to that in human serum (30-190 U/L) (Martins et al., 2008). Sodium azide (0.2%, v/v) was added to avoid contamination.

The stability of the 3D printed PCL/GelMA (10x10x1.5 mm^3), 3D printed GelMA scaffolds (10x10x1.5 mm^3) and GelMA slabs (diameter: 10 mm, height: 1.5 mm) were evaluated by incubating the scaffolds in PBS (10 mM, pH 7.4) for 21 days. GelMA slabs were prepared as controls.

All samples were kept at 37^{o}C under dynamic conditions in an orbital shaker at 70 rpm (Innova 4000 Incubator Shaker, Germany). Samples were removed periodically, washed with distilled water, freeze dried and weighed to determine the weight loss. The weighed samples were then placed into the degradation medium and incubation was continued. Weight loss was calculated from the following equation:

$$\text{Weight loss } (\%) = \left(\frac{W_0 - W_1}{W_0}\right) X100$$

where W_0 and W_1 are the weights of dry samples before and after degradation, respectively.

2.2.7.6. Equilibrium Water Content (EWC) of GelMA Hydrogels

3D printed PCL/GelMA, 3D printed GelMA and GelMA slabs were incubated in distilled water at 37ºC for 24h in an orbital shaker at 70 rpm (Innova 4000 Incubator Shaker, Germany). The equilibrium water content (EWC) of the GelMA was calculated from the weight difference of the samples in dry and wet states. EWC was calculated according to the equation below:

$$\text{EWC } (\%) = \left(\frac{W_S - W_d}{W_S}\right) X100$$

where Ws: wet sample weight, and Wd: dry sample weight.

2.2.8. *In Vitro* Studies

2.2.8.1. Determination of Cytotoxicity of PCL, PCL/HAp and PCL/HAp/PPF Scaffolds

In vitro cytotoxicity tests of 3D scaffolds were performed according to ISO 10993-5 standard. L929 fibroblasts (passage 5) were seeded in 24 well plate ($3x10^4$ cells/well) and incubated for 24 h before the cytotoxicity test. The tests were performed on extracts of the samples. Extracts of tested scaffolds were obtained by incubating of the scaffolds in complete media (DMEM high glucose medium supplemented with 10% Fetal Bovine Serum (FBS) and 1% penicillin/streptomycin antibiotic) at 37°C for 24 h. After incubation, the culture media were replaced with the extract and incubation continued for another 24 h. The cell cultures treated only with pure media (with no extracts) were used as the control. The number of cells was determined with Alamar Blue cell proliferation assay. The principle of the assay is a color change that can be measured with spectrophotometer as a result of reduction of the oxidized form of

Alamar Blue by mitochondrial enzyme activity which is related to cell number. At each time point, the wells were washed twice with sterile PBS (10 mM, pH 7.4) and incubated for 1 h with Alamar Blue solution (89% DMEM high modified colorless, 10% Alamar Blue and 1% penicillin/streptomycin) in a humidified CO_2 incubator. Then, 200 µL of Alamar Blue solution was transferred into a 96 well plate, and the absorbances of all solutions were recorded at 570 nm (λ_1) and 595 nm (λ_2) with an Elisa plate reader (Molecular Devices, USA). The percent reduction of the dye was calculated using the following equation:

$$\text{Reduction (\%)} = \frac{\left[(\varepsilon_{ox})_{\lambda 2} \text{ x } A_{\lambda 1}\right] - \left[(\varepsilon_{ox})_{\lambda 1} \text{ x } A_{\lambda 2}\right]}{\left[(\varepsilon_{red})_{\lambda 1} \text{ x } A'_{\lambda 2}\right] - \left[(\varepsilon_{red})_{\lambda 2} \text{ x } A'_{\lambda 1}\right]} x100$$

where,

$A_{\lambda 1}$= Absorbance of test well at λ_1= 570 nm

$A_{\lambda 2}$= Absorbance of test well at λ_2 = 595 nm

$A'_{\lambda 1}$= Observed absorbance of negative control well (blank) at λ_1= 570 nm

$A'_{\lambda 2}$= Observed absorbance of negative control well (blank) at λ_2 = 595 nm

$(\varepsilon_{ox})_{\lambda 2}$ = 117.216

$(\varepsilon_{red})_{\lambda 1}$ = 155.677

$(\varepsilon_{ox})_{\lambda 1}$ = 80.586

$(\varepsilon_{red})_{\lambda 2}$ = 14.652

Cell numbers were determined from a calibration curve constructed using the same procedure with known number of cells (Appendix A).

2.2.8.2. Isolation of Bone Marrow Mesenchymal Stem Cells (BMSCs) and Dental Pulp Stem Cells (DPSCs)

Bone marrow mesenchymal stem cells (BMSCs), was isolated by Ezgi İrem Bektaş under the supervision of Prof. Gamze Torun Köse at Yeditepe University. Cells were isolated from New Zealand white rabbits (6 months old, male), were used for the *in vitro* and *in vivo* experiments of the PCL, PCL/HAp and PCL/HAp/PPF scaffolds. Femurs and tibias were aseptically excised and transferred into penicillin and streptomycin containing MEM-α (1X)+GlutaMAX™ media. Metaphysial regions of bones were cut and the marrow in the midshaft was collected in a 50 mL sterile centrifuge tube. Cells were centrifuged at 1700 rpm for 5 min to eliminate fat cells. The resulting cell pellet was resuspended in the primary medium and plated in T-175 flasks. After incubation for 1 week, BMSCs were detached from the plate, frozen in FBS containing DMSO and stored in liquid nitrogen until use.

Dental pulp stem cells were loaded in GelMA and printed with PCL to obtain cell loaded PCL/GelMA hybrid scaffolds. Human DPSCs were isolated from human third molars by Onur Hastürk during his MSc thesis with the approval of the Human Subjects Ethics Committee of Middle East Technical University, Ankara, Turkey (28620816/505-69). Isolated DPSCs were used in this study with the approval of the Human Subjects Ethics Committee of Middle East Technical University, Ankara, Turkey (2017-FEN-053) (Appendix D).

DPSCs were cultured in DMEM:F12 (1:1) medium supplemented with 5 mM L-glutamine, 10% FBS and 1% penicillin/streptomycin. For osteogenic differentiation, DPSCs were cultured in DMEM:F12 (1:1) medium supplemented with 100 nM dexamethasone, 10 mM β-glycerophosphate and 50 μM L-ascorbic acid.

2.2.8.3. Characterization of Dental Pulp Stem Cells (DPSCs) with Flow Cytometry

DPSCs of passage 2-5 were analyzed for cell surface antigens of mesenchymal stem cells by flow cytometry (BD Accuri C6, USA). Cells were detached from the flask

with trypsin and centrifuged at 3,000 rpm for 5 min. The pellet was washed with FACS buffer (1:1000 sodium azide and 1:100 BSA in PBS) and fixed in 4% paraformaldehyde solution for 15 min. Fixed cells were stained with mouse IgG1 anti-human monoclonal antibodies (Biolegend, USA) against CD31, CD45, CD90 and CD105 surface markers. Endothelial CD31 (PECAM) and hematopoietic CD45 (Leukocyte common antigen) are the negative markers since they are absent in MSCs. CD90 (Thy-1) and CD 105 (SH2, endoglin) are positive markers for MSCs. CD 90 is a surface protein and is responsible for cell-cell and cell-ECM interactions. CD105 is a mesenchymal adhesion molecule. Mouse IgG1κ monoclonal antibody was used as the negative control for the detection of nonspecific binding. The cell population was gated on the forward and side scatter chart, and flow cytometry was performed on 10^5 cells per sample. Positive expression was defined as the level of fluorescence greater than 50% of the corresponding unstained cell sample.

2.2.8.4. BMSC Seeding on PCL, PCL/HAp and PCL/HAp/PPF Scaffolds

Each surface of PCL, PCL/HAp and PCL/HAp/PPF scaffolds were sterilized under UV for 30 min. During cell seeding, the scaffolds were placed on sterile teflon disks in order to prevent cell attachment onto the well (TCPS) surface. $1x10^5$ cells were seeded onto scaffolds and 4 h incubation in humidified CO_2 incubator was carried out prior to medium addition (1 mL/well) to ensure cell attachment onto the scaffolds. At the end of the 4 h incubation period, the volume of the medium in the wells was completed to 1 mL. Incubation was performed at 37^{o}C and 5% CO_2 in complete media. Cells were incubated on the scaffolds during 21 days to study cell proliferation and osteogenic differentiation.

2.2.8.5. Preparation of L929 Loaded 3D Bioprinted GelMA Hydrogels

L929 fibroblasts loaded, 3D bioprinted GelMA hydrogels were fabricated for the preliminary studies to determine the effect of printing parameters on cell viability. GelMA precursor (20%, w/v) solution was prepared in DMEM High Glucose medium and 1% (w/v) Irgacure 2959 was added as photoinitiator. Then, the solution was mixed

with L929 fibroblasts to obtain a cell density of $1x10^6$ cells/mL. Square scaffolds (10x10x1.5 mm^3, 5 layer) were printed layer-by-layer. L929 loaded GelMA scaffolds were printed as mentioned in Section 2.2.6. After printing, the scaffolds were crosslinked under OmniCure S2000 UV lamp (365 nm, 15 W/cm^2, 3 cm distance) for 5 s. These cell loaded scaffolds were washed with cell culture medium twice to remove the excess photoinitiator.

2.2.8.6. Preparation of DPSC Loaded, 3D Bioprinted PCL/GelMA Hybrid Scaffolds

GelMA hydrogel precursor solutions were prepared with cell culture medium (DMEM:F12 (1:1)). Irgacure 2959 added to the solution (1%, w/v) as a photoinitiator. Then, solutions were mixed with DPSCs to obtain a cell density of $1x10^6$ cells/mL. Square 3D hybrid scaffolds (10x10x1.5 mm^3, 5 layer) were printed layer-by-layer, through the extrusion of the PCL and GelMA in each layer as mentioned in Section 2.2.6. After printing, the scaffolds were crosslinked under OmniCure S2000 UV lamp (365 nm, 15 W/cm^2, 3 cm distance) for 5 s. Cell laden scaffolds were washed with cell culture medium twice to remove the excess photoinitiator.

2.2.8.7. Determination of BMSC Proliferation on PCL, PCL/HAp and PCL/HAp/PPF Scaffolds

The number of viable cells on the samples was assessed with Alamar Blue cell proliferation assay at predetermined time points (days 7, 14 and 21) as mentioned in Section 2.2.8.1. Cell numbers were determined from a calibration curve constructed using the same procedure with the known number of cells (Appendix B).

2.2.8.8. Determination of Osteoblastic Differentiation

Osteogenic medium (50 μg/mL L-ascorbic acid, 10 nM dexamethasone and 10 mM β-glycerophosphate) was used to promote osteoblastic differentiation (phenotype expression) of the BMSCs and DPSCs. Dexamethasone accelerates upregulation of post-proliferative osteoblast genes resulting in the induction of ALP activity and an

increase in the number of bone nodules (Coelho et al., 2000). L-ascorbic acid influences the differentiation of the preosteoblasts and plays an important role in the production of the collagenous bone ECM by increasing the expression of collagen in a dose dependent manner (Stein and Lian, 1993). β-Glycerophosphate serves as a source of phosphate ions and is strictly required for the formation of a mineralized ECM by the osteoblasts. Alkaline phosphatase (ALP) assay, Alizarin Red staining and quantitative real time polymerase chain reaction (qRT-PCR) analyses were conducted to assess the differentiation of the BMSCs on the scaffolds.

2.2.8.8.1. ALP Assay

Alkaline phosphatase (ALP) concentration secreted from BMSCs on the PCL, PCL/HAp and PCL/HAp/PPF scaffolds was determined using an ALP kit which is based on the conversion of p-nitrophenyl phosphate to p-nitrophenol. Briefly, BMSC seeded scaffolds were washed with PBS and transferred into lysis buffer. Then, the samples were lyophilized, sonicated (30 s, 25 W) on ice and centrifuged (2000 rpm, 10 min). 50 µL of p-nitrophenyl phosphate solution was added to 50 µL of supernatant and incubated (37^{o}C, 1 h). The absorbance was measured with UV-Vis spectrophotometry at 405 nm (Molecular Devices, USA). The concentration of enzyme was calculated from a calibration curve prepared with known concentrations of p-nitrophenol (Appendix C).

2.2.8.8.2. Alizarin Red Staining

Calcium deposition of BMSCs on PCL, PCL/HAp and PCL/HAp/PPF scaffolds and DPSCs in PCL/GelMA hybrid scaffolds was determined by Alizarin Red staining. Scaffolds were washed twice with PBS (10 mM, pH 7.4) and fixed in 4% paraformaldehyde (PFA). Then, the samples were treated with Alizarin Red solution for 15 min to stain them at room temperature and washed three times with dH_2O to remove excess dye. The scaffolds without cells were used as controls. Samples were examined under a stereomicroscope (Stemi 2000 C, Zeiss, Germany). Calcium and

phosphate deposition by DPSCs in PCL/GelMA hybrid scaffolds were quantified with Energy dispersive X-ray spectroscopy at the METU Central Lab.

2.2.8.8.3. Quantitative Real-Time Polymerase Chain Reaction (qRT-PCR) Analysis

Quantitative Real Time Polymerase Chain Reaction (qRT-PCR) analysis was performed by Ezgi İrem Bektaş under the supervision of Prof. Gamze Torun Köse at Yeditepe University. The osteogenic differentiation of BMSCs seeded on PCL, PCL/HAp and PCL/HAp/PPF scaffolds was evaluated. Primers were designed for runt-related transcription factor 2 (RUNX2), collagen type 1 (COL1A1), osteopontin (SPP1) and glyceraldehyde-3-phosphate dehydrogenase (GAPDH) genes (Table 2.1). RUNX2 is a transcriptional factor which plays a role in controlling skeletal development. RUNX2 regulates the differentiation of osteoblasts and the expression of many extracellular matrix protein genes including COL1A1, SPP1 during osteoblast differentiation (Komori, 2010). The PCR reaction conditions were as follows: initial denaturation at 95°C for 10 min, followed by 45 cycles of 95°C for 10 s, 58°C for 30 s and 72°C for 30 s. A cycle threshold (Ct) value was obtained for each sample and averages of duplicate sample values were obtained. Fold changes of each target gene were calculated with the $2^{-\Delta Ct}$ relative quantification method. Mean Ct value of each target gene was normalized to the averaged Ct value of housekeeping gene (GAPDH) which gives the ΔCt value. Finally, fold changes were calculated with the $2^{-\Delta Ct}$ equation.

Table 2.1. *Real-time PCR primer details.*

Gene	Primer nucleotide sequence	Product size (bp)	Genbank accession number
RUNX2	F:GCCACCACCCACTACCATAC R:GCTTCCATCAGCGTCAACAC	258	XM_008262992
COL1A1	F:AGAAATCCGCTGGAGTCTCG R:TCCGTTTTCACCAGGGCTAC	300	XM_008271783
SPP	F:CGTGGTGACAGTGTGGCTTA R:GTGACTTTGGGTTTCCACGC	249	NM_001082194
GAPDH	F:GAAGGTCGGAGTGAACGGAT R:TCTCGCTCCTGGAAGATGGT	231	NM_001082253

2.2.8.9. Microscopical Studies

2.2.8.9.1. Scanning Electron Microscopy (SEM) Analysis

BMSCs on the scaffolds were examined under SEM (FEI Quanta 400F, Holland) at METU Central Lab at the end of 21 days of incubation. The cell seeded scaffolds were washed with PBS (10 mM, pH 7.4) twice, fixed with 4% PFA for 30 min at RT, and freeze dried. The samples were mounted on aluminum stubs and sputter coated with gold (Au) under an argon atmosphere before SEM analysis.

2.2.8.9.2. Live-Dead Cell Viability Assay

3D printed GelMA scaffolds loaded with L929 fibroblasts were cultured for 8 days and PCL/GelMA hybrid scaffolds loaded with DPSCs were cultured for 3 weeks and viability of the cells in the constructs were assessed with the Live-Dead cell viability assay. Samples were washed with PBS, stained with Calcein-AM (2 μM in PBS) and ethidium homodimer-1 (4 μM in PBS) for 20 min. Then, the samples were washed with PBS to remove excess stain and examined with a confocal laser scanning microscope (CLSM) (Zeiss LSM 800, Germany). The micrographs (n=3) were analyzed using ImageJ software (National Institutes of Health, USA) to calculate cell viability according to the equation below:

$$\text{Cell viability (\%)} = \left(\frac{\text{Number of live cells (green)}}{\text{Number of total cells (green and red)}}\right) \text{X100}$$

2.2.8.9.3. Phalloidin Staining

PCL/GelMA hybrid scaffolds loaded DPSCs were removed from TCPS at predetermined time points (days 7, 14 and 21), washed with PBS (10 mM, pH 7.4) and fixed with 4% PFA for 15 min at room temperature. Samples were incubated in Triton X-100 (0.1%, v/v in 10 mM Tris-HCl buffer) for 5 min at room temperature, and then in BSA (1%, w/v in PBS) at 37^{o}C for 30 min to block nonspecific binding. Later, the samples were incubated in Alexafluor 488-Phalloidin at 37^{o}C for 1 h to stain actin. Excess dye was removed by washing with PBS (10 mM, pH 7.4). Distribution of the cells in the gel matrix was examined with CLSM (Zeiss LSM 800, Germany).

2.2.9. *In vivo* Studies

2.2.9.1. *In vivo* Biocompatibility Tests

Biocompatibility tests (Intracutaneous irritation and subcutaneous implantation) of PCL, PCL/HAp and PCL/HAp/PPF scaffolds were performed by 'the Genetic Engineering and Biotechnology Institute' of TUBITAK (The Scientific and Technological Research Council of Turkey) at Marmara Research Center (MAM) which is an organization certified by the 'Ministry of Forestry and Urbanization of Turkey' to perform analyses according to Animal Experiments Ethical Committee Working Principles and Regulations (19.02.2013-313). Below these tests are explained.

2.2.9.1.1. Intracutaneous Irritation Test

Intracutaneous irritation tests were performed according to ISO 10993-10: 2010 and ISO-10993-12: 2012 standards. New Zealand albino rabbits (8-12 weeks old) were used in this test. PBS (polar solvent) and corn oil (non-polar solvent) extracts of the PCL, PCL/HAp and PCL/HAp/PPF scaffolds were applied to the rabbits by

intradermal injection (Figure 2.7). Same solvents were used as controls. Injection sites were examined and scored at 24, 48 and 72 h.

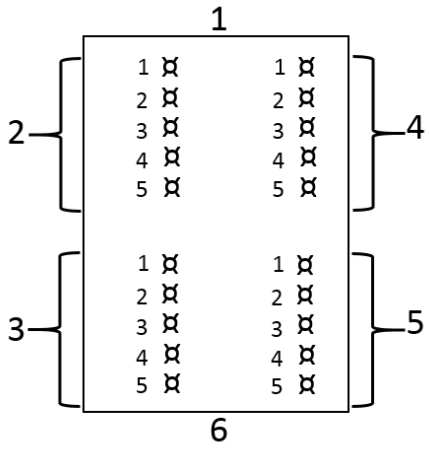

Figure 2.7. Subcutaneous injection regions in the dorsal area of the rabbits.
1; head side of rabbits, 2; test region, 3; negative control region, 4; test region, 5; positive control region, 6; tail side of rabbits.

2.2.9.1.1. Implantation Test

Implantation tests were carried out according to ISO 10993-6: 2007 and ISO 10993-12: 2012 standards. Implantation tests determine the local effects of biomaterials during implantation and involve macroscopic and microscopic histological examinations. Solid silicone was used as negative control. PCL, PCL/HAp and PCL/HAp/PPF scaffolds and negative controls were implanted in the lumbodorsal sites of Sprague Dawley rats (3-4 months old, n=3). Local effects were examined at the end of 28 days of implantation by dissecting the implantation and control regions. These regions were fixed with 4% PFA and then dehydrated with increasing concentrations series of alcohol. Dehydrated tissues were embedded in paraffin blocks and sections were obtained (5 μm in thickness). These sections were stained with hematoxylin-eosin (H&E) for the histological examination.

2.2.9.2. Orthotopic Implantation of PCL, PCL/HAp and PCL/HAp/PPF scaffolds

Orthotopic implantation tests were carried out according to the Animal Experiments Ethical Committee Report by Yeditepe University in agreement with Ministry of Forestry and Urbanization of Turkey Animal Experiments Ethical Committee Working Principles and Regulations (19.02.2013-313) (Appendix E). Implantations were performed by Dr. Tahsin Beyzadeoğlu under the supervision of Prof. Gamze Torun Köse at Yeditepe University. BMSC seeded and cell-free PCL/HAp and PCL/HAp/PPF scaffolds were implanted in the femurs of New Zealand white rabbits (male, 6-8 months old, n=42) (Figure 2.8).

Figure 2.8. Implantation of scaffold into the femur of a New Zealand rabbit.

BMSC seeded PCL/HAp and PCL/HAp/PPF scaffolds ($1x10^6$ cells/scaffold) were incubated for 10 days in osteogenic medium before the implantation. Surgeries were performed under anesthesia with ketamine (35 mg/kg) and xylazine (5 mg/kg). Defects (diameter 5 mm, depth 2.5 mm) were created with a punch on the right femurs of the rabbits, and the samples were introduced to these defects. Antibiotic (Novosef

IM Flakon; 100 mg/kg, Zentiva-Sanofi, France) was applied intramuscularly twice a day for 3 days post-operation. Animals were sacrificed at the end of 4 and 8 weeks by inhalation of CO_2. The femurs of right (implanted) and left (healthy, untreated intact control) legs were removed and kept in PBS (10 mM, pH 7.4) at +4^oC until further examination.

2.2.9.2.1. Micro CT Analysis

Computed microtomographic assessment was performed to investigate the extent of bone regeneration and healing in terms of regenerated bone volume and bone mineral density (BMD). Hydroxyapatite calibration phantoms with densities of 0.25 and 0.75 g/cm^3 were scanned under the same conditions with the rabbit bones for the calibration of BMD. Scans were performed in the wet conditions of the bone. The samples were scanned using 100 kV and 100 μA power and with 12 μm/pixel. Al/Cu filter was used to reduce the beam hardening, 3 frame average was used to reduce the noise, and each frame was obtained in 1710 ms. Samples were rotated 0.4^o throughout 360^o. NRecon was used to reconstruct the sliced images. CTAn was used for the analysis of the images. CTVox and CTVol softwares were used for the visualization of 3D rendered projections and 3D models, respectively.

2.2.9.2.2. Biomechanical Analysis

Biomechanical analysis was performed by Çağrı Yenigün under the supervision of Prof. Ergin Tönük at METU. Four point bending tests were performed to study the mechanical properties and the structural integrity of the new bone bridging into the femur defects. The test was performed by using Mechanical Tester (Shimadzu AGS-X Universal Test Machine, Japan), controlled by a computer program, Trapezium-X. Scaffold implanted femurs (right femur) were compared with the healthy (untreated intact control) counterparts (left femur). Rabbit femurs were placed on the same horizontal plane, where the two lower stabilizing points were 45 mm apart and the two upper loading points were 17 mm apart from each other (Figure 2.9). The test was performed at 5 mm.s^{-1} and a maximum load of 200 N was applied. Stiffnesses of the

scaffold implanted femurs and the controls were calculated by normalizing them with the stiffness values of empty defects.

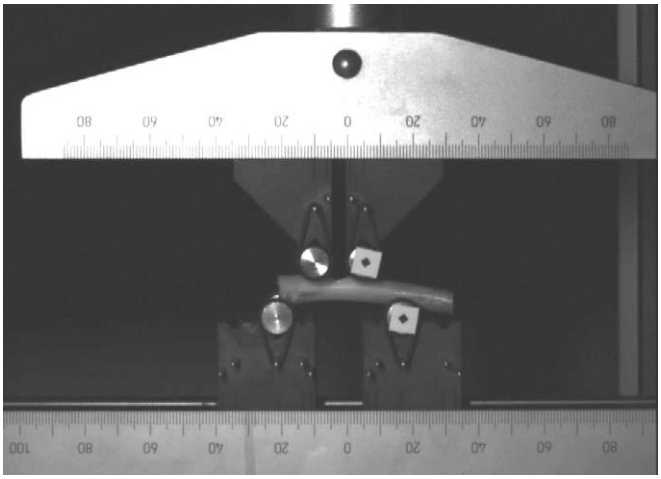

Figure 2.9. Four point bending test of rabbit femurs.

2.2.9.2.1. Histological Analysis

Following the dissection of the bone, samples were fixed with formalin (10%, v/v, pH 7.0) and then decalcified with Shandon TBD-2 Decalcifier for 14 days prior to sectioning for histological analysis to study the integration of the bone and the scaffold, tissue response and the bone formation within the defect. Histological analyses were carried out by Assist. Prof. Deniz Yücel, Acıbadem University, Department of Histology and Embryology. Samples were dehydrated with increasing concentration of alcohol series and embedded into paraffin. Sections with 5 μm in thickness were obtained and these sections were deparafinnized before staining. Hematoxylin-Eosin (H&E) and Masson's Trichrome were used for staining of sections. For H&E staining, samples were incubated in hematoxylin solution for 8 min and in eosin solution for 2 min. For Masson's Trichrome staining, samples were incubated in Weigert iron hematoxylin for 10 min to stain the nuclei of the cells. Then, the samples were kept in Biebrich Scarlet-Acid Fuchsin solution for 5 min. Finally, after washing with distilled water, samples were incubated in aniline blue for 5 min.

2.2.10. Statistical Analysis

All experiments were carried out in triplicates. Statistical analyses were performed using GraphPad Prism version 6.0 (GraphPad, San Diego, CA, USA). P-values ≤ 0.05 were considered significant.

CHAPTER 3

RESULTS AND DISCUSSION

3.1. 3D Printed PCL, PCL/HAp, and PCL/HAp/PPF Scaffolds

3.1.1. Poly(propylene) fumarate (PPF) Characterization

PPF was synthesized by the condensation reaction of propylene glycol and fumaric acid. The number average molecular weight (Mn), weight average molecular weight (Mw) and polydispersity index (PDI) values of PPF were determined with gel permeation chromatography (GPC) (CTO-10ASVP, Shimadzu, Japan) and found as Mn: 1816 g/mol, Mw: 2704 g/mol and PDI: 1.48. The chemical structure of the uncrosslinked and crosslinked PPF was analyzed with Fourier Transform Infrared Spectroscopy (FTIR) (Frontier, Perkin Elmer, USA). The IR spectra (Figure 3.1) showed the characteristic peaks for PPF: ester carbonyl group at 1730 cm^{-1} and unsaturated double bonds in fumarate unit at 1646 cm^{-1}. PPF is crosslinked due to the opening of the unsaturated carbon-carbon double (C=C) bonds in its structure and in the presence of a photoinitiator (Irgacure 2959), it is possible to crosslink the fumarate groups using a UV light. The transmission peak of carbon-carbon double bond (1646 cm^{-1}) decreased, but it can be still observed. This proves that there were still unsaturated double bonds in the polymer structure after the crosslinking reaction.

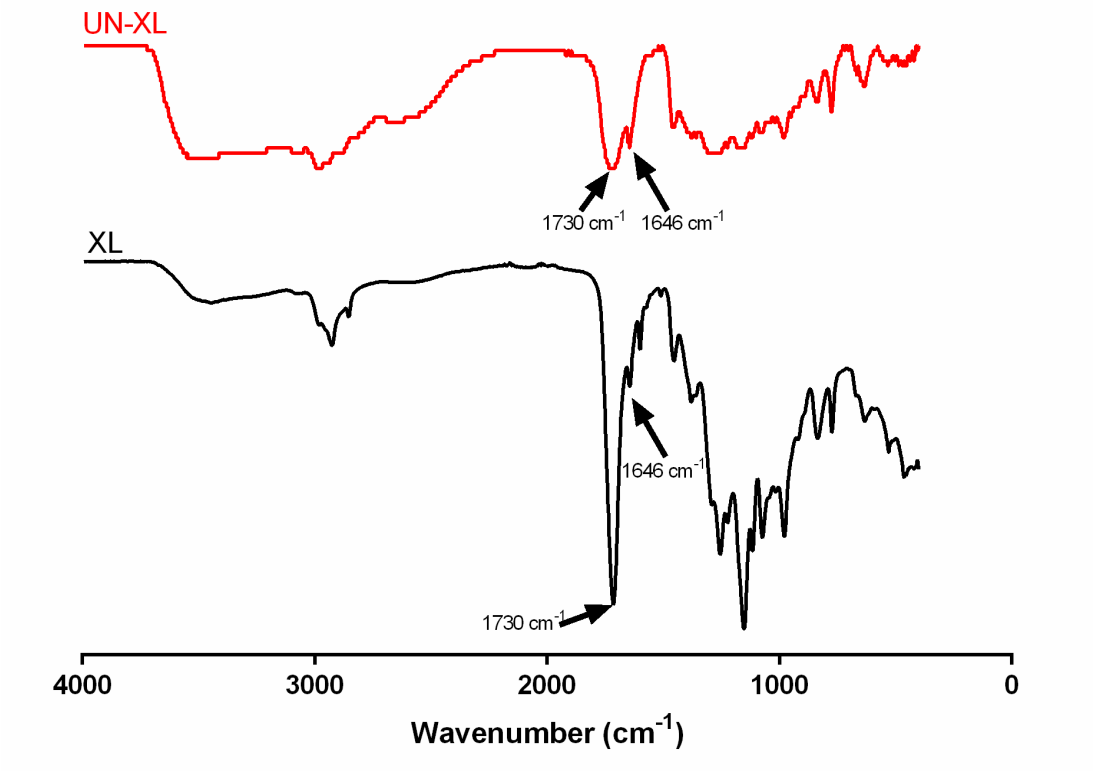

Figure 3.1. FTIR spectra of uncrosslinked (UN-XL) and crosslinked (XL) PPF.

3.1.2. Physical and Chemical Characterization of the Scaffolds

Custom designed 3D cylindrical PCL scaffolds were produced according to data obtained from Micro CT imaging of rabbit femur with a cylindrical defect. 3D printed PCL scaffolds were coated with HAp and HAp/PPF to increase the biological functionality.

Pore size, porosity, pore distribution, and surface chemistry are the factors that affect the osteoconduction, vascularization and *in vivo* bone growth (Bose et al., 2012 and Kim et al., 2010). In this study, basic (B) and basic shift (BS) PCL scaffolds were fabricated by changing the respective position of the deposited fibers or the pores with respect to each other. The scaffolds were observed under a stereomicroscope, SEM and Micro CT (Figure 3.2). Since the printing parameters (such as extrusion temperature and printing rate in the x and y directions) were kept constant, pore sizes

and fiber dimensions did not change significantly between B and BS scaffolds. In this study, the pore size in the scaffolds was found to be around 350 μm. In the literature, pore sizes in the range between 20 μm-1500 μm were reported in bone tissue engineering applications (Murphy et al., 2010). According to many studies, pores exceeding 300 μm lead to bone formation and vascularization (Karageorgiou et al., 2005; Kuboki et al., 2001; Roosa et al., 2010). Pores that are larger than 300 μm lead to direct osteogenesis by facilitating capillary formation. Porosities of the scaffolds were found to decrease from 35.08% to 26.29% as the shift distance increased up to 50%. Statistical analysis showed that porosities between basic (B) and basic shift (BS) ones [B-BS 0.25 (*$p<0.05$), B-BS 0.50 (**$p< 0.01$), BS 0.10-BS 0.25 (**$p< 0.01$), and BS 0.10-BS 0.50 (**$p< 0.01$)] were statistically significant. Since the fibers in the shifted structures could not be supported with the fibers of the underlying layers, the porosity of the BS scaffolds tended to be lower than the B ones because of the collapsing in the BS scaffolds. SEM, Micro CT and porosity analysis showed that B and BS 0.10 scaffolds were found to have higher porosity and more open pore structure compared to other BS scaffolds. This caused cell leakage during cell seeding and led to low cell adhesion. On the contrary, BS 0.20, BS 0.25 and BS 0.50 have less open pore structure which led to insufficient cell infiltration and therefore, less bone ingrowth. BS 0.15 PCL scaffolds were chosen for use in the following investigations since they had moderate porosity that would support cell attachment (*in vitro*) and bone ingrowth (*in vivo*) due to the interconnected open pores in their structures.

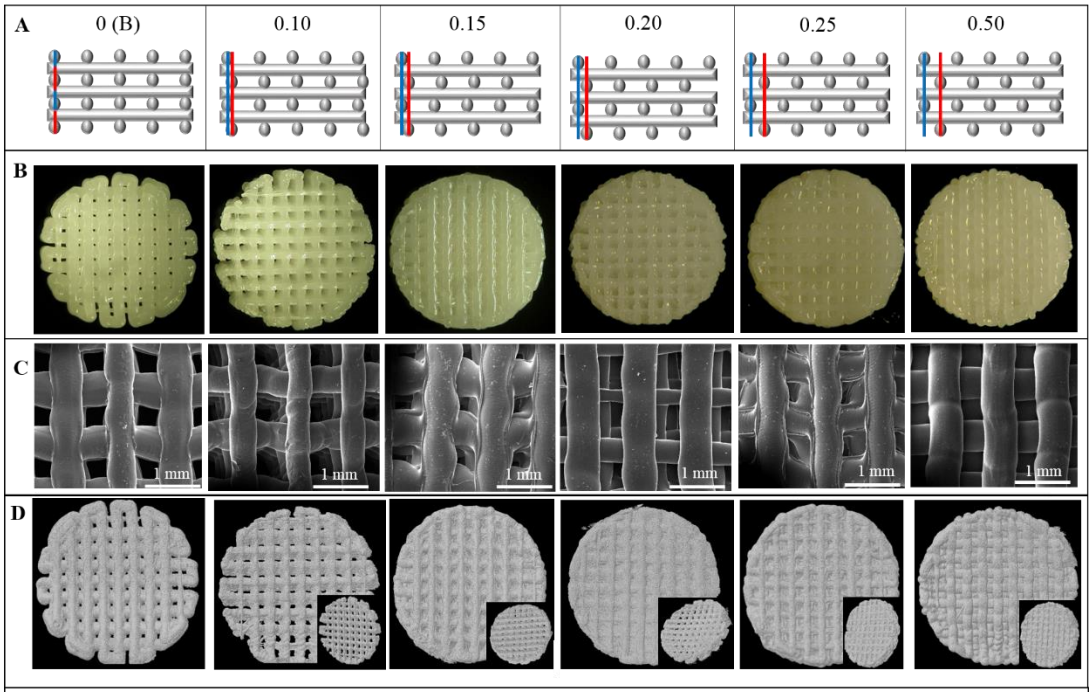

E

Shift Degree (mm)	B	BS				
	0	0.10	0.15	0.20	0.25	0.50
Fiber Diameter (µm)	573±53	549±39	562±67	585±41	512±32	587±27
Pore Size (µm)	360±42	326±60	339±30	368±23	342±39	370±21
Porosity (%)	35±2	36±1	31±4	30±2	27±2	26±3

Figure 3.2. Physical characterization of 3D printed B (0 mm) and BS (shifted 0.10, 0.15, 0.20, 0.25, 0.50 mm) PCL scaffolds.
A) Schematic representations of the PCL scaffolds in cross sectional views. B) Stereomicrographs, C) SEM micrographs, and D) Micro CT of the scaffolds as seen from the top. Insets show the models at an angle. E) Table of fiber diameters, pore size and porosity values of the B and BS scaffolds (n=3). The blue and red lines indicate the change of localization of the fibers in subsequent layers. Statistical analysis for porosity was carried out by using one-way ANOVA. The porosity differences for B-BS 0.25 (*p<0.05), B-BS 0.50 (**p< 0.01), BS 0.10-BS 0.25 (**p< 0.01), and BS 0.10-BS 0.50 (**p< 0.01) are statistically significant.

Composite scaffolds were prepared by coating the PCL scaffolds with HAp and with HAp/PPF. The microarchitecture, porosity and HAp distribution throughout the constructs were analyzed with SEM, Micro CT and EDS analyses (Figure 3.3A-J). Micro CT analysis confirmed that pure PCL scaffolds had no HAp particles and the others had it (Figure 3.3A). HAp particles were distributed homogeneously over the strands of the PCL/HAp and PCL/HAp/PPF scaffolds (Figure 3.3B and C). PCL/HAp scaffolds had higher Ca and P elements (Ca: 6.53% and P: 4.52%) than PCL/HAp/PPF scaffolds (Ca: 1.22% and P: 0.76%). This situation most probably arised from the covering and masking effect of PPF coat on HAp particle detection. According to Figure 3.3J, porosity of the scaffolds did not significantly change upon coating with HAp and PPF (PCL: 31±4%, PCL/HAp: 35±3% and PCL/HAp/PPF: 36±3%).

Water contact angles (WCA) were measured to investigate the wettability of the scaffolds (Figure 3.3K). Wettability is a surface characteristic which affects adhesion, proliferation and migration of cells on polymeric materials (Arima et al., 2007). It is stated in the literature that a moderately hydrophilic surface leads to a higher cell attachment compared to hydrophobic or highly hydrophilic surfaces (Diez-Pacual et al., 2016; Ozcan et al., 2008). It was found that untretated PCL scaffolds had higher WCA (80°) than the PCL/HAp (65°) scaffolds because of the ionic nature of HAp. WCA values of PPF containing scaffolds (50° at the first second, but then immediately decreased to 32° in 5 s) were even lower. Although PPF is a hydrophobic polymer, the addition of HAp nanoparticles to the structure apparently decreased its WCA dramatically. In the literature, it was reported that the WCA of crosslinked PPF was 69° and decreased to 35° upon the incorporation of HAp (Lee et al., 2008). We found similar change in hydrophilicity for the composite PCL/HAp and PCL/HAp/PPF scaffolds.

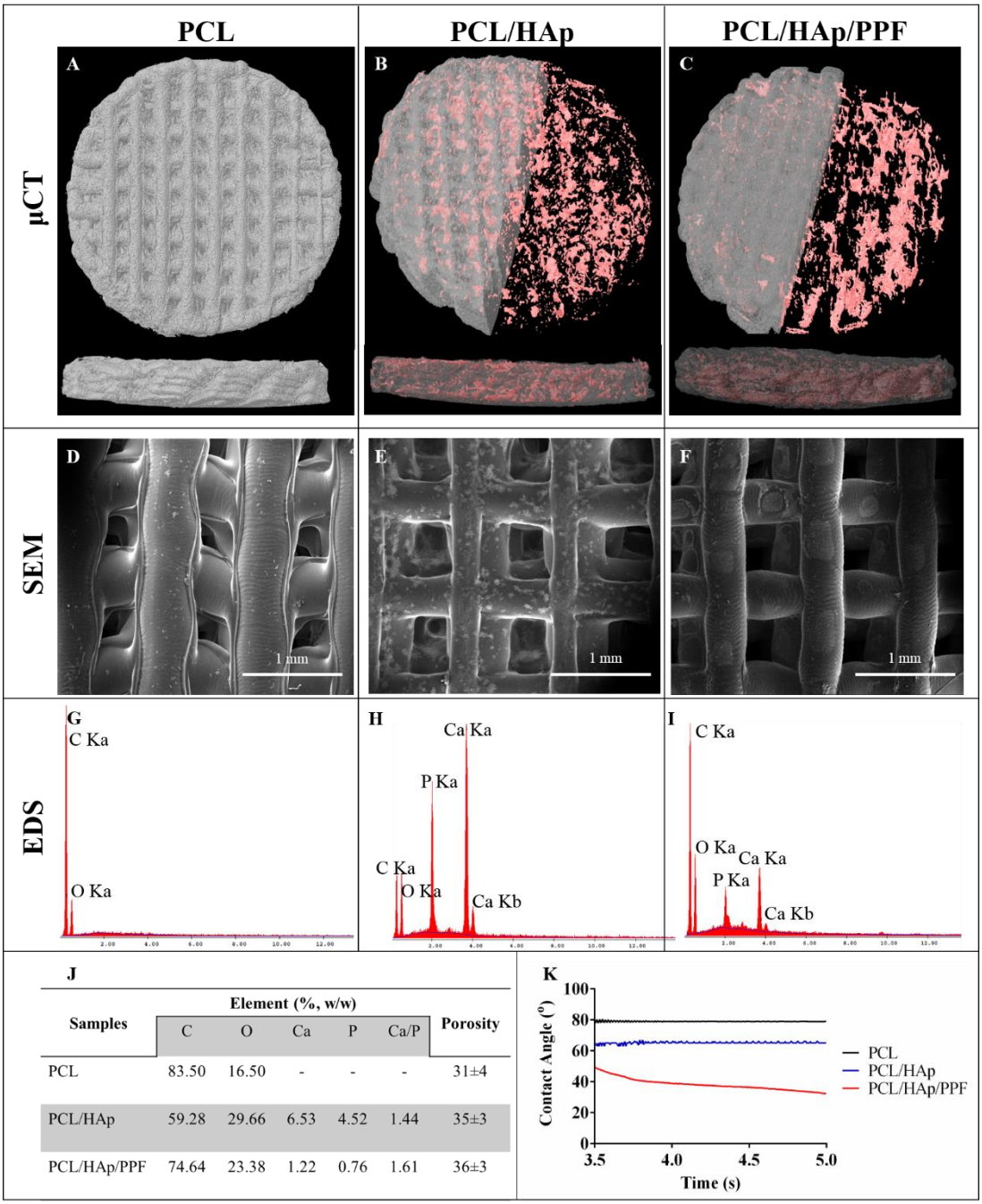

Figure 3.3. Physical and chemical characterization of the PCL, PCL/HAp and PCL/HAp/PPF scaffolds designed in BS 0.15 form.
A-C) Micro CT results (Top View and cross-section) and the distribution of the HAp particles in the scaffolds (red). The cross-section in z-direction shows the distribution of the HAp over the fibers. D-F) SEM micrographs of the scaffolds. G-I) EDS results showing the presence of Ca and P ions. J) EDS analysis for C, O, Ca and P elements and porosity values (n=3). K) Water contact angles of the scaffolds.
(PCL:A, D, G; PCL/HAp: B, E, H; PCL/HAp/PPF: C, F, I).

3.1.3. Evaluation of *In Situ* Degradation

Scaffolds used in tissue engineering applications are designed to degrade at a rate suitable for removal in a reasonable period while supporting the tissue that is undergoing regeneration. Therefore, the enzymatic degradations of the scaffolds were studied *in situ* in aqueous solutions of lipase, an enzyme secreted by the macrophages (Seyednejad et al., 2012). Lipase is adsorbed onto the polymer surface and cleaves the ester bonds of PCL because of its structural similarity to lipids (Mochizuki et al., 1997). The main factors that affect the degradation rate of the scaffolds are chemistry, morphology, and porosity. The weight loss profiles of the PCL based scaffolds are shown in Figure 3.4.

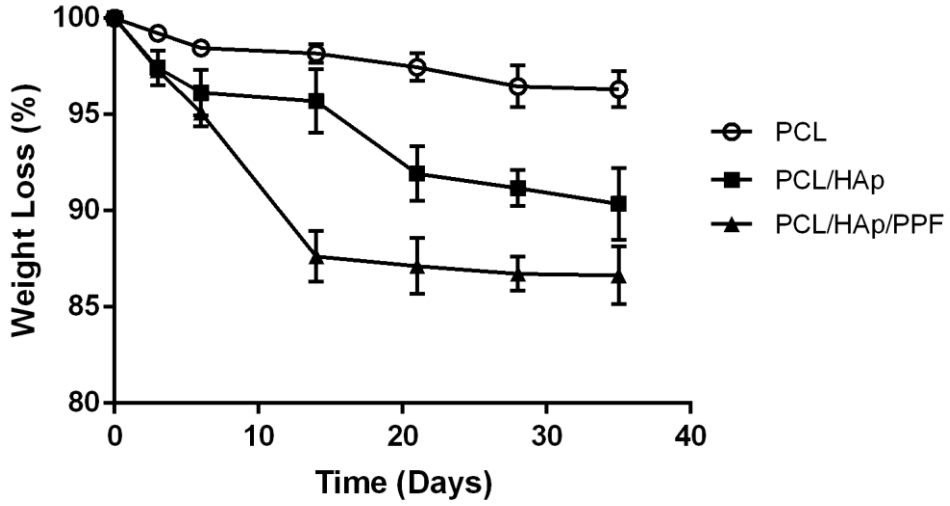

Figure 3.4. Weight loss of BS 0.15 scaffolds of PCL, PCL/HAp and PCL/HAp/PPF in aqueous lipase solution (180 U/L) in 35 days (n=3).

The rate of weight loss of the scaffolds significantly increased upon the incorporation of HAp onto the scaffolds. Incorporation of bioceramic molecules such as HAp into the polymers increases the degradation rate of the polymers, because the ceramic filler HAp act as “defects” and also enhance water absorption due to its ionic nature increasing the rate of media diffusion into the coat and also increase the surface area

for hydrolytic attack. Also, since the hydrophilicity of the scaffold increase, the invasion of enzyme and water into the scaffolds increase with the amount of HAp incorporation (Ito et al., 2005). The highest degradation rate was observed with PCL/HAp/PPF scaffolds because of the highest hydrophilicity as shown previously as a decrease in water contact angle values (Section 3.1.2).

3.1.4. Mechanical Analysis

Electromagnetic radiation is one of the most commonly used sterilization methods for tissue grafts. Irradiation with high energy gamma rays may lead to the formation of reactive intermediates on polymers and these intermediates are involved in several reaction pathways, which may cause crosslinking or scission of the polymer backbone or the side chains (Khan et al., 2013, Fawzy et al., 2011). Mechanical properties of the polymers are also affected by these reactions (Suarez et al., 2001). In this study, the effect of the gamma irradiation on the mechanical properties of the PCL-based scaffolds was investigated. Compression tests were performed before and after gamma irradiation and stress-strain curves were plotted (Figure 3.5). Similarity of the curves shows that mechanical properties of the scaffolds were not significantly affected by gamma irradiation.

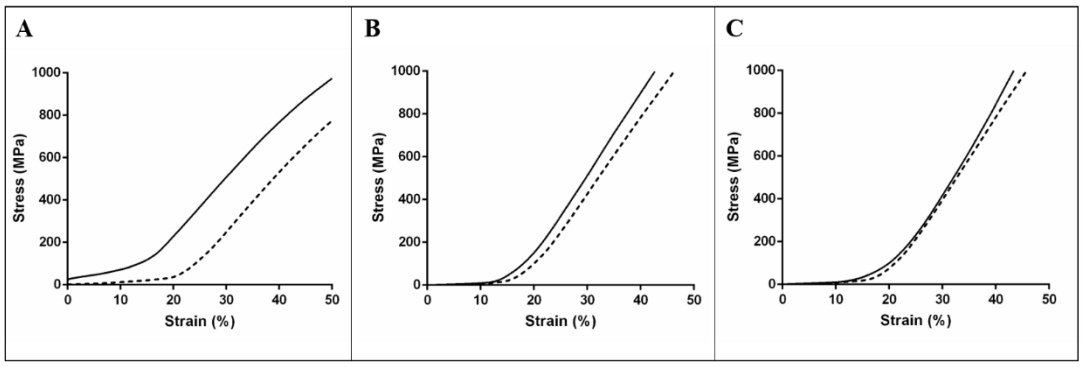

Figure 3.5. Stress-strain curves of A) PCL, B) PCL/HAp and C) PCL/HAp/PPF scaffolds before and after gamma irradiation (n=5).
(Solid line: Before, Dotted line: After irradiation).

Mechanical properties of the 3D printed scaffolds can be modulated by changing the fiber positions within the scaffold architecture (Hollister 2005, Yilgor et al., 2008). In this study, compression test was performed to study the effect of the scaffold design and chemical composition on the mechanical properties of the scaffolds (Figure 3.6). Change in fiber organization of the PCL scaffold from basic (B) to basic shift (BS 0.15) architecture led to a significant decrease in compressive modulus from 37.52±0.50 MPa to 22.80±1.29 MPa. The reason behind that decrease was the shifted fibers were not supported by the fibers of subsequent layers (Park et al., 2011).

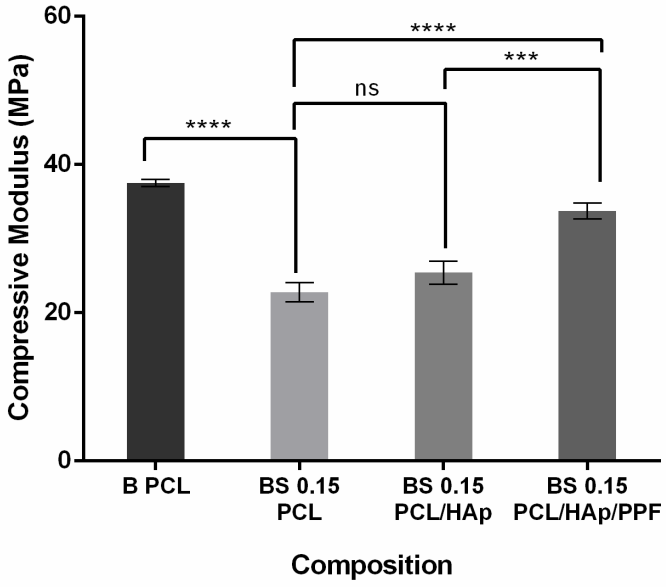

Figure 3.6. Compressive modulus of PCL (B and BS 0.15), and BS 0.15 scaffolds of PCL/HAp and PCL/HAp/PPF (n=5).
Statistical analysis was carried out by using one-way ANOVA. ***p<0.005, ****p<0.0001, and ns: not significant.

In Figure 3.6, it is seen that the addition of HAp coat onto the BS PCL scaffold did not change the compressive modulus, significantly. However, the compressive modulus increased from 22.80±1.29 MPa to 33.74±1.08 MPa upon HAp/PPF coating. According to the literature PPF-based composite materials have a compressive modulus in the range 23–265 MPa (Yan et al., 2011; Peter et al., 1998) depending on

the process and this strength is suitable to replace the human trabecular bone (Athanasiou et al., 2000).

3.1.5. *In Vitro* Studies

3.1.5.1. Cytotoxicity of the Scaffolds

The cytotoxicity test was carried out with the extracts of the scaffolds that were prepared by incubation of the scaffolds in the media in accordance with the ISO 10993-5 standard test method. L929 fibroblasts were used for the test and cell viability was measured with Alamar Blue cell proliferation assay. Figure 3.7 shows the number of cells which were cultured with the extraction media in comparison with those cultured with complete media as a control.

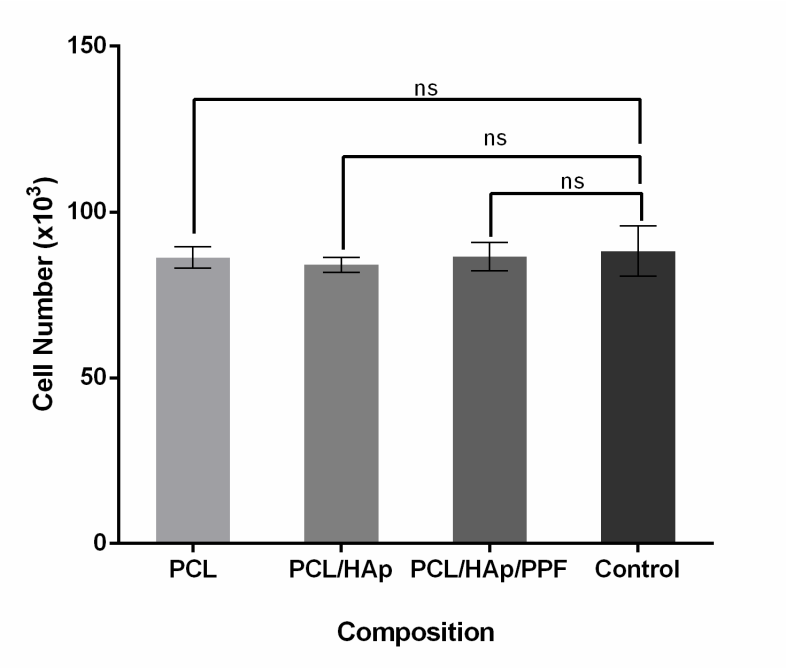

Figure 3.7. Cytotoxicity of PCL, PCL/HAp and PCL/HAp/PPF scaffolds using fibroblasts (L929) in accordance with ISO 10993-5 using the extracts after incubation of the scaffolds in the complete medium at 37ºC for 24 h (n=3). Control: L929 fibroblasts grown in DMEM High medium. Statistical analysis was carried out by using one-way ANOVA. ns: not significant.

The results presented in Figure 3.7 suggest that all the scaffolds were nontoxic, and none of the extracts presented any risk of cytotoxicity. PCL is a FDA approved

polymer for medical applications and there are many commercial PCL-based products; Monocryl (suture), Ellansé (dermal filler), Neurolac^{TM} (nerve guide), Resilon (root canal filling) are the main ones. The mineral component of the human bone is mostly HAp. PCL and HAp have earlier been used in bone tissue engineering without any cytotoxic effects (Lee et al., 2014). PPF has also been used for bone tissue engineering application. In 2013, Wang et al. showed that PPF had no cytotoxic effect on hMSC, L929, MC3T3, and cMSC cells. In a study of Luo et al. (2016), 3D printed PPF scaffolds were incubated with L929 fibroblasts and hMSCs and no cytotoxicity was observed. However, uncrosslinked PPF copolymers were shown to be highly cytotoxic (viability <3%) compared to crosslinked networks (viability>80%) (Timmer et al., 2003). Therefore, biocompatibility of the materials used in this study have already been proved, and we also observed no cytotoxicity.

3.1.5.2. BMSCs Proliferation on The Scaffolds

BMSCs proliferation was assessed using Alamar Blue cell viability assay which is based on cell metabolic activity. The effect of the inner architecture of PCL scaffolds (B and BS 0.15) on cell attachment efficiency and viability were compared (Figure 3.8). It was found that cell adhesion was significantly higher in the BS PCL scaffolds than the B PCL probably because of the larger contact area between the cells and the scaffold in BS construct. In the case of the basic structure, cell adherence is lower than that of the shifted scaffold because cells passed and leaked through the scaffold. Cells have more chance of contact in BS 0.15 PCL scaffolds due to the tortuous pathway of flow in these scaffolds, leading to higher initial adhesion and subsequent higher cell numbers. Yilgor et al. (2008) and Yeo et al. (2012) observed similar results for the scaffolds that have shifted fiber orientation. Therefore, for *in vitro* and *in vivo* experiments, BS 0.15 scaffolds were selected.

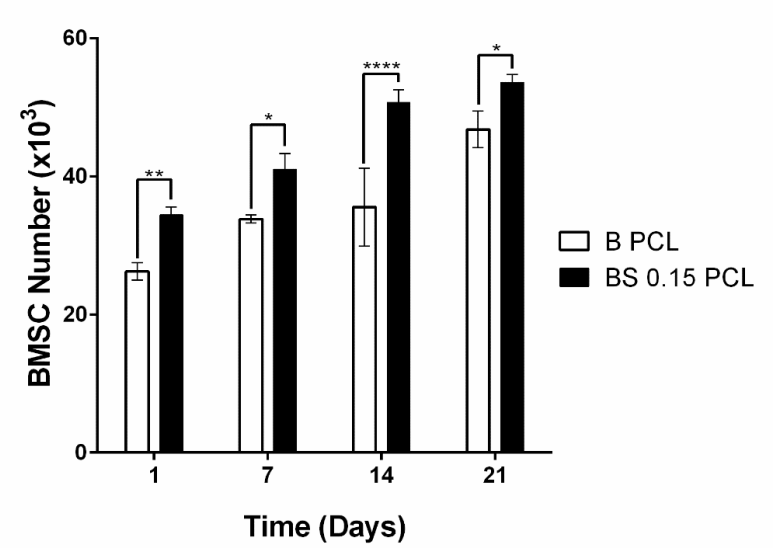

Figure 3.8. The change in the number of BMSC on PCL scaffolds (B and BS 0.15) as determined by Alamar cell viability test (n=3).
Statistical analysis was carried out by using one-way ANOVA. *p<0.05, **p<0.01, and ****p<0.0001.

The effect of the surface chemistry of the scaffold on BMSC viability was also evaluated (Figure 3.9).

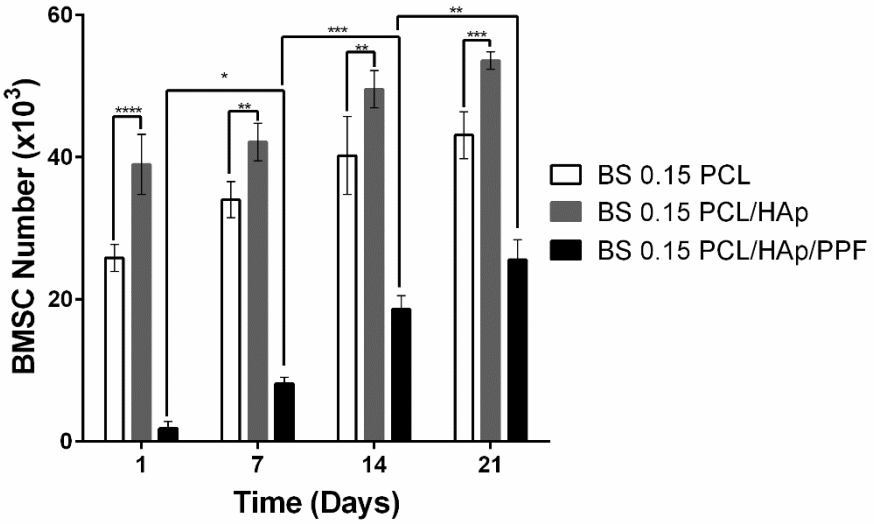

Figure 3.9. Viability of BMSC on PCL, PCL/HAp and PCL/HAp/PPF scaffolds as determined by Alamar cell viability test (n=3).
Statistical analysis was carried out by using one-way ANOVA. *p<0.05, **p<0.01, ***p<0.005, and ****p<0.0001.

Higher adhesion and higher cell numbers were observed for PCL/HAp scaffolds during 21 days of incubation (Figure 3.9). The feature of being osteoconductive of HAp nanoparticles improved cell adhesion and proliferation. Also, it was reported that HAp nanoparticles facilitate adsorption of specific serum proteins which helps and regulates the adhesion and proliferation of the cells (Chuenjitkuntaworn et al., 2010). In 2019, Fang et al. showed that HAp deposition on polyacrylamide/dextran hydrogel increased osteoblast adhesion and proliferation compared with unmineralized hydrogel, not only because of absorption of serum proteins, also because of the increased surface roughness. In a study of Kim et al. (2018), it was demonstrated that incorporation of HAp nanoparticles in PCL increased viability and proliferation of mesenchymal stem cells (MSCs) on 3D printed scaffolds. Also it was suggested that the positive effect of HAp on MSCs viability and proliferation was directly proportional with the concentration of HAp in the composite scaffolds.

However, in the presence of the PPF on the scaffolds the initial cell attachment of the cells was adversely affected (Figure 3.9). This is probably because of the increased hydrophilicity of the PCL/HAp/PPF scaffolds as mentioned in Section 3.1.2 (Figure 3.3K). Since the WCA decreased from 50° to 32° in 5 s, cells could not have time for attachment during the cell seeding process. Material surfaces should have moderate wettability with a water contact angle of 40°–70° for optimal cell adhesion (Oliveira et al., 2014 and Ozcan et al., 2007). Although cells adhered to the surface of PCL/HAp/PPF scaffolds much less than that on PCL and PCL/HAp scaffolds, the cell proliferation rate was almost 1.4 fold higher on PCL/HAp/PPF scaffolds compared with PCL and PCL/HAp scaffolds.

3.1.5.3. SEM Analysis of BMSCs on 3D Scaffolds

Cellular morphology of the BMSCs seeded on PCL, PCL/HAp and PCL/HAp/PPF scaffolds was investigated by SEM on day 21 of the cell culture (Figure 3.10). The results indicated that, cells attached, proliferated, and spread well on all scaffolds. BMSCs spread on the fibers and also spread across the fibers and attempted to fill the

pores of the scaffolds with secreted extracellular matrix (ECM). These observations indicate that the substrate surface properties are very suitable for BMSC adhesion regardless of surface chemistry.

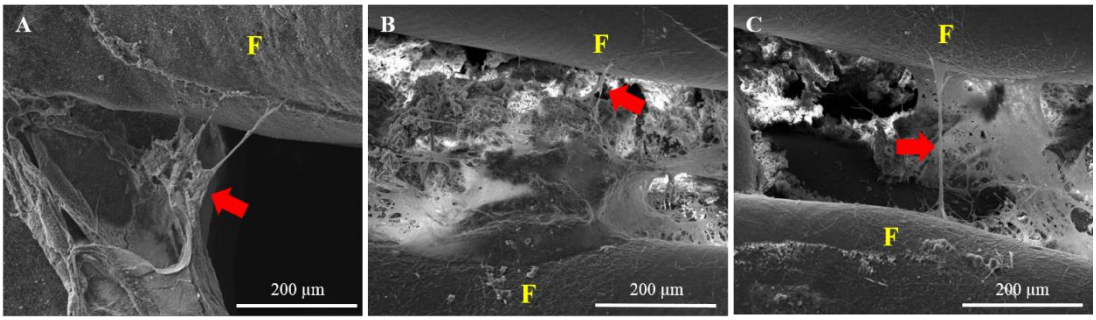

Figure 3.10. SEM of BMSCs seeded scaffolds.
A) PCL, B) PCL/HAp, and C) PCL/HAp/PPF (Day 21). F: Fibers of the scaffolds. Red arrow shows cells.

3.1.5.4. Osteogenic Differentiation

Osteogenic differentiation of BMSCs on the scaffolds was investigated with Alizarin Red, ALP assay, and quantitative RT-PCR analyses.

3.1.5.4.1. Alizarin Red Staining

BMSCs enter into the mineralization phase and deposit mineralized extracellular matrix (ECM) upon osteogenic differentiation. Alizarin Red (AR) staining was performed to demonstrate mineral deposition on days 7, 14 and 21. The stereomicrographs of BMSCs seeded scaffolds and cell free (control) scaffolds stained with AR are shown in Figure 3.11. It was observed that the formation of mineralized nodules of the BMSCs cultured on the PCL/HAp and PCL/HAp/PPF scaffolds were greater than that of the pure PCL scaffold. The increase in color intensity along 21 days showed that the calcium deposition of the cells on the scaffolds increased in time. Similarly, Chuenjitkuntaworn et al. (2010) compared PCL and PCL/HAp scaffolds prepared by solvent casting method, and reported that the presence of HAp on the scaffolds enhanced primary bone cell mineralization and supported the differentiation of the cells.

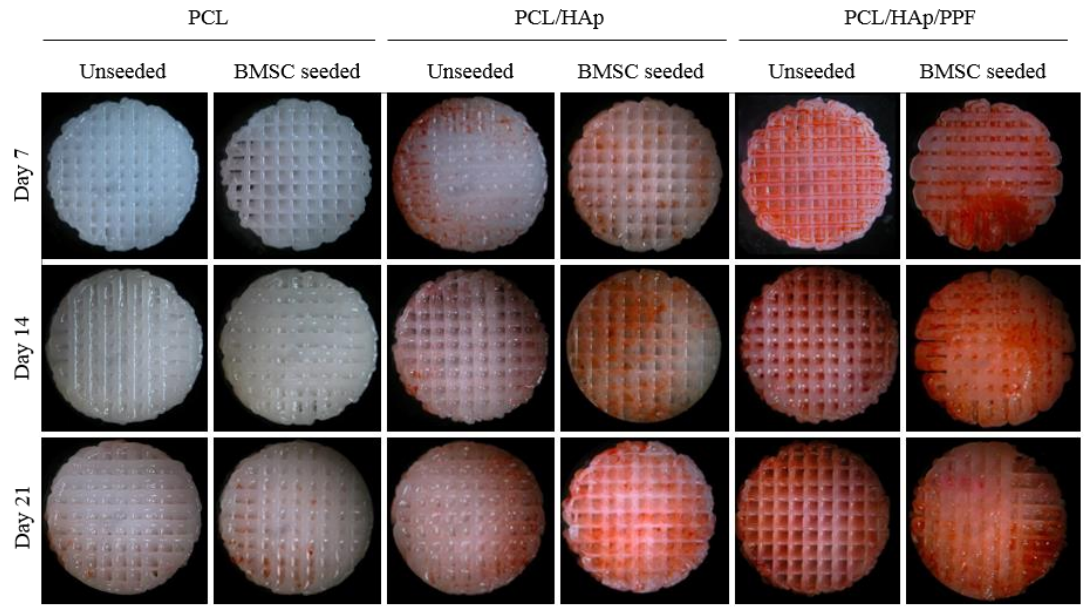

Figure 3.11. Stereomicrographs of the PCL, PCL/HAp and PCL/HAp/PPF scaffolds stained with Alizarin Red for HAp deposition on days 7, 14 and 21.

Kumar et al. (2015) compared injectable chitin-PCL and chitin-PCL-nHAp microgels in terms of differentiation of the rabbit adipose derived stem cells. They found that the cells in contact with the PCL-nHAp microgel had more foci of mineral deposition. According to Kumar et al. (2015), apart from the osteoinductive property of the nHAp particles, nHAp particles also increases the surface area which leads to increase the number of nucleation points for the mineral deposition by the cells.

3.1.5.4.1. ALP Assay

Alkaline phosphatase enzyme (ALP) is a membrane associated enzyme and early indicator of osteogenic differentiation (An et al., 2004). ALP plays a significant role in the induction of hydroxyapatite deposition on ECM proteins and the catalytic activity of ALP is required for normal skeletal calcification (Anderson et al., 2004). ALP concentrations of the BMSCs on the PCL based scaffolds were measured on days 7, 14 and 21 (Figure 3.12) to evaluate the osteogenic differentiation.

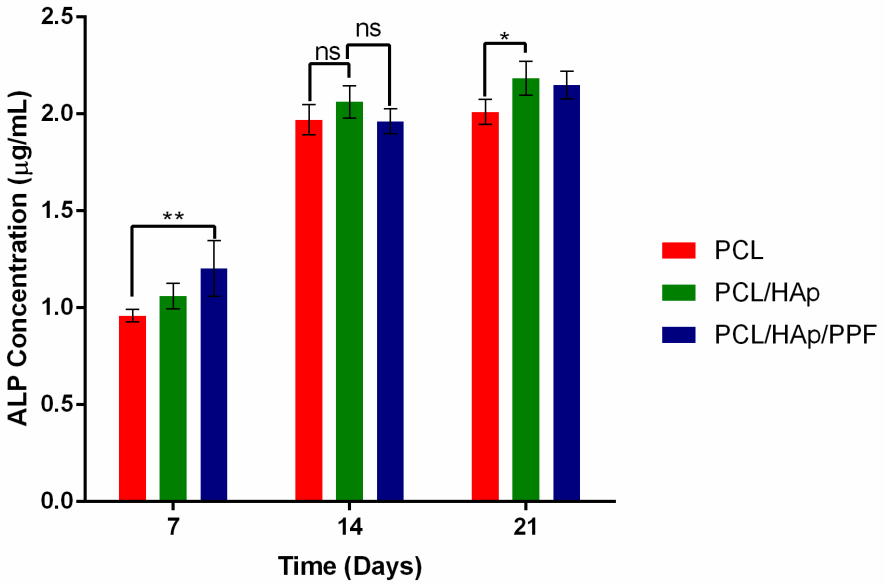

Figure 3.12. ALP concentration of BMSCs on PCL, PCL/HAp and PCL/HAp/PPF scaffolds (n=3). Statistical analysis was carried out by using two-way ANOVA. *p<0.05, **p<0.01, and ns: not significant.

The analysis of ALP revealed that the cells on the scaffolds showed a rise of ALP level between days 7 and 14 for all scaffolds and thereafter reached a plateau which shows the initiation of biomineralization. ALP is increased in the early stages of biomineralization and induce hydroxyapatite mineralization. After the initial mineralization there is no longer need for ALP, so that cellular levels of the enzyme decreases before a mature mineralized matrix is formed (Storrie et al., 2005). In the literature, similar results as, a rise and fall in ALP of the MSCs were reported (Porter et al., 2009; Shin et al., 2004). In Figure 3.12, it is seen that the ALP concentration of the HAp containing scaffolds was higher than that of the PCL scaffold especially on days 7 and 21 which is due to the osteogenic feature of the HAp (Wei et al., 2011). Fernández et al. (2014) also showed that the addition of HAp into PCL and polydiisopropyl fumarate blend increased the cellular expression of ALP.

3.1.5.4.1. Quantitative Real-Time Polymerase Chain Reaction (qRT-PCR)

In addition to ALP production and alizarin red staining, osteogenic differentiation of BMSCs on the scaffolds was also investigated by studying the genes RUNX2, COL1A1 and SPP1 as a molecular approach. RUNX2 is an early differentiation factor that is expressed in the condensed mesenchymes. Cells that express RUNX2 segregate from osteochondroprogenitors to form precursor osteoblasts. During bone formation, osterix (an osteoblast-specific transcription factor) is expressed from these precursors which induce the differentiation of the cells into mature and functional osteoblasts, and finally into osteocytes (Sinha et al., 2013). RUNX2 gene has also an important role in the production and regulation of bone matrix proteins. Figure 3.13 shows the RUNX2 expression of BMSCs on the PCL based scaffolds on days 3, 7, 14 and 21 of incubation. While the expression of RUNX2 of the cells on the PCL scaffolds did not significantly change during the whole culture time, the presence of HAp/PPF onto the scaffold upregulated the RUNX2 expression from day 3 to day 21 due to the osteoinductive property of HAp (Ganesh et al., 2014). The expression of RUNX2 of the cells on PCL/HAp/PPF scaffolds was higher than the other two groups for all measured days of the culture. Interestingly, for the PCL/HAp/PPF scaffolds, RUNX2 transcription factor expression decreased from day 3 to day 7, and increased from day 7 to day 21. In a study of Kim et al., (2011) this down- and following upregulation pattern was explained with the effect of low cell seeding density. They compared PPF and PPF/HAp scaffolds with low and high cell seeding densities in terms of gene expression. According to the results of the study, the expression of RUNX2 for the scaffolds with low cell seeding density decreased from day 1 to day 4 and increased from day 4 to day 8. Similarly, in this current study, cell seeding efficiency of PCL/HAp/PPF scaffolds was very low compared to the PCL and PCL/HAp scaffolds because of the increased hydrophilicity of the PCL/HAp/PPF scaffolds as mentioned in Section 3.1.5.2.

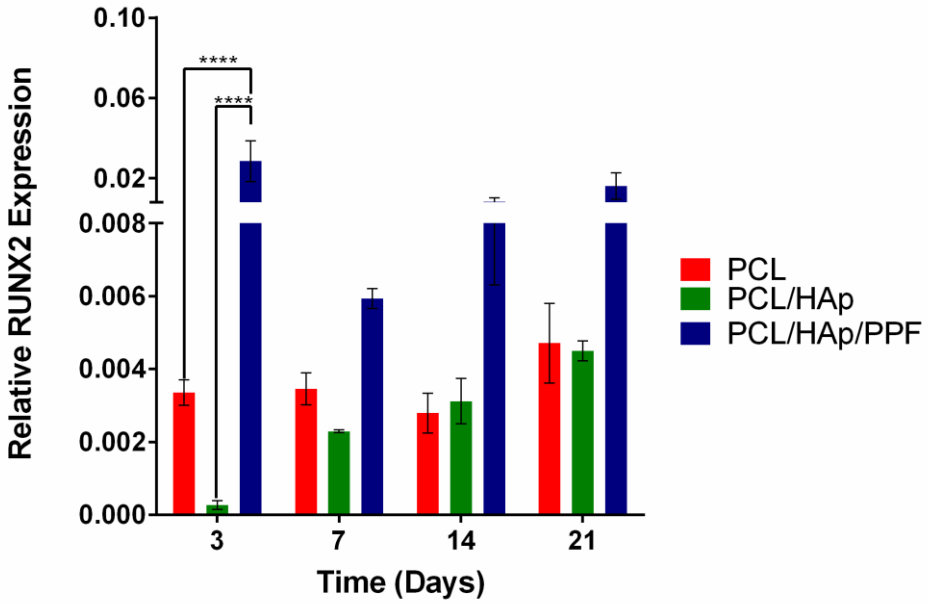

Figure 3.13. Quantitative RT-PCR results for RUNX2 gene expression of the BMSCs on PCL, PCL/HAp and PCL/HAp/PPF scaffolds (n=3).
Statistical analysis was carried out by using two-way ANOVA. *p<0.05, **p<0.01, ***p<0.005, ****p<0.0001, and ns: not significant

Collagen, especially collagen type 1 (COL1A1), is the most abundant protein in the bone matrix and is one of the indicators of osteogenic differentiation (Chuenjitkuntaworn et al., 2009). Figure 3.14 shows the COL1A1 expression of BMSCs on the PCL based scaffolds on days 3, 7, 14 and 21 of incubation. COL1A1 expression decreased from day 3 to day 7, and increased from day 7 to day 14 for all groups. Dormer et al. (2011) observed this fluctuating expression for human BMSCs on PLGA scaffolds and PLGA with 5% HAp constructs. They explained this observation as the fluctuating expression of COL1A1 in control and low HAp containing samples could be representative of a cyclic process of osteoblast matrix and mineral production. Also, Kang et al. (2014) showed that 10% HAp incorporation in PCL electrospun scaffolds, enhances osteogenic differentiation. In Figure 3.14, it is also seen that the expression of COL1A1 of BMSCs on PCL/HAp/PPF scaffolds was significantly higher than on other groups especially on days 14 and 21.

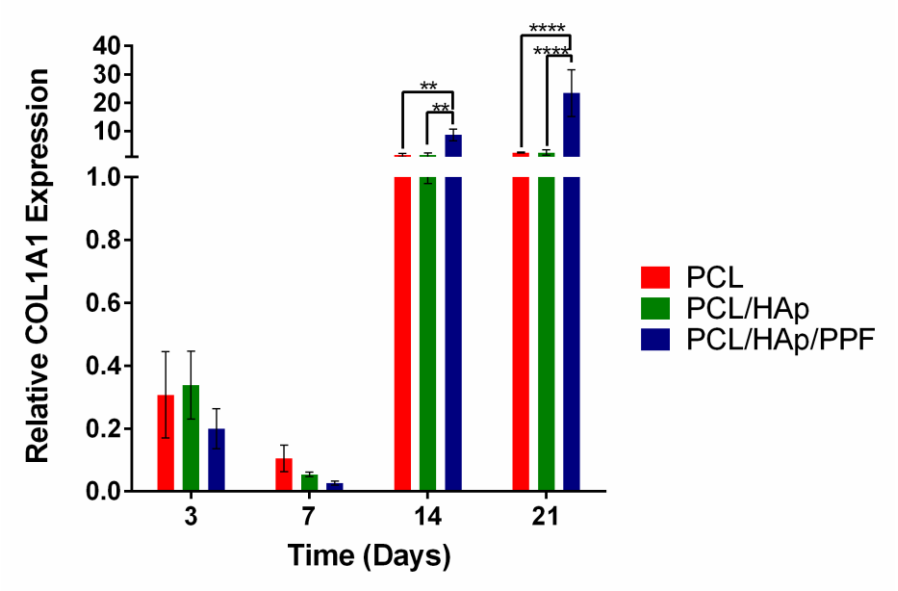

Figure 3.14. Quantitative RT-PCR results for COL1A1 gene expression of the BMSCs on PCL, PCL/HAp and PCL/HAp/PPF scaffolds (n=3).
Statistical analysis was carried out by using two-way ANOVA. *p<0.05, **p<0.01, ***p<0.005, ****p<0.0001, and ns: not significant.

Although the role of osteopontin (SPP1) in the regulation of MSC differentiation has not been fully understood, it has been known that SPP1 is secreted from MSCs and upregulated during osteogenic differentiation (Chen et al., 2014). SPP1 is upregulated during the cell proliferation phase and after the initial mineralization of ECM (Kim et al., 2010). SPP1 plays an important role in the clearance of debris by macrophage phagocytosis and the formation of new bone at the edges of the bone defects during bone repair. Figure 3.15 shows the SPP1 expression of BMSCs on the PCL based scaffolds on days 3, 7, 14 and 21 of incubation.

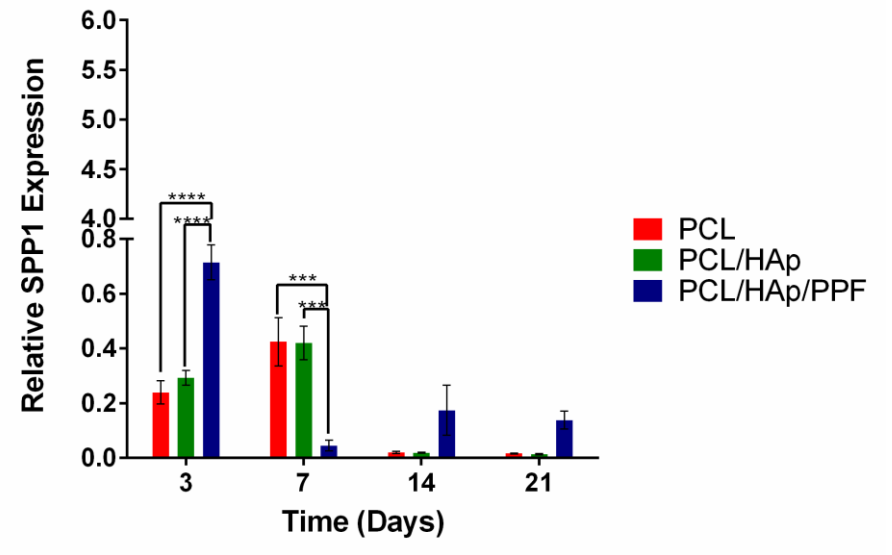

Figure 3.15. Quantitative RT-PCR results for SPP1 gene expression of the BMSCs on PCL, PCL/HAp and PCL/HAp/PPF scaffolds (n=3).
Statistical analysis was carried out by using two-way ANOVA. *p<0.05, **p<0.01, ***p<0.005, ****p<0.0001, and ns: not significant.

SPP1 expression of BMSCs increased from day 3 to day 7, and decreased from day 7 to day 21 for PCL and PCL/HAp scaffolds. SPP1 expression of BMSCs on PCL/HAp/PPF scaffolds decreased significantly from day 3 to day 7, and then did not change significantly. Kim et al. (2010) showed that cells on 3D printed PCL/HAp scaffolds displayed a higher level of SPP1 expression than that of PCL scaffolds on day 10.

3.2. 3D Printed GelMA and PCL/GelMA Hybrid Scaffolds

3.2.1. ^{1}H-NMR of GelMA

Gelatin was methacrylated by using methacrylic anhydride. The degree of methacrylation (DM) is the ratio of ε-amino groups (lysine, hydroxylysine) of methacrylated gelatin to unreacted pure gelatin prior to the reaction (Hoch et al., 2012). The ^{1}H NMR spectra were normalized to the phenylalanine signal (6.9-7.5 ppm) since it is proportional with the concentration of the gelatin and is not reacted during methacrylation. DM was calculated through the integrated areas of lysine

methylene signals (2.8-2.95 ppm) of gelatin and GelMA. The DM was calculated as 85±9% for the synthesized GelMA (Figure 3.16).

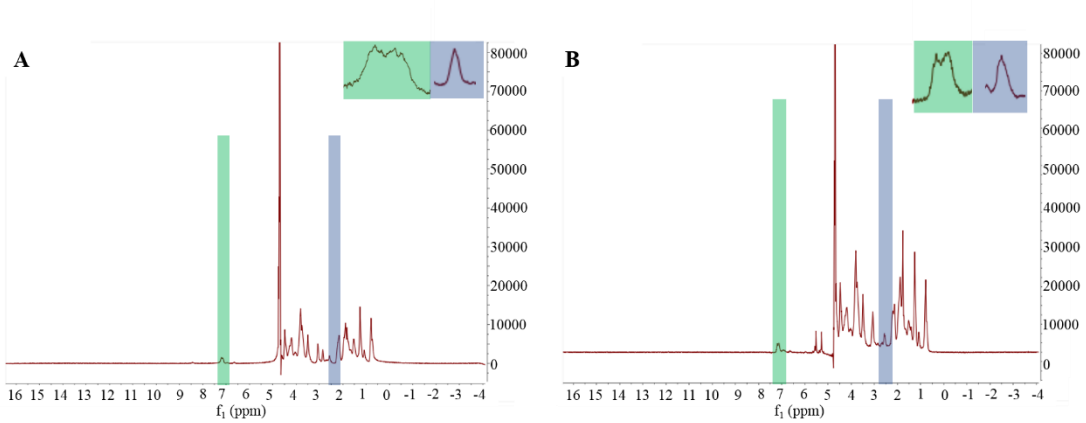

Figure 3.16. ^{1}H-NMR spectra of A) gelatin, and B) uncrosslinked gelatin methacrylamide (GelMA). The green region between 7.50 and 6.90 ppm is the phenylalanine signal and the blue region between 2.95 and 2.80 ppm is the lysine methylene signals.

3.2.2. Microscopic Evaluation of PCL/GelMA Hybrid Scaffolds

The microarchitecture of the hybrid constructs was examined with a stereomicroscope, SEM and Micro CT (Figures 3.17 and 3.18). In order to have acceptable images, GelMA fibers were stained with Brilliant Blue after printing (Figure 3.17A). PCL was printed in well defined shapes as parallel fibers with meandering corners and the fibers were straight. PCL fibers had uniform thickness throughout the scaffold. GelMA was printed between the PCL struts. For SEM analysis, scaffolds were freeze dried (Figures 3.17B and C). PCL fiber diameter was calculated as 674±44 μm. Porous structure of GelMA and separation of PCL and GelMA at the boundaries upon drying was observed after freeze drying.

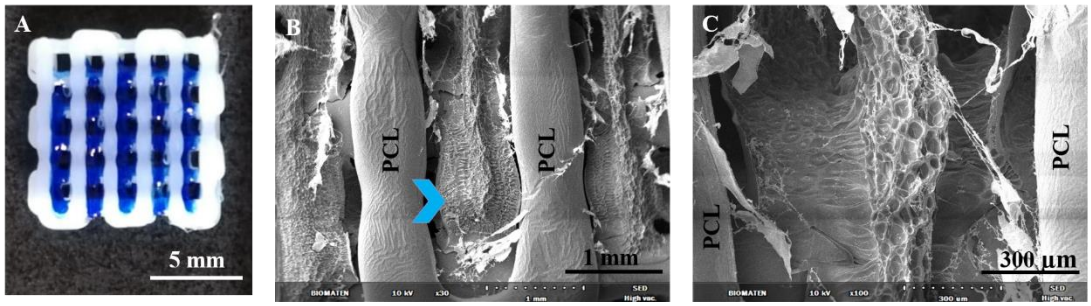

Figure 3.17. Stereomicrograph and SEM micrographs of PCL/GelMA hybrid scaffold.
A) Stereomicrograph of PCL/GelMA scaffold (10x10x1.5 mm^3). GelMA was stained with Brilliant Blue after printing to make it visible. Scanning electron micrograph of A) PCL/GelMA scaffold (10 x10 x1.5 mm^3) (30X magnification) and B) GelMA fiber between the PCL struts (100X magnification). Blue arrowhead shows the printed GelMA fiber.

Micro CT images of the constructs are shown in Figure 3.18. PCL/GelMA scaffolds were printed by loading with HAp to make the hydrogel visible during Micro CT analysis. The white particles are HAp nanoparticles in GelMA and the gray fibers around them are PCL struts in Figure 3.18A. In Figure 3.18B, HAp nanoparticle loaded GelMA is seen as green and the red fibers are PCL struts. According to the Figure 3.18, GelMA was printed between the PCL fibers in both x and y direction.

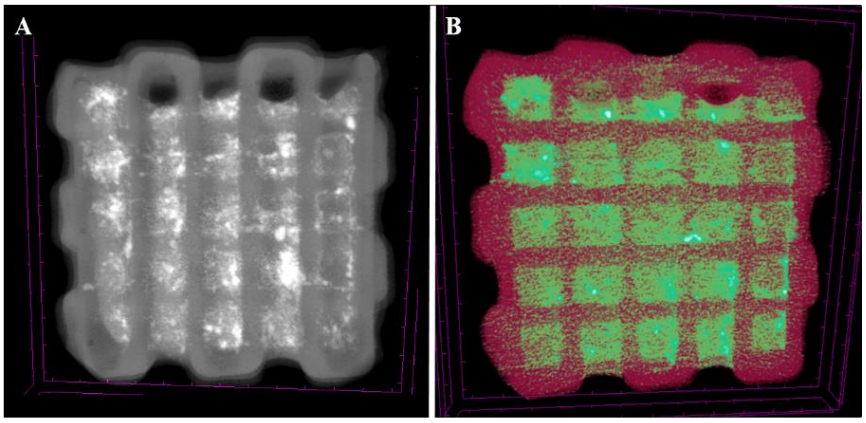

Figure 3.18. MicroCT images of PCL/GelMA hybrid scaffold.
A) Maximum intensity projection image, and B) Colored image of HAp loaded scaffold (10x10x1.5 mm^3).

3.2.3. *In situ* Degradation

Degradation of the scaffolds under culture conditions gives an idea about the scaffold stability under biological conditions. 3D printed PCL/GelMA, 3D printed GelMA scaffolds and GelMA slabs were incubated in PBS (pH 7.4, 10 mM), taken out at certain time intervals, freeze-dried and weighed (Figure 3.19).

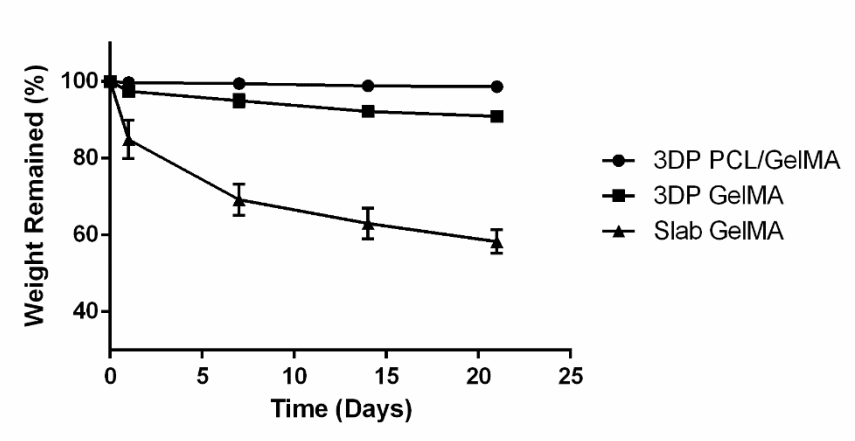

Figure 3.19. In situ degradation of 3D printed PCL/GelMA (10x10x1.5 mm^3), 3D printed GelMA scaffolds (10x10 x1.5 mm^3) and GelMA slabs (diameter: 10 mm, height: 1.5 mm) in PBS at 37°C (n=3).

Since the degradation rate of the PCL is too low to observe during 21 days under *in situ* conditions, the observation is more dependent on weight loss of the gel part of the hybrid scaffold. The degradation rate of the 3D printed GelMA (10x10x1.5 mm^3) was significantly higher than that of 3D printed PCL/GelMA (10x10x1.5 mm^3) on days 7 (**$p<0.001$), 14 (****$p<0.0001$) and 21 (****$p<0.0001$). This is because PCL fibers prevent the diffusion of water at a certain level, so that water can not reach the gel part. It was observed that around 2% of the GelMA in the hybrid scaffold was degraded at the end of 21 days of incubation which shows that the material is stable enough to be used in the *in vitro* studies.

GelMA slabs (diameter: 1 cm, height: 1.5 mm) were used as a control and 42% of the gel was degraded at the end of 21 days of incubation. The degradation rate of the

GelMA slabs was significantly higher than that of the 3D printed GelMA scaffolds. This is probably because of the lower crosslinking density of the slabs. Since the slabs has more gel material per unit area, UV penetration was significantly lower when compared with the 3D printed GelMA.

3.2.4. Equilibrium Water Content (EWC) of GelMA

Hydrogels are crosslinked networks of hydrophilic polymers that can absorb high amount of water many times of their original mass. The samples immersed in distilled water, removed after 24 h, the wet and swollen samples were weighed. The EWC of 3D printed PCL/GelMA, 3D printed GelMA scaffolds, and GelMA slabs were compared (Figure 3.20).

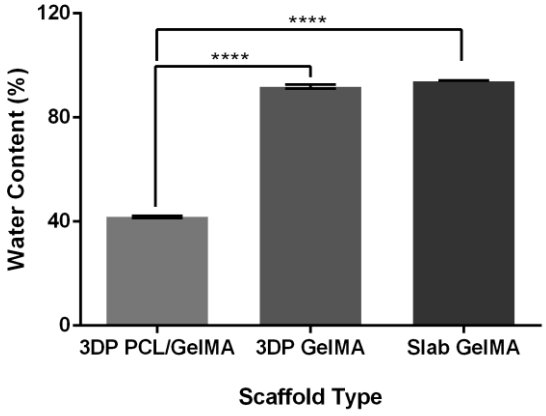

Figure 3.20. Equilibrium water content of 3D printed GelMA, PCL/GelMA scaffolds and slab GelMA after 24 h incubation in distilled water (n=3).
Statistical analysis was carried out by using one-way ANOVA. *p<0.05, **p<0.01, ***p<0.005, ****p<0.0001, and ns: not significant.

GelMA in the PCL/GelMA hybrid scaffolds reached equilibrium swelling after about 24 h with the degree of swelling (DS) of 41±1%. Since PCL does not absorb water, this amount is directly absorbed by GelMA present in scaffold. The water content of 3D printed GelMA (91±1%) and GelMA slab (93±1%) was significantly higher than that of PCL/GelMA scaffolds. PCL fibers in the hybrid scaffold might prevent water

penetration in the scaffold, so that the water retention capacity of GelMA significantly decreased.

3.2.5. Compressive Mechanical Test

3D printed GelMA, PCL and PCL/GelMA scaffolds were exposed to compression tests and compressive moduli of the scaffolds were calculated from the initial slope of the stress-strain curves (Figure 3.21).

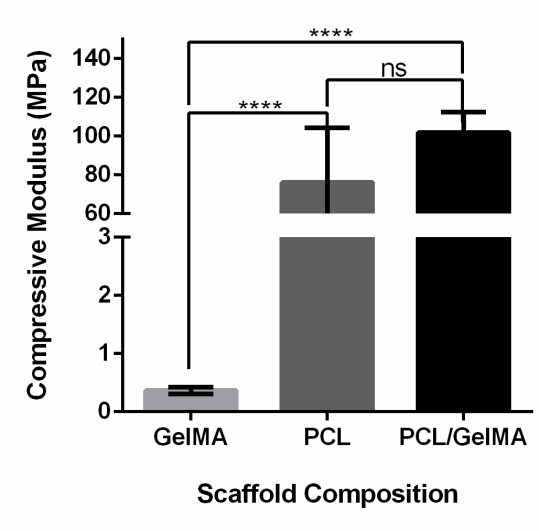

Figure 3.21. Compressive modulus of 3D printed GelMA, PCL and PCL/GelMA scaffolds (n=5). Statistical analysis was carried out by using one-way ANOVA. ****p<0.0001, and ns: not significant.

Compressive moduli of the GelMA scaffolds (0.36±0.05 MPa) were significantly lower than that of the PCL (76±28 MPa) and PCL/GelMA (102±10 MPa) scaffolds. There was no significant difference between the compressive moduli of PCL and PCL/GelMA scaffold which indicated that the strength of the scaffold was based on the PCL, and the presence of GelMA hydrogel between the PCL fibers did not contribute to the mechanical properties of the constructs. Similarly, Dong et al. (2017) reported that incorporation of chitosan hydrogels in 3D printed PCL scaffolds did not contribute the mechanical property. Similarly, Schuurman et al. (2011) printed alginate hydrogel between the PCL fibers and observed that there was no contribution

of the hydrogel to the mechanical properties of the scaffold. Both of the PCL and PCL/GelMA scaffolds are suitable to replace the human trabecular bone which has a compressive elastic modulus of 50–100 MPa (Athanasiou et al., 2000).

3.2.6. *In vitro* studies

3.2.6.1. Flow Cytometry of DPSCs

According to The Mesenchymal and Tissue Stem Cell Committee of the International Society for Cellular Therapy (ISCT), there are 3 main criteria to define MSC: 1) adherence to plastic, 2) expression of specific surface antigens (expression of CD105, CD73 and CD90; and lack expression of CD45, CD34, CD14 or CD11b, CD79α or CD19), and 3) multipotent differentiation potential (Dominici et al., 2006). The expression of surface markers CD31, CD45, CD90 and CD105 of DPSCs were analyzed with flow cytometry. Hematopoietic CD45 (Leukocyte common antigen) and endothelial CD31 (PECAM) are used as negative markers since they are absent in MSCs. CD90 (Thy-1) is a surface protein which is responsible for cell-cell and cell-ECM interactions. CD105 (SH2, endoglin) is a mesenchymal adhesion molecule. The cells were incubated with IgG1κ isotype control to detect any nonspecific interaction between the cell surface and the Fc (constant) region of the antibodies used. Also, the fluorescence intensity of unstained cells was compared with the stained cells. No nonspecific binding was detected as the fluorescence intensity of cells stained with isotype control highly overlapped (99.92%) with the intensity of unstained cells (Figure 3.22). Isolated DPSCs were found to be negative for the markers CD45 (0.80%) and CD31 (0.13%). Cells displayed positive expression for the mesenchymal markers CD105 (99.77%) and CD90 (99.92%). The expression profiles were consistent with other studies in the literature (Hasturk et al., 2019; Perry et al., 2008; Khanna-Jain et al., 2012).

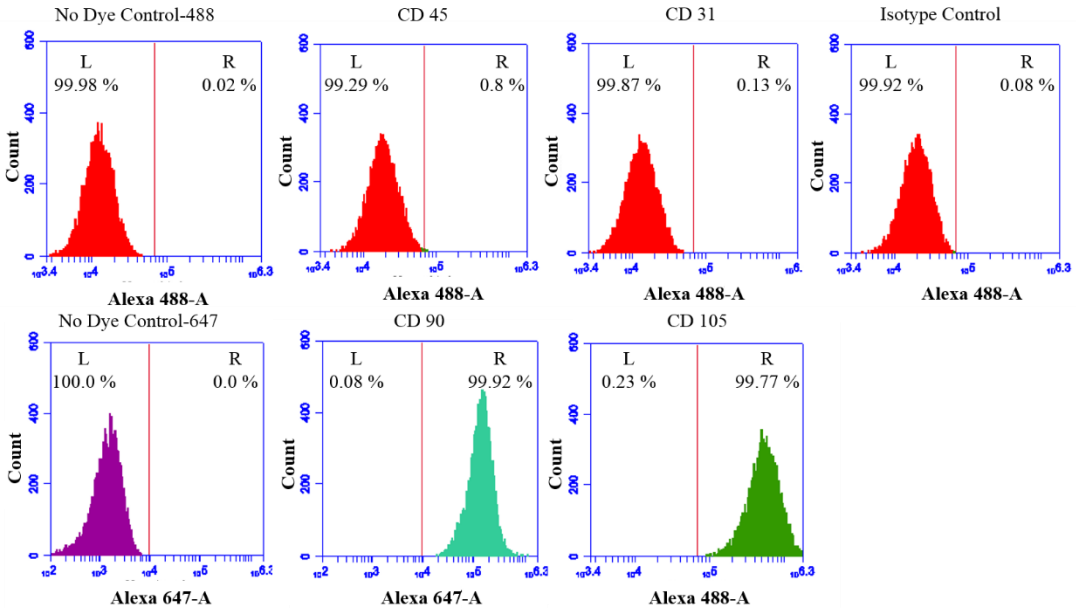

DPSCs Passage 4	Negative Quadrant	Std. Dev.	Positive Quadrant	Std. Dev.
No Dye Control-488	99.98 %	$7.07x10^{-5}$	0.02 %	$7.07x10^{-5}$
No Dye Control-647	99.9 %	$4.07x10^{-5}$	0.01 %	$4.07x10^{-5}$
Isotype Control	99.9 %	$4.x10^{-4}$	0.1 %	$4.x10^{-4}$
CD 45	99.29 %	6.7×10^{-3}	0.8 %	6.7×10^{-3}
CD 31	99.87 %	7×10^{-4}	0.13 %	7×10^{-4}
CD 90	0.08 %	4×10^{-4}	99.92 %	4×10^{-4}
CD 105	0.23 %	1.1×10^{-2}	99.77 %	1.1×10^{-2}

Figure 3.22. Flow cytometry analysis of the expression of surface markers by DPSCs stained with CD45, CD31, antimouse IgG1 isotype control, CD90 and CD105 antibodies along with the controls (n=3).

3.2.6.2. L929 Fibroblast Loaded, 3D Printed GelMA Scaffolds

L929 fibroblast is the most commonly used cell line for preliminary studies to study cytocompatibility of hydrogel and effect of printing parameters on cell viability (Lai et al., 2016; Blaeser et al, 2016; Suntornnond et al., 2017). In this study, L929 fibroblasts were loaded in GeLMA at a density of $1x10^6$ cells/mL and the viability of the cells was assessed with live/dead assay on days 1, 4 and 8 (Figure 3.23). ImageJ analysis revealed that more than 90% of the cells in the GelMA were alive on days 1 and 4. In a study of Bektas et al. (2017) high cell density ($1x10^6$ cells/mL) in

GelMA was used similarly to this study to enable cells to interact with each other. Bahcecioglu et al. (2019) reported high fibrochondrocyte viability (around 80%) in GelMA hydrogels on day 1. This high cell viability is the result of the presence of biologic recognition sites (arginine-glycine-aspartic acid (RGD) sequences) which enhances adhesion and proliferation of the cells on gelatin.

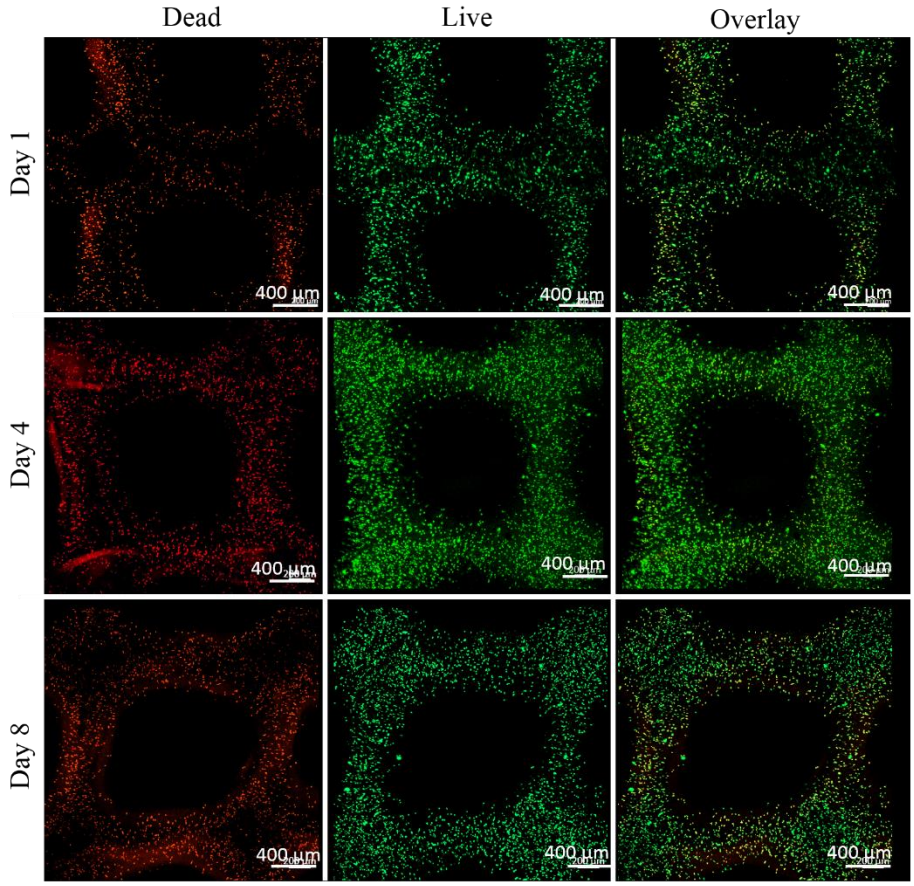

Figure 3.23. Live/Dead Assay of L929 fibroblast loaded GelMA, studied with CLSM. Calcein AM: Live Cells, green; Ethidium Homodimer: Dead Cells, red.

3.2.6.3. DPSC Loaded, 3D Printed PCL/GelMA Hybrid Scaffolds

3.2.6.3.1 Live/Dead Assay

Viability of the DPSCs was evaluated with Live/Dead assay on days 0, 7, 14 and 21 (Figure 3.24). In order to assess the effect of the printing parameters on cell viability, live/dead assay was conducted on day 0 (Figure 3.24) and it was found that the printing parameters did not affect the cell viability. Cell number increased significantly from day 0 to 7 showing the ability of GelMA to support cell proliferation due to its RGD binding sites. However, cell number decreased on days 14 and 21, which was probably due to the degradation of GelMA. Since GelMA degraded, cells that were loaded in GelMA were washed out during medium changing steps.

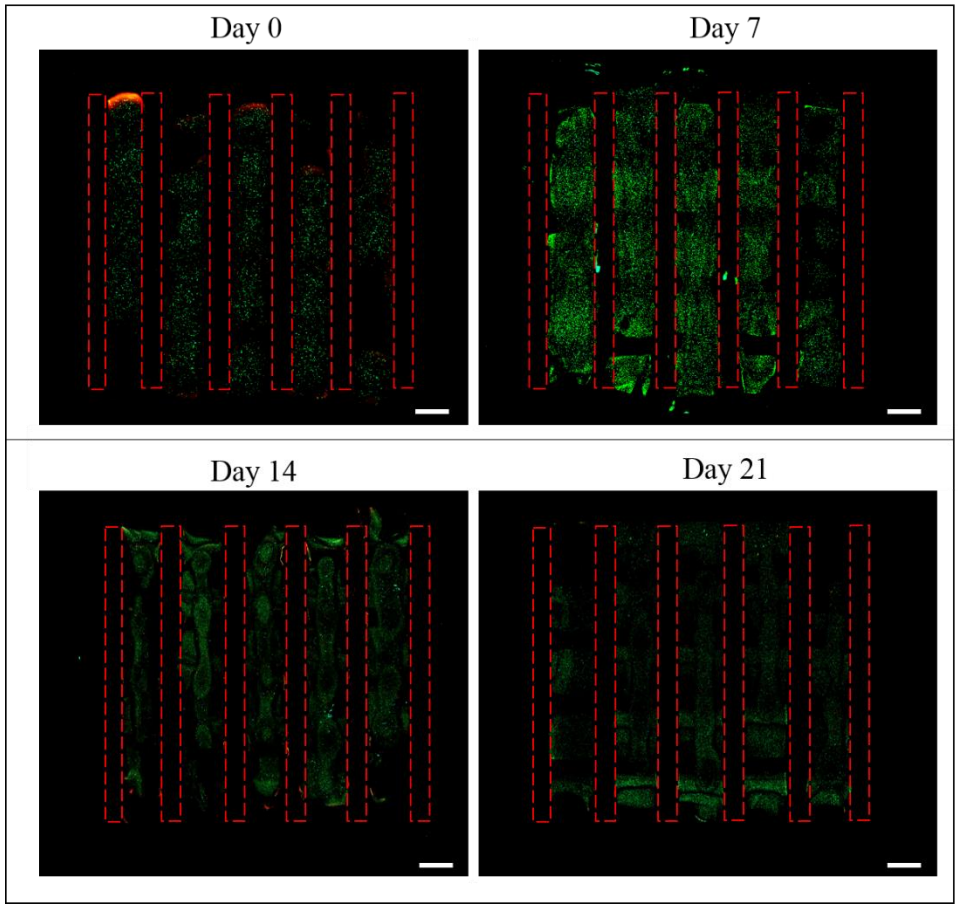

Figure 3.24. Live/Dead Assay of DPSC loaded PCL/GelMA, studied with CLSM. Calcein AM: Live Cells, green; Ethidium Homodimer: Dead Cells, red. Red dotted rectangles show the PCL fibers. Scale bar: 1 mm.

Although, only 2% of the GelMA in the hybrid scaffold was degraded at the end of 21 days of incubation during *in situ* degradation studies (Section 3.2.3, Figure 3.19), significantly faster degradation was observed during *in vitro* studies due to the presence of enzymes that were produced by the cells. However, in the case of implantation of cell loaded scaffolds *in vivo*, the degradation of the GelMA would not be a problem since the cells in the degraded gel will still be present at the host area and will not be washed out. Also, the rapid degradation of the GelMA in the hybrid scaffold enables new tissue formation while the remaining PCL supports additional mechanical support for the newly forming tissue (Dong et al., 2017).

3.2.6.3.2 Phalloidin Staining

Distribution of the DPSCs in the cell loaded PCL/GelMA scaffolds was observed on days 7, 14 and 21 under a CLSM microscope (Figure 3.25). The homogeneous cell distribution in GelMA was observed on day 7. However, cell number significantly decreased on days 14 and 21 due to the degradation of the GelMA as mentioned in Section 3.2.6.3.1. Since the gel itself was stained with phalloidin, the irregular shape of the gel due to the degradation was observed on days 14 and 21.

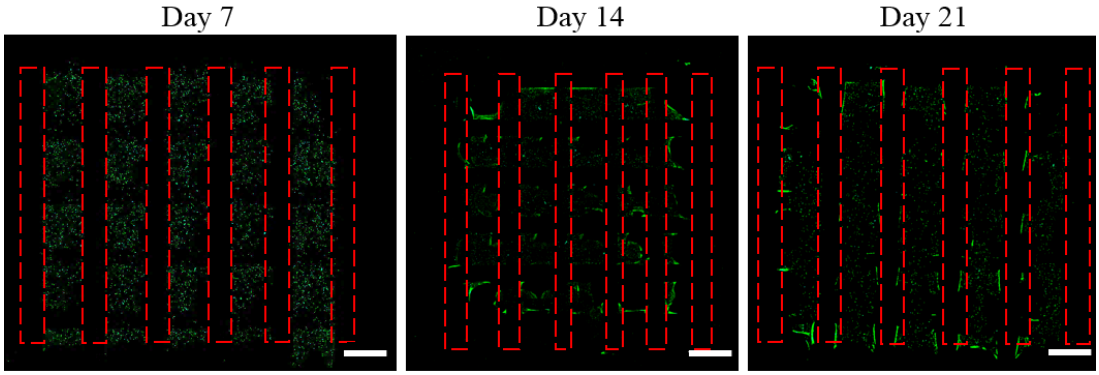

Figure 3.25. Phalloidin staining of DPSC loaded PCL/GelMA, studied with CSLM. Phalloidin: Cytoskeleton, green. Red dotted rectangles show the PCL fibers. Scale bar: 1 mm.

3.2.6.3.3 Osteogenic Differentiation

3.2.6.3.3.1 Alizarin Red Staining

Alizarin Red (AR) staining was performed to demonstrate mineral deposition of DPSCs upon osteogenic differentiation on days 7, 14 and 21. The stereomicrographs of DPSCs loaded PCL/GelMA scaffolds and cell free (control) scaffolds stained with AR are presented in Figure 3.26. Mineralized nodules of the DPSCs in the PCL/GelMA scaffolds were observed on day 21. Deposition of Ca and P ions were quantified with Energy dispersive X-ray spectroscopy (EDS) (Figure 3.27). DPSCs entered into the mineralization phase after day 14. Ca (0.14%, w/w) and P (0.37%, w/w) deposition was observed on day 21. Results of AR staining revealed that osteogenic differentiation of DPSCs in 3D GelMA hydrogel was enhanced.

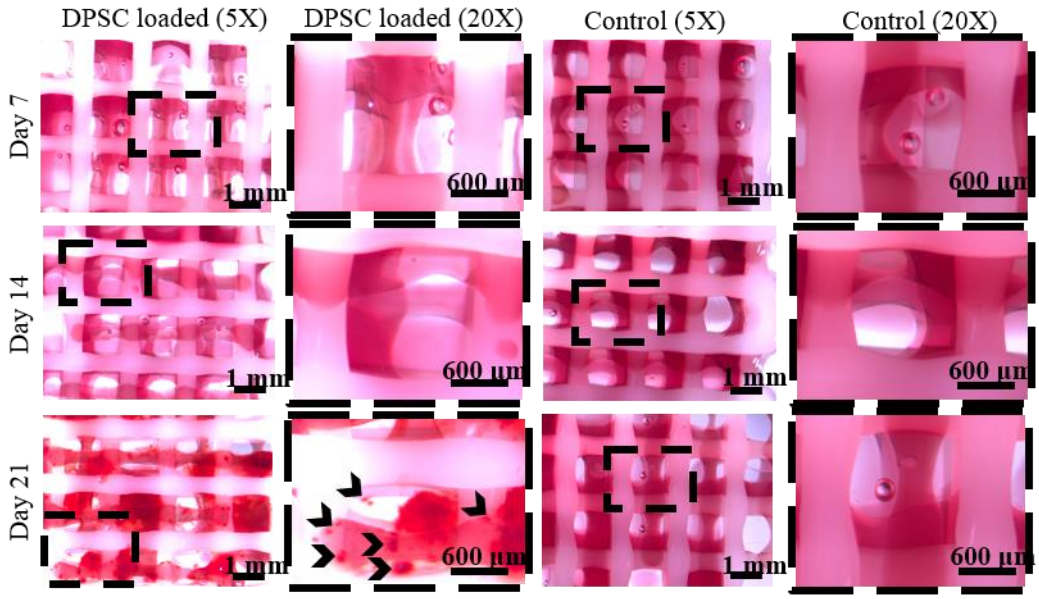

Figure 3.26. Stereomicrographs of the Alizarin Red staining of DPSC loaded PCL/GelMA and the control (cell free PCL/GelMA). Black arrow heads show CaP deposition.

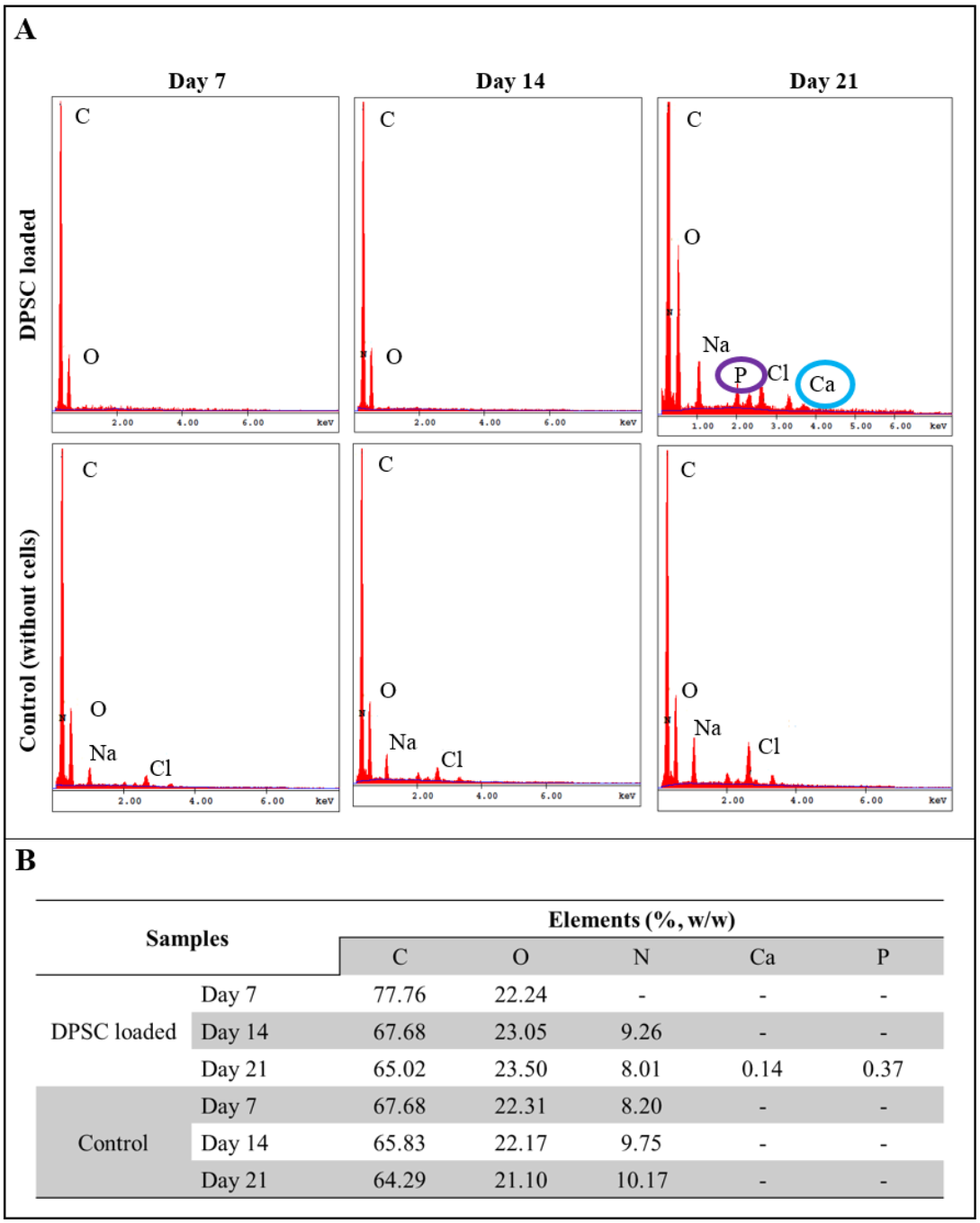

B

Samples		Elements (%, w/w)				
		C	O	N	Ca	P
DPSC loaded	Day 7	77.76	22.24	-	-	-
	Day 14	67.68	23.05	9.26	-	-
	Day 21	65.02	23.50	8.01	0.14	0.37
Control	Day 7	67.68	22.31	8.20	-	-
	Day 14	65.83	22.17	9.75	-	-
	Day 21	64.29	21.10	10.17	-	-

Figure 3.27. EDS analysis of the Alizarin Red staining of DPSC loaded PCL/GelMA on days 7, 14 and 21. A) Energy dispersive X-ray spectra showing the presence of Ca and P ions. B) Table of EDS analysis for C, O, N, Ca and P elements (n=3).

3.3. *In vivo* Studies

Results of *in situ* mechanical tests and *in vitro* studies of PCL based composite scaffolds showed that PCL/HAp and PCL/HAp/PPF scaffolds had sufficient strength to substitute for bone tissue. Also, they were quite stable, noncytotoxic and had osteogenic features due to the HAp in their composition. Therefore, these scaffolds were chosen for testing *in vivo* to study their biocompatibility and suitability for bone tissue regeneration.

3.3.1. *In vivo* Biocompatibility Tests

3.3.1.1. Intracutaneous Irritation Test

The skin has various types of immune cells that perform innate and acquired immunity and when the skin contacts irritants, symptoms like erythema and edema are observed (Chen et al., 2011). Intracutaneous irritation tests of PCL, PCL/HAp and PCL/HAp/PPF scaffolds were carried out at TÜBİTAK Marmara Research Center (MAM). The tests were performed according to the protocol of ISO 10993-10 (Biological evaluation of medical devices-Part 10: Tests for irritation and skin sensitization) which defines the approach for *in vivo* biocompatibility testing. Extracts of the scaffolds in polar and nonpolar solvents were injected intradermally to New Zealand albino rabbits. The scores determined were 0.13, 0.11 and 0.20 (Table 3.1A) for PCL, PCL/HAp and PCL/HAp/PPF scaffolds, respectively. These scores indicated that there was negligible irritation due to the scaffolds. In the literature extracts of PCL, HAp and PPF were studied separately for their irritation of the skin and it was found that neither of them caused irritation (Kaplan et al., 2016; Geetha et al., 2013; Jayabalan et al., 2009).

3.3.1.2. Implantation Test

Although PCL is a widely used polymer in FDA approved devices, PCL based composite scaffolds have to be evaluated for their effects when implanted subcutaneously. PCL, PCL/HAp and PCL/HAp/PPF scaffolds were implanted

subcutaneously in rats and implantation sites were observed after 28 days. These tests were carried out at TÜBİTAK Marmara Research Center (MAM). The severity scoring method is based on the number and type of inflammatory cells found at the implantation site. After 28 days all the severity scores of the PCL, PCL/HAp and PCL/HAp/PPF scaffolds were lower than the lowest limit of 2.9, it was concluded that the scaffolds induced no inflammatory response according to ISO 10993-6 (Biological evaluation of medical devices-Part 6: Tests for local effects after implantation) (Table 3.1B). In 2012, Ghanaati et al. implanted HAp granules subcutaneously in rats and studied the early and late inflammatory responses for 30 days at four time points (on days 3, 10, 15 and 30). Histological and histomorphometrical analyses showed that, HAp in granula form (100-350 μm) leads to low levels of early and late inflammation. Fisher et al. (2002), implanted PPF scaffolds subcutaneously in New Zealand white rabbits. Histological and histomorphometrical analysis were performed at the end of 8 weeks and minimal fibrous encapsulation was observed. Sitharaman et al. (2008), implanted porous PPF scaffolds subcutaneously in New Zealand White rabbits and histological scores for tissue response were around 1.00, which is very similar to the score (1.67 for PCL/HAp/PPF scaffolds) obtained in this study.

Table 3.1. *Scores of in vivo biocompatibility tests of PCL, PCL/HAp and PCL/HAp/PPF scaffolds.*

A. Irritation scores

Sample and Extraction Solvent	**Test Site**	**Score**
PCL (polar)	left anterior site	0
Polar solvent control	left posterior site	0
PCL (non-polar)	right anterior site	0.13
Non-polar solvent control	right posterior site	0
PCL/HAp (polar)	left anterior site	0
Polar solvent control	left posterior site	0
PCL/HAp (non-polar)	right anterior site	0.11
Non-polar solvent control	right posterior site	0
PCL/HAp/PPF (polar)	left anterior site	0
Polar solvent control	left posterior site	0
PCL/HAp/PPF (non-polar)	right anterior site	0.20
Non-polar solvent control	right posterior site	0

Mean severity score values: 0= no erythema/edema, 1= very little erythema/edema (noticed barely), 2= distinguishable erythema/edema, 3= moderate erythema/edema, 4= severe erythema/edema.

B. Implantation scores

Sample	**PCL**						**PCL/HAp**						**PCL/HAp/PPF**					
Criteria	**Test Sample**			**Control**			**Test Sample**			**Control**			**Test Sample**			**Control**		
Inflammation	0	0	0	0	0	0	0	0	0	0	0	0	0	0	0	0	0	0
Polymorphonuclear cells	1	1	1	0	0	1	0	0	0	0	0	0	0	0	0	0	0	0
Lymphocytes	0	0	0	0	0	0	1	1	1	0	0	1	1	1	1	0	0	1
Plasma cells	0	0	0	0	0	0	0	0	0	0	0	0	0	0	0	0	0	0
Macrophages	0	0	0	0	0	0	0	0	0	0	0	0	0	0	0	0	0	0
Giant cells	0	0	0	0	0	0	0	0	0	0	0	0	0	0	0	0	0	0
Necrosis	0	0	0	0	0	0	0	0	0	0	0	0	0	0	0	0	0	0
Sub-Total	1	1	1	0	0	1	1	1	1	0	0	0	1	1	1	0	1	1
New angiogenesis	0	1	0	0	0	0	1	0	0	0	0	0	0	0	0	0	0	0
Fibrosis	1	1	1	0	1	1	1	1	1	0	1	1	0	1	1	1	0	0
Fatty infiltration	0	0	0	0	0	0	0	0	0	0	0	0	0	0	0	0	0	0
Sub-Total	1	2	1	0	1	1	2	1	1	0	1	1	0	1	1	1	0	0
TOTAL	2	3	2	0	1	2	3	2	2	0	1	1	1	2	2	1	1	1
AVERAGE	**2.33**			1.00			**2.33**			0.67			**1.67**			1.00		

Mean severity score values: 0-2.9=not irritant, 3.0-8.9= low irritant, 9.0-15.0=moderately irritant, >15.0 very irritant.

3.3.2. Evaluation of *In vivo* Bone Tissue Regeneration

3.3.2.1. Micro CT Analysis

BMSC seeded PCL/HAp and PCL/HAp/PPF scaffolds and unseeded controls were implanted orthotopically into the femoral defects of the New Zealand white rabbits in order to investigate the osteoinductive and osteoconductive potentials of the scaffolds and the level of regeneration. Micro CT analysis was performed to determine the extent of new mineralized tissue formation (Figure 3.28). Empty defect was used as the control. Bone regeneration was at a minimum level for these controls with regions of very low mineralization at the edges of the defect even after 8 weeks of implantation. BMSC free (unseeded) PCL/HAp scaffold implanted femurs displayed better coverage of the defects with respect to control. After 8 weeks, there was new bone formation growing from the edges towards the center of the defect. In Figure 3.28, it is seen that seeding BMSCs on the scaffolds before the implantation, enhanced bone regeneration as expected. It was also observed that the BMSC seeded PCL/HAp/PPF scaffold implanted femurs displayed the greatest closure at the defect site at the end of 4 and 8 weeks (Figure 3.28). It is well known that MSCs promote bone formation in orthotopic defects *in vivo* (Oryan et al., 2018; Rai et al., 2010; Dupont et al., 2009) due to the secretion of growth factors and cytokines that initiate a therapeutic outcome (Caplan, 2009). Qi et al. (2016) compared PCL scaffolds with HAp coated PCL scaffolds by evaluating new bone formation within a defect region in the calvarial bone of Sprague Dawley rats. After 8 weeks of implantation, PCL/HAp implanted femurs displayed better closure than pristine PCL implanted femurs. Likewise, Shim et al. (2017) showed that surface coating of biphasic calcium phosphate (mixture of HAp and β-TCP) nanoparticles on 3D printed PCL scaffolds enhanced bone regeneration after 8 weeks of implantation with respect to untreated PCL.

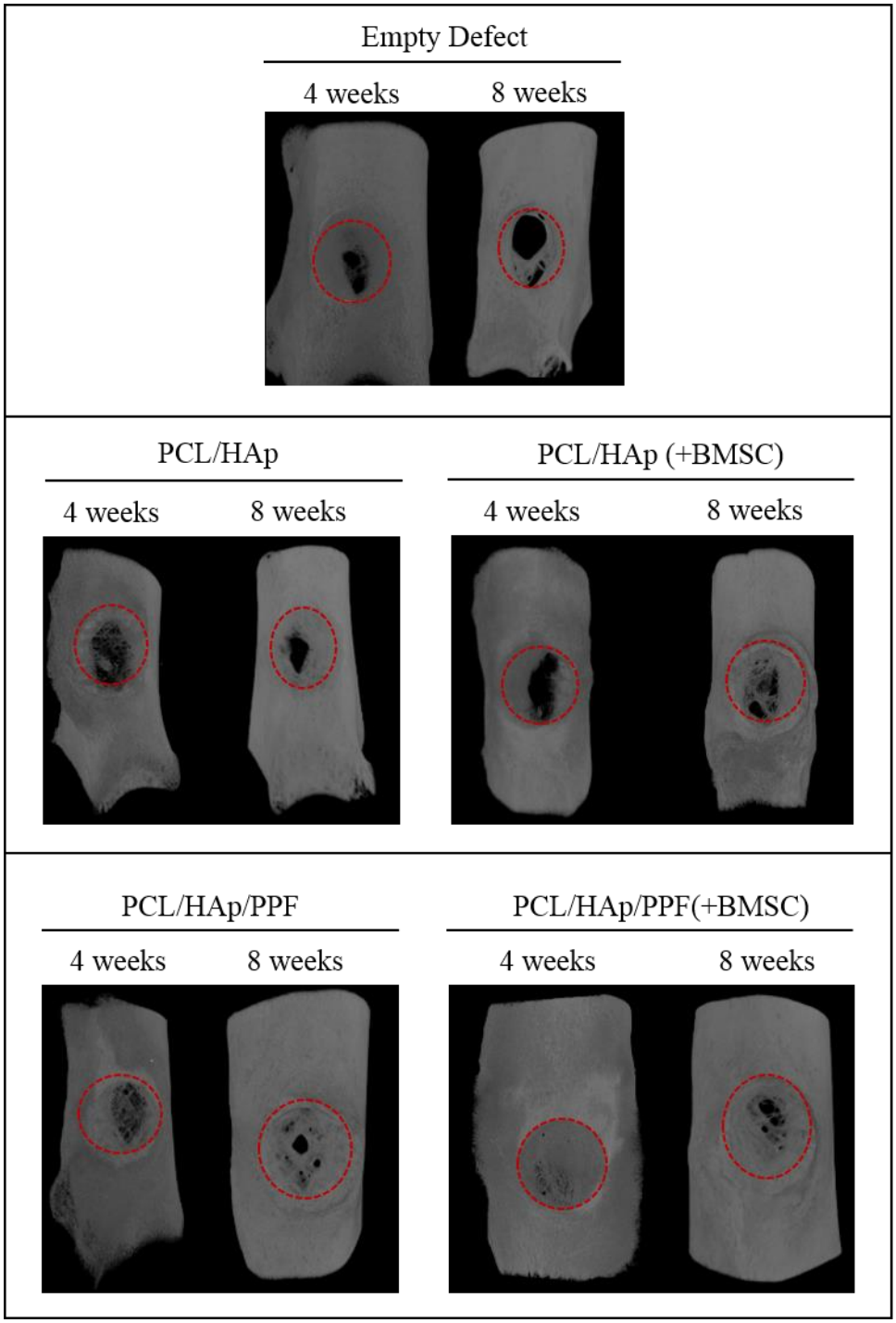

Figure 3.28. Evaluation of *in vivo* bone tissue regeneration with Micro CT images of the rabbit femurs at the end of 4 and 8 weeks after implantation.
Dotted red circles show the defect site.

The bone mineral densities (BMD) of the newly formed bone were quantitatively determined by Micro CT analysis (Figure 3.29). The difference between the BMD of the control (untreated empty defect) and the scaffold implanted defects was more distinct at the end of 8 weeks where it was significantly higher in BMSC-seeded PCL/HAp/PPF scaffolds (1.13±0.12) than other groups and was comparable to the BMD values of the healthy bone (1.31±0.05).

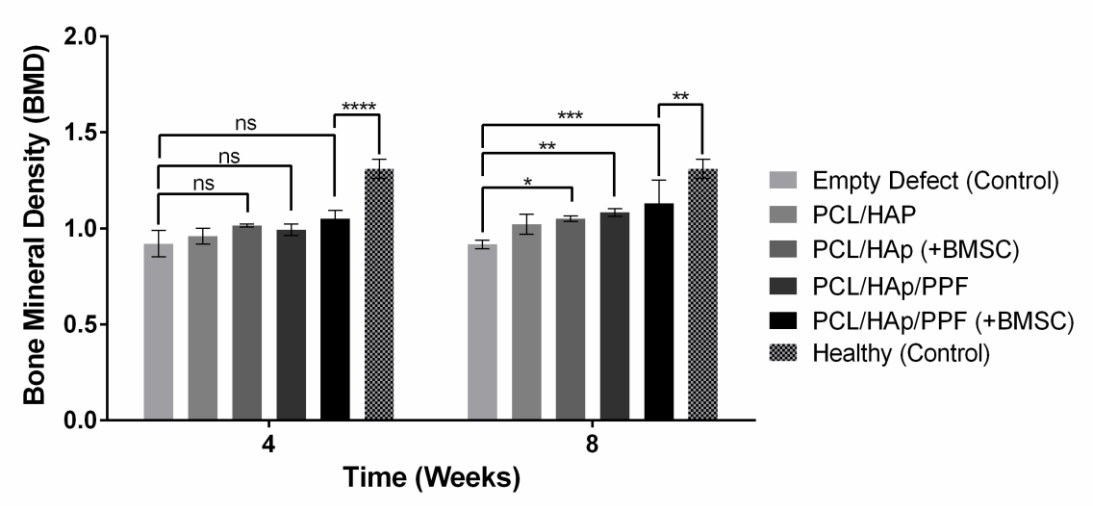

Figure 3.29. Bone mineral density (BMD) values of the the newly formed bone in untreated empty defect (control), the scaffold implanted defects and healthy bone (control). (n_{empty}=3, $n_{scaffold\ implanted}$=4). Statistical analysis was carried out by using two-way ANOVA. *p < 0.05, **p < 0.01, ***p< 0.005, ****p < 0.0001, and ns: not significant).

3.3.2.2. Biomechanical Analysis

Four point bending test was performed to investigate the mechanical properties of the reconstructed region of the femurs. The stiffness of the femurs with implanted scaffolds was obtained under compression and tension after 4 and 8 weeks of the implantation (Figures 3.30 and 3.31). Untreated, empty defect was used as control. The stiffness increased for all groups from 4 to 8 weeks indicates that the defects were healing as time progressed. The stiffness of the defects treated with BMSC seeded scaffolds displayed a significant increase compared to cell free scaffolds at both 4 and 8 weeks which suggests the presence of the cells enhanced the healing of the defect.

Schantz et al., (2003) compared the stiffness values of unseeded and MSC seeded PCL scaffolds implanted calvarial bones of New Zealand white rabbit and they found a significant increase in stiffness of cell seeded group. Especially BMSC seeded PCL/HAp/PPF scaffolds displayed a significantly higher stiffness at both compression and tension positions after 8 weeks of implantation (Figure 3.31). Moreover, the mechanical integrity of BMSC seeded PCL/HAp/PPF scaffold implanted femurs was as good as the healthy bone.

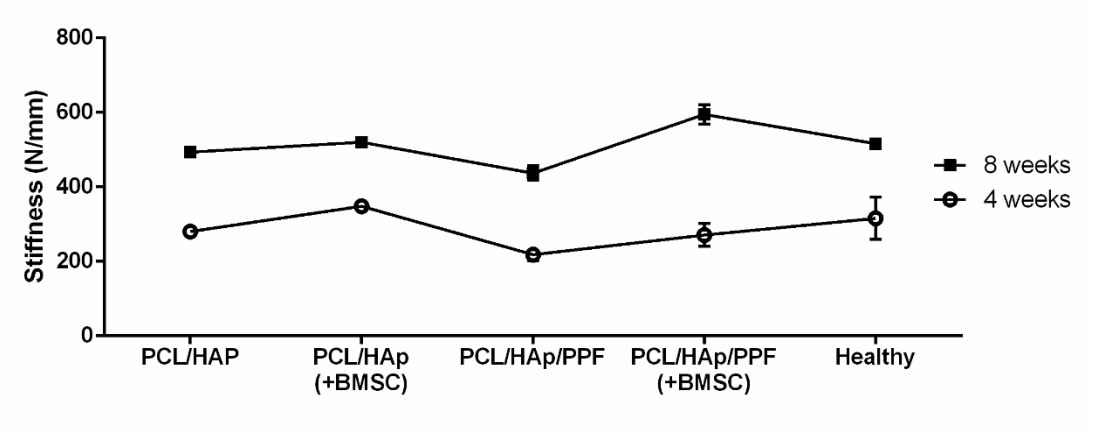

Figure 3.30. Stiffness values of the femurs at the position of compression at 4 and 8 weeks (n=4).

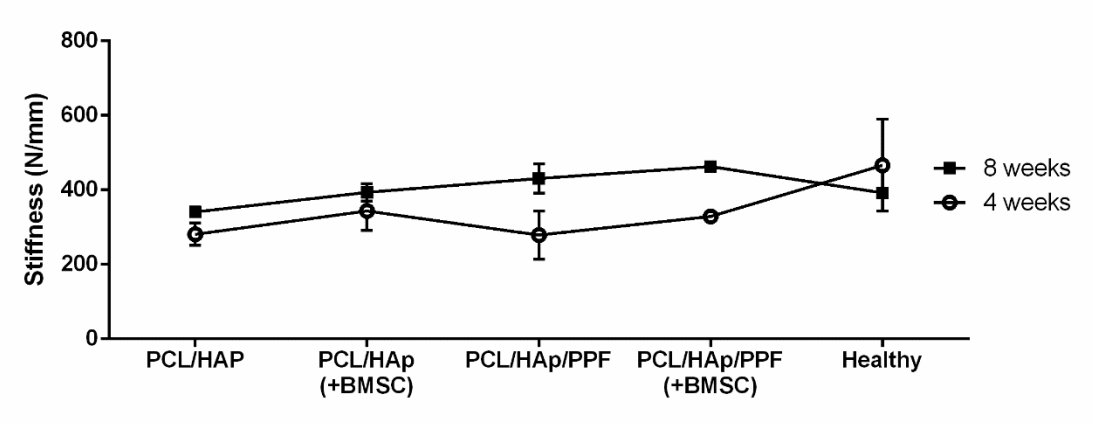

Figure 3.31. Stiffness values of the femurs at the position of tension at 4 and 8 weeks (n=4).

3.3.2.3 Histological Analysis

Histological analysis was performed to assess the progress of bone regeneration at the cellular level. Tissue sections of scaffold implanted femurs at 4 weeks post-op were stained with H&E, and Masson's trichrome (Figure 3.32).

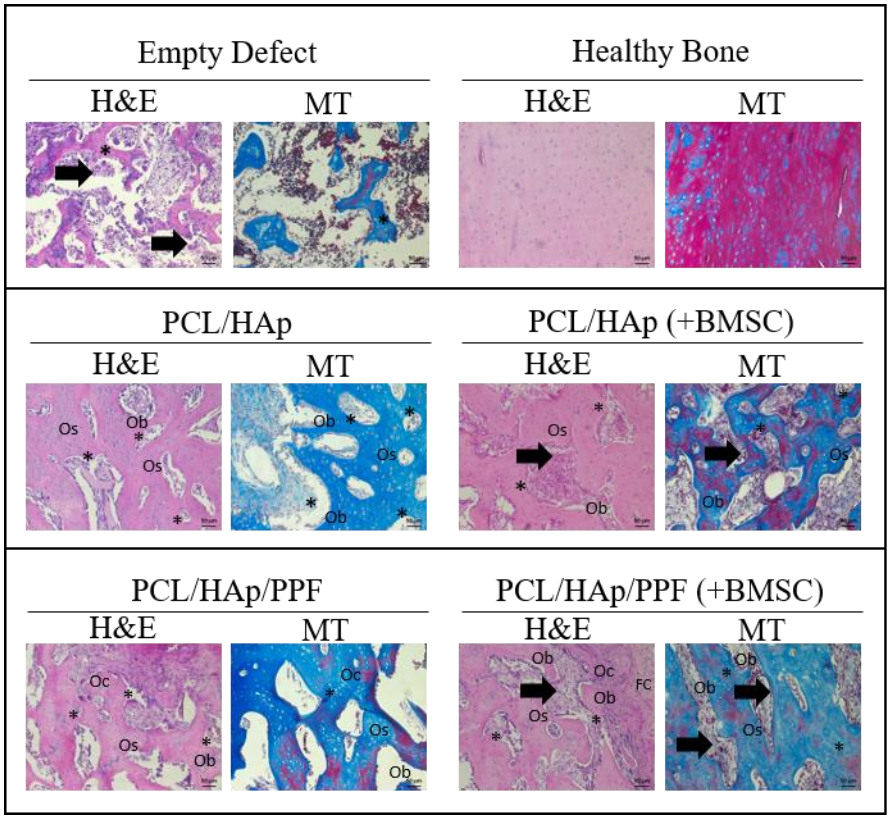

Figure 3.32. Histological study of the BMSCs seeded and unseeded PCL/HAp and PCL/HAp/PPF scaffolds (both BS 0.15) after 4 weeks of implantation.
H&E: Hematoxylin Eosin and MT: Masson's Trichrome. (*denotes new bone formations, arrows indicate foreign body giant cells and macrophages, FC: fibrous connective tissue, Ob: Osteoblasts, Os: Osteocytes, Oc: Osteoclasts).

In the control (untreated empty defect) group, there was extensive fibrous connective tissue and small amounts of new bone formation in the form of spicule and trabecula. Also, in the gap between trabecula, intense bleeding sites, and significant amount of foreign body giant cells and macrophages were observed. Contrarily, fibrous connective tissue formation and bleeding sites decreased when scaffolds were

implanted at the defect site. There were 3 main cell types in all the experimental groups: Osteoblasts, osteocytes and osteoclasts. Osteoblasts are the precursor cells and involve in the new bone formation, while osteocytes are the mature bone cells and osteoclasts have a significant role in bone removal and remodeling (Florencio-Silva et al., 2015). As it is seen in Figure 3.32, there was no significant difference between the PCL/HAp and PCL/HAp/PPF implanted defects at the cellular level. However, BMSC seeding on the scaffolds before implantation led to the formation of more intense connective tissue in the defects. In the literature, the effect of PCL based scaffolds with or without BMSCs on bone regeneration was investigated and found that seeding BMSC led to better osteochondral tissue formation compared to control group (Shao et al., 2006). Similarly, Xie et al. (2016) showed that mesenchymal stem cell derived microvesicles (MSC-MVs) incorporated alginate-PCL scaffolds displayed more new bone formation compared to alginate-PCL group without cell.

CHAPTER 4

CONCLUSION

Bone disorders affect millions of people around the world and effective bone regeneration of critical sized defects still remains a challenge. Current treatments for large bone defects resulting from osteoporosis-related fractures, trauma, tumor resections and craniofacial bone malformations rely on the use of bone grafts. Furthermore, bone graft treatments require extensive reshaping especially for the craniofacial bone deformations, and the final outcome does not always be satisfied for both patient and surgeon. Therefore, customized tissue engineered constructs with the specific shapes would be the ideal solution. In recent years, one of the most promising constructs in bone tissue engineering is 3D fabricated scaffolds due to their highly precise pore size, structure, interconnectivity, and mechanical properties.

In this study, a novel tissue engineering construct which can restore or replace the function of the defected bone was developed. This study was divided into two parts: 1) PCL based composite scaffolds fabrication by coating with HAp and HAp/PPF and investigation of *in vivo* regenerative capacity of PCL/HAp and PCL/HAp/PPF scaffolds, and 2) DPSCs loaded PCL/GelMA hybrid scaffold production and characterization.

In the first part of the study, PCL scaffolds were printed by fused deposition modelling (FDM) technique having either basic or basic shift geometry. PCL scaffolds with 0.15 mm shifting distance were chosen for further investigations due to their moderate porosity to support cell attachment, and interconnectivity of pores which enhances bone ingrowth *in vivo*. HAp and HAp/PPF incorporation onto PCL scaffold significantly enhanced the compressive modulus which was suitable to replace the human trabecular bone. *In vitro* studies were conducted with BMSCs and enhanced

cell adhesion for PCL/HAp scaffolds was observed. None of these PCL based scaffolds showed any cytotoxicity (*in vitro*), irritation (*in vivo*) or inflammation (*in vivo*). PCL/HAp and PCL/HAp/PPF scaffolds (either with BMSC seeded or unseeded) implanted into defected rabbit femurs and bone tissue regeneration was evaluated after 4 weeks and 8 weeks of implantation. Micro CT and BMD analysis revealed that BMSC seeded PCL/HAp/PPF scaffolds had significantly better tissue regeneration compared to the ones having no BMSC after 8 weeks of the implantation. Biomechanical analysis showed greater tissue integrity between BMSC seeded PCL/HAp and PCL/HAp/PPF scaffolds and femurs.

In the second part of the study, PCL/GelMA hybrid scaffolds were fabricated with 3D printing technique to obtain homogenous cell distribution in a mechanically strong construct for bone tissue replacement. Compressive modulus of the hybrid construct (102±10 MPa) was in the range of the compressive modulus of the human trabecular bone (50-100 MPa). DPSCs were loaded GelMA and printed between the PCL fibers with high cell viability after printing. DPSCs in the hydrogel part of the scaffold deposited Ca and P ions which shows the differentiation of the cells towards to osteogenic lineage.

In conclusion, hybrid structures of PCL and cell loaded GelMA hold promise to be used in bone tissue engineering applications. PCL/HAp and PCL/HAp/PPF composite scaffolds have great potential to go into clinical trials for bone defects.

REFERENCES

Akkouch, A., Zhang, Z., and Rouabhia, M. (2014). Engineering bone tissue using human dental pulp stem cells and an osteogenic collagen-hydroxyapatite-poly(l-lactide-co-ε-caprolactone) scaffold. Journal of Biomaterials Applications, 28(6), 922-936.

An, S., Ling, J., Gao, Y., and Xiao, Y. (2012). Effects of varied ionic calcium and phosphate on the proliferation, osteogenic differentiation and mineralization of human periodontal ligament cells *in vitro*. Journal of Periodontal Research, 47(3), 374-382.

Anderson, H. C., Sipe, J. B., Hessle, L., Dhamyamraju, R., Atti, E., Camacho, N. P., and Millán, J. L. (2004). Impaired calcification around matrix vesicles of growth plate and bone in alkaline phosphatase-deficient mice. The American Journal of Pathology, 164(3), 841-847.

Arima, Y., and Iwata, H. (2007). Effect of wettability and surface functional groups on protein adsorption and cell adhesion using well-defined mixed self-assembled monolayers. Biomaterials, 28(20), 3074-3082.

Arun Kumar, R., Sivashanmugam, A., Deepthi, S., Iseki, S., Chennazhi, K. P., Nair, S. V., and Jayakumar, R. (2015). Injectable chitin-poly(ε-caprolactone)/nanohydroxyapatite composite microgels prepared by simple regeneration technique for bone tissue engineering. ACS Applied Materials and Interfaces, 7(18), 9399-9409.

Athanasiou, K. A., Zhu, C. F., Lanctot, D. R., Agrawal, C. M., and Wang, X. (2000). Fundamentals of biomechanics in tissue engineering of bone. Tissue Engineering, 6(4), 361-381.

Bahcecioglu, G., Hasirci, N., Bilgen, B., and Hasirci, V. (2019). Hydrogels of agarose, and methacrylated gelatin and hyaluronic acid are more supportive for *in vitro*

meniscus regeneration than three dimensional printed polycaprolactone scaffolds. International Journal of Biological Macromolecules, 122, 1152-1162.

Baheiraei, N., Nourani, M. R., Mortazavi, S. M. J., Movahedin, M., Eyni, H., Bagheri, F., and Norahan, M. H. (2018). Development of a bioactive porous collagen/β-tricalcium phosphate bone graft assisting rapid vascularization for bone tissue engineering applications. Journal of Biomedical Materials Research Part A, 106(1), 73-85.

Bao, C., Chong, M. S., Qin, L., Fan, Y., Teo, E. Y., Sandikin, D., Choolani M., and Chan, J. K. Y. (2019). Effects of tricalcium phosphate in polycaprolactone scaffold for mesenchymal stem cell-based bone tissue engineering. Materials Technology, 1-7.

Blaeser, A., Duarte Campos, D. F., Puster, U., Richtering, W., Stevens, M. M., and Fischer, H. (2016). Controlling shear stress in 3D bioprinting is a key factor to balance printing resolution and stem cell integrity. Advanced Healthcare Materials, 5(3), 326-333.

Bose, S., Roy, M., and Bandyopadhyay, A. (2012). Recent advances in bone tissue engineering scaffolds. Trends in Biotechnology, 30(10), 546-554.

Bruyas, A., Lou, F., Stahl, A. M., Gardner, M., Maloney, W., Goodman, S., and Yang, Y. P. (2018). Systematic characterization of 3D-printed PCL/β-TCP scaffolds for biomedical devices and bone tissue engineering: Influence of composition and porosity. Journal of Materials Research, 33(14), 1948-1959.

Buyuksungur, S., Tanir, T. E., Buyuksungur, A., Bektas, E. I., Kose, G. T., Yucel, D., Beyzadeoglu T., Cetinkaya E., Yenigun C., Tönük E., Hasirci, V., and Hasirci, N. (2017). 3D printed poly(ε-caprolactone) scaffolds modified with hydroxyapatite and poly(propylene fumarate) and their effects on the healing of rabbit femur defects. Biomaterials Science, 5(10), 2144-2158.

Byambaa, B., Annabi, N., Yue, K., Trujillo-de Santiago, G., Alvarez, M. M., Jia, W., Kazemzadeh-Narbat M., Shin R. S., Tamayol A., and Khademhosseini, A. (2017). Bioprinted osteogenic and vasculogenic patterns for engineering 3D bone tissue. Advanced Healthcare Materials, 6(16), 1700015.

Caplan, A. I. (2009). Why are MSCs therapeutic? New data: new insight. The Journal of Pathology, 217(2), 318-324.

Celikkin, N., Mastrogiacomo, S., Jaroszewicz, J., Walboomers, X. F., and Swieszkowski, W. (2018). Gelatin methacrylate scaffold for bone tissue engineering: The influence of polymer concentration. Journal of Biomedical Materials Research Part A, 106(1), 201-209.

Celikkin, N., Mastrogiacomo, S., Walboomers, X. F., and Swieszkowski, W. (2019). Enhancing X-ray Attenuation of 3D Printed Gelatin Methacrylate (GelMA) Hydrogels Utilizing Gold Nanoparticles for Bone Tissue Engineering Applications. Polymers, 11(2), 367.

Chen, C. H., Hsieh, M. F., Ho, Y. N., Huang, C. M., Lee, J. S., Yang, C. Y., and Chang, Y. (2011). Enhancement of catechin skin permeation via a newly fabricated mPEG-PCL-graft-2-hydroxycellulose membrane. Journal of Membrane Science, 371(1-2), 134-140.

Chen, Q., Shou, P., Zhang, L., Xu, C., Zheng, C., Han, Y., Li W., Huang Y., Zhang X., Shao C., Roberts, A. I., Rabson A. B., Ren G., Zhang Y. Wang Y., Denhard D. T., and Shi Y. (2014). An osteopontin-integrin interaction plays a critical role in directing adipogenesis and osteogenesis by mesenchymal stem cells. Stem Cells, 32(2), 327-337.

Chen, W., Zhou, H., Tang, M., Weir, M. D., Bao, C., and Xu, H. H. (2011). Gas-foaming calcium phosphate cement scaffold encapsulating human umbilical cord stem cells. Tissue Engineering Part A, 18(7-8), 816-827.

Chimene, D., Lennox, K. K., Kaunas, R. R., and Gaharwar, A. K. (2016). Advanced bioinks for 3D printing: a materials science perspective. Annals of Biomedical Engineering, 44(6), 2090-2102.

Chuenjitkuntaworn, B., Inrung, W., Damrongsri, D., Mekaapiruk, K., Supaphol, P., and Pavasant, P. (2010). Polycaprolactone/hydroxyapatite composite scaffolds: preparation, characterization, and *in vitro* and *in vivo* biological responses of human primary bone cells. Journal of Biomedical Materials Research Part A, 94(1), 241-251.

Chuenjitkuntaworn, B., Supaphol, P., Pavasant, P., and Damrongsri, D. (2010). Electrospun poly(L-lactic acid)/hydroxyapatite composite fibrous scaffolds for bone tissue engineering. Polymer International, 59(2), 227-235.

Coelho, M. J., and Fernandes, M. H. (2000). Human bone cell cultures in biocompatibility testing. Part II: effect of ascorbic acid, β-glycerophosphate and dexamethasone on osteoblastic differentiation. Biomaterials, 21(11), 1095-1102.

Dadsetan, M., Guda, T., Runge, M. B., Mijares, D., LeGeros, R. Z., LeGeros, J. P., Silliman T. D., Lu L., Wenke J. C., Brown Baer R. B., and Yaszemski, M. J. (2015). Effect of calcium phosphate coating and rhBMP-2 on bone regeneration in rabbit calvaria using poly (propylene fumarate) scaffolds. Acta Biomaterialia, 18, 9-20.

Daly, A. C., Cunniffe, G. M., Sathy, B. N., Jeon, O., Alsberg, E., and Kelly, D. J. (2016). 3D bioprinting of developmentally inspired templates for whole bone organ engineering. Advanced Healthcare Materials, 5(18), 2353-2362.

d'Aquino, R., Graziano, A., Sampaolesi, M., Laino, G., Pirozzi, G., De Rosa, A., and Papaccio, G. (2007). Human postnatal dental pulp cells co-differentiate into osteoblasts and endotheliocytes: a pivotal synergy leading to adult bone tissue formation. Cell Death and Differentiation, 14(6), 1162.

Deville, S., Saiz, E., and Tomsia, A. P. (2006). Freeze casting of hydroxyapatite scaffolds for bone tissue engineering. Biomaterials, 27(32), 5480-5489.

Dhivya, S., Keshav Narayan, A., Logith Kumar, R., Viji Chandran, S., Vairamani, M., and Selvamurugan, N. (2018). Proliferation and differentiation of mesenchymal stem cells on scaffolds containing chitosan, calcium polyphosphate and pigeonite for bone tissue engineering. Cell Proliferation, 51(1), e12408.

Díez-Pascual, A. M., and Díez-Vicente, A. L. (2016). Poly(propylene fumarate)/polyethylene glycol-modified graphene oxide nanocomposites for tissue engineering. ACS Applied Materials and Interfaces, 8(28), 17902-17914.

Dominici, M. L. B. K., Le Blanc, K., Mueller, I., Slaper-Cortenbach, I., Marini, F. C., Krause, D. S., Deans R., Keating A., Prokop D., and Horwitz, E. M. (2006). Minimal criteria for defining multipotent mesenchymal stromal cells. The International Society for Cellular Therapy position statement. Cytotherapy, 8(4), 315-317.

Dong, L., Wang, S. J., Zhao, X. R., Zhu, Y. F., and Yu, J. K. (2017). 3D-printed poly(ε-caprolactone) scaffold integrated with cell-laden chitosan hydrogels for bone tissue engineering. Scientific Reports, 7(1), 13412.

Dormer, N. H., Qiu, Y., Lydick, A. M., Allen, N. D., Mohan, N., Berkland, C. J., and Detamore, M. S. (2011). Osteogenic differentiation of human bone marrow stromal cells in hydroxyapatite-loaded microsphere-based scaffolds. Tissue Engineering Part A, 18(7-8), 757-767.

Duarte Campos, D. F., Blaeser, A., Buellesbach, K., Sen, K. S., Xun, W., Tillmann, W., and Fischer, H. (2016). Bioprinting organotypic hydrogels with improved mesenchymal stem cell remodeling and mineralization properties for bone tissue engineering. Advanced Healthcare Materials, 5(11), 1336-1345.

Dupont, K. M., Sharma, K., Stevens, H. Y., Boerckel, J. D., García, A. J., and Guldberg, R. E. (2010). Human stem cell delivery for treatment of large segmental bone defects. Proceedings of the National Academy of Sciences, 107(8), 3305-3310.

Einhorn, T. A., and Gerstenfeld, L. C. (2015). Fracture healing: mechanisms and interventions. Nature Reviews Rheumatology, 11(1), 45.

Ercal, P., Pekozer, G. G., and Kose, G. T. (2018). Dental stem cells in bone tissue engineering: current overview and challenges. In Cell Biology and Translational Medicine, Volume 3 (pp. 113-127). Springer, Cham.

Espalin, D., Arcaute, K., Rodriguez, D., Medina, F., Posner, M., and Wicker, R. (2010). Fused deposition modeling of patient-specific polymethylmethacrylate implants. Rapid Prototyping Journal, 16(3), 164-173.

Fang, J., Li, P., Lu, X., Fang, L., Lv, X., and Ren, F. (2019). A Strong, Tough, and Osteoconductive Hydroxyapatite Mineralized Polyacrylamide/Dextran Hydrogel for Bone Tissue Regeneration. Acta Biomaterialia.

Fawzy, Y. H., Ali, A. E. H., El-Maghraby, G. F., and Radwan, R. M. (2011). Gamma irradiation effect on the thermal stability, optical and electrical properties of acrylic acid/methyl methacrylate copolymer films. World Journal of Condensed Matter Physics, 12-18.

Fellah, B. H., Weiss, P., Gauthier, O., Rouillon, T., Pilet, P., Daculsi, G., and Layrolle, P. (2006). Bone repair using a new injectable self-crosslinkable bone substitute. Journal of Orthopaedic Research, 24(4), 628-635.

Fernández, J. M., Cortizo, M. S., and Cortizo, A. M. (2014). Fumarate/ceramic composite based scaffolds for tissue engineering: evaluation of hydrophylicity, degradability, toxicity and biocompatibility. Journal of Biomaterials and Tissue Engineering, 4(3), 227-234.

Firth, A. L., and Yuan, J. X. J. (2012). Identification of functional progenitor cells in the pulmonary vasculature. Pulmonary Circulation, 2(1), 84-100.

Fisher, J. P., Vehof, J. W., Dean, D., van der Waerden, J. P. C., Holland, T. A., Mikos, A. G., and Jansen, J. A. (2002). Soft and hard tissue response to photocrosslinked poly(propylene fumarate) scaffolds in a rabbit model. Journal of Biomedical Materials Research, 59(3), 547-556.

Florencio-Silva, R., Sasso, G. R. D. S., Sasso-Cerri, E., Simões, M. J., and Cerri, P. S. (2015). Biology of bone tissue: structure, function, and factors that influence bone cells. BioMed Research International, 2015.

Ganesh, N., Ashokan, A., Rajeshkannan, R., Chennazhi, K., Koyakutty, M., and Nair, S. V. (2014). Magnetic resonance functional nano-hydroxyapatite incorporated poly(caprolactone) composite scaffolds for *in situ* monitoring of bone tissue regeneration by MRI. Tissue Engineering Part A, 20(19-20), 2783-2794.

Gao, G., Schilling, A. F., Hubbell, K., Yonezawa, T., Truong, D., Hong, Y., Dai G., and Cui, X. (2015). Improved properties of bone and cartilage tissue from 3D inkjet-bioprinted human mesenchymal stem cells by simultaneous deposition and photocrosslinking in PEG-GelMA. Biotechnology Letters, 37(11), 2349-2355.

García-Gareta, E., Coathup, M. J., and Blunn, G. W. (2015). Osteoinduction of bone grafting materials for bone repair and regeneration. Bone, 81, 112-121.

Ge, Z., Tian, X., Heng, B. C., Fan, V., Yeo, J. F., and Cao, T. (2009). Histological evaluation of osteogenesis of 3D-printed poly-lactic-co-glycolic acid (PLGA) scaffolds in a rabbit model. Biomedical Materials, 4(2), 021001.

Geetha, C. S., Remya, N. S., Leji, K. B., Syama, S., Reshma, S. C., Sreekanth, P. J., Varma H. K., and Mohanan, P. V. (2013). Cells–nano interactions and molecular toxicity after delayed hypersensitivity, in Guinea pigs on exposure

to hydroxyapatite nanoparticles. Colloids and Surfaces B: Biointerfaces, 112, 204-212.

Ghanaati, S., Barbeck, M., Detsch, R., Deisinger, U., Hilbig, U., Rausch, V., Sader R., Unger R. E., Ziegler G., and Kirkpatrick, C. J. (2012). The chemical composition of synthetic bone substitutes influences tissue reactions *in vivo*: histological and histomorphometrical analysis of the cellular inflammatory response to hydroxyapatite, beta-tricalcium phosphate and biphasic calcium phosphate ceramics. Biomedical Materials, 7(1), 015005.

Giannotti, S., Trombi, L., Bottai, V., Ghilardi, M., D'Alessandro, D., Danti, S., Dell'Osso G., and Petrini, M. (2013). Use of autologous human mesenchymal stromal cell/fibrin clot constructs in upper limb non-unions: long-term assessment. PloS One, 8(8), e73893.

Gronthos, S., Mankani, M., Brahim, J., Robey, P. G., and Shi, S. (2000). Postnatal human dental pulp stem cells (DPSCs) *in vitro* and *in vivo*. Proceedings of the National Academy of Sciences, 97(25), 13625-13630.

Guvendiren, M., Molde, J., Soares, R. M., and Kohn, J. (2016). Designing biomaterials for 3D printing. ACS biomaterials science and engineering, 2(10), 1679-1693.

Han, D. S., Chang, H. K., Kim, K. R., and Woo, S. M. (2014). Consideration of bone regeneration effect of stem cells: comparison of bone regeneration between bone marrow stem cells and adipose-derived stem cells. Journal of Craniofacial Surgery, 25(1), 196-201.

Hasirci N, Kilic C, Kömez A, Bahcecioglu G, Hasirci V. Hydrogels in regenerative medicine. In: Gels Handbook: Fundamentals, Properties and Applications. Volume 2- Applications of Hydrogels in Regenerative Medicine. Volume Eds: Abidin MR, Gurkan UA, Edalat F. Eds: Demirci U, Khademhosseini A. World Scientific Publishing. Singapore. 2016.

Hasirci, V., and Hasirci, N. (2018). Fundamentals of Biomaterials. Springer New York.

Hasturk, O., Ermis, M., Demirci, U., Hasirci, N., and Hasirci, V. (2019). Square prism micropillars on poly(methyl methacrylate) surfaces modulate the morphology and differentiation of human dental pulp mesenchymal stem cells. Colloids and Surfaces B: Biointerfaces, 178, 44-55.

Heo, D. N., Hospodiuk, M., and Ozbolat, I. T. (2019). Synergistic interplay between human MSCs and HUVECs in 3D spheroids laden in collagen/fibrin hydrogels for bone tissue engineering. Acta Biomaterialia, 95, 348-356.

Hing, K. A. (2004). Bone repair in the twenty–first century: biology, chemistry or engineering?. Philosophical Transactions of the Royal Society of London. Series A: Mathematical, Physical and Engineering Sciences, 362(1825), 2821-2850.

Hoch, E., Schuh, C., Hirth, T., Tovar, G. E., and Borchers, K. (2012). Stiff gelatin hydrogels can be photo-chemically synthesized from low viscous gelatin solutions using molecularly functionalized gelatin with a high degree of methacrylation. Journal of Materials Science: Materials in Medicine, 23(11), 2607-2617.

Hollister, S. J. (2005). Porous scaffold design for tissue engineering. Nature Materials, 4(7), 518.

Ho-Shui-Ling, A., Bolander, J., Rustom, L. E., Johnson, A. W., Luyten, F. P., and Picart, C. (2018). Bone regeneration strategies: Engineered scaffolds, bioactive molecules and stem cells current stage and future perspectives. Biomaterials, 180, 143-162.

Intranuovo, F., Gristina, R., Brun, F., Mohammadi, S., Ceccone, G., Sardella, E., Rossi F., Tromba G., and Favia, P. (2014). Plasma Modification of PCL Porous

Scaffolds Fabricated by Solvent-Casting/Particulate-Leaching for Tissue Engineering. Plasma Processes and Polymers, 11(2), 184-195.

Inzana, J. A., Olvera, D., Fuller, S. M., Kelly, J. P., Graeve, O. A., Schwarz, E. M., Kates S. L., and Awad, H. A. (2014). 3D printing of composite calcium phosphate and collagen scaffolds for bone regeneration. Biomaterials, 35(13), 4026-4034.

Ito, Y., Hasuda, H., Kamitakahara, M., Ohtsuki, C., Tanihara, M., Kang, I. K., and Kwon, O. H. (2005). A composite of hydroxyapatite with electrospun biodegradable nanofibers as a tissue engineering material. Journal of Bioscience and Bioengineering, 100(1), 43-49.

Jayabalan, M., Shalumon, K. T., and Mitha, M. K. (2009). Injectable biomaterials for minimally invasive orthopedic treatments. Journal of Materials Science: Materials in Medicine, 20(6), 1379-1387.

Ji, K., Wang, Y., Wei, Q., Zhang, K., Jiang, A., Rao, Y., and Cai, X. (2018). Application of 3D printing technology in bone tissue engineering. Bio-Design and Manufacturing, 1(3), 203-210.

Kamel, N. A., Abou-Aiaad, T. H., Iskander, B. A., Khalil, S. K. H., Mansour, S. H., Abd-El-Messieh, S. L., and Abd-El-Nour, K. N. (2010). Biophysical studies on bone cement composites based on polyester fumarate. Journal of Applied Polymer Science, 116(2), 876-885.

Kanafi, M. M., Ramesh, A., Gupta, P. K., and Bhonde, R. R. (2014). Dental pulp stem cells immobilized in alginate microspheres for applications in bone tissue engineering. International Endodontic Journal, 47(7), 687-697.

Kang, H. W., Lee, S. J., Ko, I. K., Kengla, C., Yoo, J. J., and Atala, A. (2016). A 3D bioprinting system to produce human-scale tissue constructs with structural integrity. Nature Biotechnology, 34(3), 312.

Kang, H., Shih, Y. R. V., Hwang, Y., Wen, C., Rao, V., Seo, T., and Varghese, S. (2014). Mineralized gelatin methacrylate-based matrices induce osteogenic differentiation of human induced pluripotent stem cells. Acta Biomaterialia, 10(12), 4961-4970.

Kang, R., Luo, Y., Zou, L., Xie, L., Lysdahl, H., Jiang, X., Chen C., Bolund L., Chen B., Besenbacher F., and Bünger, C. (2014). Osteogenesis of human induced pluripotent stem cells derived mesenchymal stem cells on hydroxyapatite contained nanofibers. RSC Advances, 4(11), 5734-5739.

Kao, C. T., Lin, C. C., Chen, Y. W., Yeh, C. H., Fang, H. Y., and Shie, M. Y. (2015). Poly(dopamine) coating of 3D printed poly(lactic acid) scaffolds for bone tissue engineering. Materials Science and Engineering: C, 56, 165-173.

Kaplan, J. A., Liu, R., Freedman, J. D., Padera, R., Schwartz, J., Colson, Y. L., and Grinstaff, M. W. (2016). Prevention of lung cancer recurrence using cisplatin-loaded superhydrophobic nanofiber meshes. Biomaterials, 76, 273-281.

Karageorgiou, V., and Kaplan, D. (2005). Porosity of 3D biomaterial scaffolds and osteogenesis. Biomaterials, 26(27), 5474-5491.

Kasper, F. K., Tanahashi, K., Fisher, J. P., and Mikos, A. G. (2009). Synthesis of poly(propylene fumarate). Nature Protocols, 4(4), 518.

Khan, R. A., Beck, S., Dussault, D., Salmieri, S., Bouchard, J., and Lacroix, M. (2013). Mechanical and barrier properties of nanocrystalline cellulose reinforced poly(caprolactone) composites: Effect of gamma radiation. Journal of Applied Polymer Science, 129(5), 3038-3046.

Khanna-Jain, R., Vanhatupa, S., Vuorinen, A., Sandor, G. K., Suuronen, R., Mannerstrom, B., and Miettinen, S. (2012). Growth and differentiation of human dental pulp stem cells maintained in fetal bovine serum, human serum and serum-free/xeno-free culture media. Journal of Stem Cell Research and Therapy, 2(126), 2.

Kilic Bektas, C., and Hasirci, V. (2018). Mimicking corneal stroma using keratocyte-loaded photopolymerizable methacrylated gelatin hydrogels. Journal of tissue engineering and regenerative medicine, 12(4), e1899-e1910.

Kim, H. J., Park, I. K., Kim, J. H., Cho, C. S., and Kim, M. S. (2012). Gas foaming fabrication of porous biphasic calcium phosphate for bone regeneration. Tissue Engineering and Regenerative Medicine, 9(2), 63-68.

Kim, J. Y., Lee, T. J., Cho, D. W., and Kim, B. S. (2010). Solid free-form fabrication-based PCL/HA scaffolds fabricated with a multi-head deposition system for bone tissue engineering. Journal of Biomaterials Science, Polymer Edition, 21(6-7), 951-962.

Kim, J., Kim, I. S., Cho, T. H., Lee, K. B., Hwang, S. J., Tae, G., Noh I., Lee S. H., Park Y., and Sun, K. (2007). Bone regeneration using hyaluronic acid-based hydrogel with bone morphogenic protein-2 and human mesenchymal stem cells. Biomaterials, 28(10), 1830-1837.

Kim, K., Dean, D., Lu, A., Mikos, A. G., and Fisher, J. P. (2011). Early osteogenic signal expression of rat bone marrow stromal cells is influenced by both hydroxyapatite nanoparticle content and initial cell seeding density in biodegradable nanocomposite scaffolds. Acta Biomaterialia, 7(3), 1249-1264.

Kim, K., Yeatts, A., Dean, D., and Fisher, J. P. (2010). Stereolithographic bone scaffold design parameters: osteogenic differentiation and signal expression. Tissue Engineering Part B: Reviews, 16(5), 523-539.

Kim, M. H., Yun, C., Chalisserry, E. P., Lee, Y. W., Kang, H. W., Park, S. H., Jung W. K., Oh J., and Nam, S. Y. (2018). Quantitative analysis of the role of nanohydroxyapatite (nHA) on 3D-printed PCL/nHA composite scaffolds. Materials Letters, 220, 112-115.

Kim, S. J., Shin, Y. W., Yang, K. H., Kim, S. B., Yoo, M. J., Han, S. K., Im S. A., Won Y. D., Sung Y. B., Jeon T. S., Chang C. H., Jang J. D., Lee S. B., Kim H.

C., and Lee S. Y. (2009). A multi-center, randomized, clinical study to compare the effect and safety of autologous cultured osteoblast (Ossron™) injection to treat fractures. BMC Musculoskeletal Disorders, 10(1), 20.

Ko, H. F., Sfeir, C., and Kumta, P. N. (2010). Novel synthesis strategies for natural polymer and composite biomaterials as potential scaffolds for tissue engineering. Philosophical Transactions of the Royal Society A: Mathematical, Physical and Engineering Sciences, 368(1917), 1981-1997.

Komori, T. (2010). Regulation of bone development and extracellular matrix protein genes by RUNX2. Cell and Tissue Research, 339(1), 189.

Kuboki, Y., Jin, Q., Kikuchi, M., Mamood, J., and Takita, H. (2002). Geometry of artificial ECM: sizes of pores controlling phenotype expression in BMP-induced osteogenesis and chondrogenesis. Connective Tissue Research, 43(2-3), 529-534.

Lai, T. C., Yu, J., and Tsai, W. B. (2016). Gelatin methacrylate/carboxybetaine methacrylate hydrogels with tunable crosslinking for controlled drug release. Journal of Materials Chemistry B, 4(13), 2304-2313.

Lan, P. X., Lee, J. W., Seol, Y. J., and Cho, D. W. (2009). Development of 3D PPF/DEF scaffolds using micro-stereolithography and surface modification. Journal of Materials Science: Materials in Medicine, 20(1), 271-279.

Langer, R., and Vacanti, J. P. 1993. Tissue engineering. Science (New York, N.Y.) 260(5110), 920–926.

Lee, B. H., Shirahama, H., Cho, N. J., and Tan, L. P. (2015). Efficient and controllable synthesis of highly substituted gelatin methacrylamide for mechanically stiff hydrogels. RSC Advances, 5(128), 106094-106097.

Lee, C. H., Hajibandeh, J., Suzuki, T., Fan, A., Shang, P., and Mao, J. J. (2014). Three-dimensional printed multiphase scaffolds for regeneration of periodontium complex. Tissue Engineering Part A, 20(7-8), 1342-1351.

Lee, J. W., Ahn, G., Kim, D. S., and Cho, D. W. (2009). Development of nano-and microscale composite 3D scaffolds using PPF/DEF-HA and micro-stereolithography. Microelectronic Engineering, 86(4-6), 1465-1467.

Lee, J. W., Lan, P. X., Kim, B., Lim, G., and Cho, D. W. (2007). 3D scaffold fabrication with PPF/DEF using micro-stereolithography. Microelectronic Engineering, 84(5-8), 1702-1705.

Lee, K. W., Wang, S., Yaszemski, M. J., and Lu, L. (2008). Physical properties and cellular responses to crosslinkable poly(propylene fumarate)/hydroxyapatite nanocomposites. Biomaterials, 29(19), 2839-2848.

Lendeckel, S., Jödicke, A., Christophis, P., Heidinger, K., Wolff, J., Fraser, J. K., Hedrick M. H., Berthold L. and Howaldt, H. P. (2004). Autologous stem cells (adipose) and fibrin glue used to treat widespread traumatic calvarial defects: case report. Journal of Cranio-Maxillofacial Surgery, 32(6), 370-373.

Li, C., Vepari, C., Jin, H. J., Kim, H. J., and Kaplan, D. L. (2006). Electrospun silk-BMP-2 scaffolds for bone tissue engineering. Biomaterials, 27(16), 3115-3124.

Li, D., and Xia, Y. (2004). Electrospinning of nanofibers: reinventing the wheel?. Advanced Materials, 16(14), 1151-1170.

Li, J., Chen, M., Fan, X., and Zhou, H. (2016). Recent advances in bioprinting techniques: approaches, applications and future prospects. Journal of Translational Medicine, 14(1), 271.

Li, Y. C., Zhang, Y. S., Akpek, A., Shin, S. R., and Khademhosseini, A. (2016). 4D bioprinting: the next-generation technology for biofabrication enabled by stimuli-responsive materials. Biofabrication, 9(1), 012001.

Lian, J. B., Stein, G. S., Van Wijnen, A. J., Stein, J. L., Hassan, M. Q., Gaur, T., and Zhang, Y. (2012). MicroRNA control of bone formation and homeostasis. Nature Reviews Endocrinology, 8(4), 212.

Lindahl, A., Brittberg, M., Gibbs, D., Dawson, J. I., Kanczler, J., Black, C., Tare R., Oreffo, R. O. (2015). Cartilage and bone regeneration. In Tissue Engineering (529-582). Academic Press.

Liu, X., and Ma, P. X. (2004). Polymeric scaffolds for bone tissue engineering. Annals of Biomedical Engineering, 32(3), 477-486.

Luo, Y., Dolder, C. K., Walker, J. M., Mishra, R., Dean, D., and Becker, M. L. (2016). Synthesis and biological evaluation of well-defined poly(propylene fumarate) oligomers and their use in 3D printed scaffolds. Biomacromolecules, 17(2), 690-697.

Malikmammadov, E., Tanir, T. E., Kiziltay, A., Hasirci, V., and Hasirci, N. (2018). PCL-TCP wet spun scaffolds carrying antibiotic-loaded microspheres for bone tissue engineering. Journal of Biomaterials Science, Polymer Edition, 29(7-9), 805-824.

Mangano, C., Piattelli, A., Mangano, A., Mangano, F., Mangano, A., Iezzi, G., Borgers F. L., d'Avila S., and Shibli, J. A. (2009). Combining scaffolds and osteogenic cells in regenerative bone surgery: a preliminary histological report in human maxillary sinus augmentation. Clinical Implant Dentistry and Related Research, 11, e92-e102.

Maraldi, T., Riccio, M., Pisciotta, A., Zavatti, M., Carnevale, G., Beretti, F., La Sala G. B., Molta A., and De Pol, A. (2013). Human amniotic fluid-derived and dental pulp-derived stem cells seeded into collagen scaffold repair critical-size bone defects promoting vascularization. Stem Cell Research and Therapy, 4(3), 53.

Marcacci, M., Kon, E., Moukhachev, V., Lavroukov, A., Kutepov, S., Quarto, R., Mastrogiacomo M., and Cancedda, R. (2007). Stem cells associated with macroporous bioceramics for long bone repair: 6-to 7-year outcome of a pilot clinical study. Tissue Engineering, 13(5), 947-955.

Marolt, D. (2015). Tissue Engineering Craniofacial Bone Products. In Stem Cell Biology and Tissue Engineering in Dental Sciences (pp. 521-539). Academic Press.

Marsell, R., and Einhorn, T. A. (2011). The biology of fracture healing. Injury, 42(6), 551-555.

Martin, I., Wendt, D., Heberer, M. (2004). The role of bioreactors in tissue engineering. Trends in Biotechnology, 22(2), 80-86.

Martins, A. M., Pham, Q. P., Malafaya, P. B., Sousa, R. A., Gomes, M. E., Raphael, R. M., Kasper F. K., Reis R. L., and Mikos, A. G. (2009). the role of lipase and a-amylase in the degradation of starch/poly(e-caprolactone) fiber meshes and the osteogenic differentiation of cultured marrow stromal cells. Tissue Engineering: Part A, 15(2).

Meijer, G. J., de Bruijn, J. D., Koole, R., and van Blitterswijk, C. A. (2008). Cell based bone tissue engineering in jaw defects. Biomaterials, 29(21), 3053-3061.

Mesimäki, K., Lindroos, B., Törnwall, J., Mauno, J., Lindqvist, C., Kontio, R., Miettinen S., and Suuronen, R. (2009). Novel maxillary reconstruction with ectopic bone formation by GMP adipose stem cells. International Journal of Oral and Maxillofacial Surgery, 38(3), 201-209.

Mirab, F., Eslamian, M., and Bagheri, R. (2018). Fabrication and characterization of a starch-based nanocomposite scaffold with highly porous and gradient structure for bone tissue engineering. Biomedical Physics and Engineering Express, 4(5), 055021.

Mochizuki, M., and Hirami, M. (1997). Structural effects on the biodegradation of aliphatic polyesters. Polymers for Advanced Technologies, 8(4), 203-209.

Murphy, C. M., Haugh, M. G., and O'Brien, F. J. (2010). The effect of mean pore size on cell attachment, proliferation and migration in collagen–glycosaminoglycan scaffolds for bone tissue engineering. Biomaterials, 31(3), 461-466.

N. Turner, B., Strong, R., and A. Gold, S. (2014). A review of melt extrusion additive manufacturing processes: I. Process design and modeling. Rapid Prototyping Journal, 20(3), 192-204.

Nandi, S. K., Fielding, G., Banerjee, D., Bandyopadhyay, A., and Bose, S. (2018). 3D-printed β-TCP bone tissue engineering scaffolds: Effects of chemistry on *in vivo* biological properties in a rabbit tibia model. Journal of Materials Research, 33(14), 1939-1947.

Oliveira, S. M., Alves, N. M., and Mano, J. F. (2014). Cell interactions with superhydrophilic and superhydrophobic surfaces. Journal of Adhesion Science and Technology, 28(8-9), 843-863.

Olthof, M. G., Kempen, D. H., Herrick, J. L., Yaszemski, M. J., Dhert, W. J., and Lu, L. (2018). Effect of different sustained bone morphogenetic protein-2 release kinetics on bone formation in poly(propylene fumarate) scaffolds. Journal of Biomedical Materials Research Part B: Applied Biomaterials, 106(2), 477-487.

Oryan, A., Eslaminejad, M. B., Kamali, A., Hosseini, S., Moshiri, A., and Baharvand, H. (2018). Mesenchymal stem cells seeded onto tissue-engineered osteoinductive scaffolds enhance the healing process of critical-sized radial bone defects in rat. Cell and Tissue Research, 374(1), 63-81.

Ozcan, C., and Hasirci, N. (2007). Plasma modification of PMMA films: surface free energy and cell-attachment studies. Journal of Biomaterials Science, Polymer Edition, 18(6), 759-773.

Ozcan, C., Zorlutuna, P., Hasirci, V., and Hasirci, N. (2008). Influence of oxygen plasma modification on surface free energy of PMMA films and cell attachment. In Macromolecular symposia (Vol. 269, No. 1, pp. 128-137). Weinheim: Wiley-Vch Verlag.

Park, J. Y., Choi, J. C., Shim, J. H., Lee, J. S., Park, H., Kim, S. W., Doh J., and Cho, D. W. (2014). A comparative study on collagen type I and hyaluronic acid dependent cell behavior for osteochondral tissue bioprinting. Biofabrication, 6(3), 035004.

Park, S. A., Lee, S. H., and Kim, W. D. (2011). Fabrication of porous polycaprolactone/hydroxyapatite (PCL/HA) blend scaffolds using a 3D plotting system for bone tissue engineering. Bioprocess and Biosystems Engineering, 34(4), 505-513.

Parra-Torres, A. Y., Valdés-Flores, M., Orozco, L., and Velázquez-Cruz, R. (2013). Molecular aspects of bone remodeling. In Topics in osteoporosis. IntechOpen.

Paul, A., Manoharan, V., Krafft, D., Assmann, A., Uquillas, J. A., Shin, S. R., Hasan A., Hussain M. A., Gahawar A. K., and Khademhosseini, A. (2016). Nanoengineered biomimetic hydrogels for guiding human stem cell osteogenesis in three dimensional microenvironments. Journal of Materials Chemistry B, 4(20), 3544-3554.

Perez, J. R., Kouroupis, D., Li, D. J., Best, T. M., Kaplan, L., and Correa, D. (2018). Tissue engineering and cell-based therapies for fractures and bone defects. Frontiers in Bioengineering and Biotechnology, 6, 105.

Perry, B. C., Zhou, D., Wu, X., Yang, F. C., Byers, M. A., Chu, T. M. G., Hockema J. J., Woods E. J., and Goebel, W. S. (2008). Collection, cryopreservation, and

characterization of human dental pulp–derived mesenchymal stem cells for banking and clinical use. Tissue Engineering Part C: Methods, 14(2), 149-156.

Peter, S. J., Miller, S. T., Zhu, G., Yasko, A. W., and Mikos, A. G. (1998). *In vivo* degradation of a poly(propylene fumarate)/β-tricalcium phosphate injectable composite scaffold. Journal of Biomedical Materials Research, 41(1), 1-7.

Porter, J. R., Henson, A., and Popat, K. C. (2009). Biodegradable poly(ε-caprolactone) nanowires for bone tissue engineering applications. Biomaterials, 30(5), 780-788.

Porter, J. R., Ruckh, T. T., and Popat, K. C. (2009). Bone tissue engineering: a review in bone biomimetics and drug delivery strategies. Biotechnology Progress, 25(6), 1539-1560.

Posritong, S., Chavez, R. F., Chu, T. M., and Bruzzaniti, A. (2019). A Pyk2 inhibitor incorporated into a PEGDA-gelatin hydrogel promotes osteoblast activity and mineral deposition. Biomedical Materials, 14(2), 025015.

Prabhakaran, M. P., Venugopal, J., and Ramakrishna, S. (2009). Electrospun nanostructured scaffolds for bone tissue engineering. Acta Biomaterialia, 5(8), 2884-2893.

Pradel, W., and Lauer, G. (2012). Tissue-engineered bone grafts for osteoplasty in patients with cleft alveolus. Annals of Anatomy-Anatomischer Anzeiger, 194(6), 545-548.

Pradel, W., Eckelt, U., and Lauer, G. (2006). Bone regeneration after enucleation of mandibular cysts: comparing autogenous grafts from tissue-engineered bone and iliac bone. Oral Surgery, Oral Medicine, Oral Pathology, Oral Radiology, and Endodontology, 101(3), 285-290.

Qi, X., Huang, Y., Han, D., Zhang, J., Cao, J., Jin, X., Huang J., Li X., and Wang, T. (2016). Three-dimensional poly(ε-caprolactone)/hydroxyapatite/collagen

scaffolds incorporating bone marrow mesenchymal stem cells for the repair of bone defects. Biomedical Materials, 11(2), 025005.

Quarto, R., Mastrogiacomo, M., Cancedda, R., Kutepov, S. M., Mukhachev, V., Lavroukov, A., Kon E., and Marcacci, M. (2001). Repair of large bone defects with the use of autologous bone marrow stromal cells. New England Journal of Medicine, 344(5), 385-386.

Rai, B., Lin, J. L., Lim, Z. X., Guldberg, R. E., Hutmacher, D. W., and Cool, S. M. (2010). Differences between *in vitro* viability and differentiation and *in vivo* bone-forming efficacy of human mesenchymal stem cells cultured on PCL–TCP scaffolds. Biomaterials, 31(31), 7960-7970.

Ronca, A., Ambrosio, L., and Grijpma, D. W. (2013). Preparation of designed poly(D, L-lactide)/nanosized hydroxyapatite composite structures by stereolithography. Acta Biomaterialia, 9(4), 5989-5996.

Roosa, S. M. M., Kemppainen, J. M., Moffitt, E. N., Krebsbach, P. H., and Hollister, S. J. (2010). The pore size of polycaprolactone scaffolds has limited influence on bone regeneration in an *in vivo* model. Journal of Biomedical Materials Research Part A, 92(1), 359-368.

Sándor, G. K., Tuovinen, V. J., Wolff, J., Patrikoski, M., Jokinen, J., Nieminen, E., Mannerström B., Lappalainen O. P., Seppanen R., and Miettinen, S. (2013). Adipose stem cell tissue–engineered construct used to treat large anterior mandibular defect: a case report and review of the clinical application of good manufacturing practice–level adipose stem cells for bone regeneration. Journal of Oral and Maxillofacial Surgery, 71(5), 938-950.

Santos, M. I., and Reis, R. L. (2010). Vascularization in bone tissue engineering: physiology, current strategies, major hurdles and future challenges. Macromolecular Bioscience, 10(1), 12-27.

Sayin, E., Rashid, R. H., Rodríguez-Cabello, J. C., Elsheikh, A., Baran, E. T., and Hasirci, V. (2017). Human adipose derived stem cells are superior to human osteoblasts (HOB) in bone tissue engineering on a collagen-fibroin-ELR blend. Bioactive Materials, 2(2), 71-81.

Schantz, J. T., Hutmacher, D. W., Lam, C. X. F., Brinkmann, M., Wong, K. M., Lim, T. C., Chou N., Guldberg R. E. and Teoh, S. H. (2003). Repair of calvarial defects with customised tissue-engineered bone grafts II. Evaluation of cellular efficiency and efficacy *in vivo*. Tissue Engineering, 9(4, Supplement 1), 127-139.

Schuurman, W., Khristov, V., Pot, M. W., van Weeren, P. R., Dhert, W. J., and Malda, J. (2011). Bioprinting of hybrid tissue constructs with tailorable mechanical properties. Biofabrication, 3(2), 021001.

Sears, N. A., Seshadri, D. R., Dhavalikar, P. S., and Cosgriff-Hernandez, E. (2016). A review of three-dimensional printing in tissue engineering. Tissue Engineering Part B: Reviews, 22(4), 298-310.

Seyednejad, H., Gawlitta, D., Kuiper, R. V., de Bruin, A., van Nostrum, C. F., Vermonden, T., Dhert W.J., and Hennink, W. E. (2012). *In vivo* biocompatibility and biodegradation of 3D-printed porous scaffolds based on a hydroxyl-functionalized poly(ε-caprolactone). Biomaterials, 33(17), 4309-4318.

Shafiee, A., and Atala, A. (2016). Printing technologies for medical applications. Trends in Molecular Medicine, 22(3), 254-265.

Shao, N., Guo, J., Guan, Y., Zhang, H., Li, X., Chen, X., Zhou D., and Huang, Y. (2018). Development of organic/inorganic compatible and sustainably bioactive composites for effective bone regeneration. Biomacromolecules, 19(9), 3637-3648.

Shao, X., Goh, J. C., Hutmacher, D. W., Lee, E. H., and Zigang, G. (2006). Repair of large articular osteochondral defects using hybrid scaffolds and bone marrow-derived mesenchymal stem cells in a rabbit model. Tissue Engineering, 12(6), 1539-1551.

Shayesteh, Y. S., Khojasteh, A., Soleimani, M., Alikhasi, M., Khoshzaban, A., and Ahmadbeigi, N. (2008). Sinus augmentation using human mesenchymal stem cells loaded into a β-tricalcium phosphate/hydroxyapatite scaffold. Oral Surgery, Oral Medicine, Oral Pathology, Oral Radiology, and Endodontology, 106(2), 203-209.

Shim, J. H., Yoon, M. C., Jeong, C. M., Jang, J., Jeong, S. I., Cho, D. W., and Huh, J. B. (2014). Efficacy of rhBMP-2 loaded PCL/PLGA/β-TCP guided bone regeneration membrane fabricated by 3D printing technology for reconstruction of calvaria defects in rabbit. Biomedical Materials, 9(6), 065006.

Shim, K. S., Kim, S. E., Yun, Y. P., Jeon, D. I., Kim, H. J., Park, K., and Song, H. R. (2017). Surface immobilization of biphasic calcium phosphate nanoparticles on 3D printed poly(caprolactone) scaffolds enhances osteogenesis and bone tissue regeneration. Journal of Industrial and Engineering Chemistry, 55, 101-109.

Shin, H., Zygourakis, K., Farach-Carson, M. C., Yaszemski, M. J., and Mikos, A. G. (2004). Modulation of differentiation and mineralization of marrow stromal cells cultured on biomimetic hydrogels modified with Arg-Gly-Asp containing peptides. Journal of Biomedical Materials Research Part A, 69(3), 535-543.

Sinha, K. M., and Zhou, X. (2013). Genetic and molecular control of osterix in skeletal formation. Journal of Cellular Biochemistry, 114(5), 975-984.

Sitharaman, B., Shi, X., Walboomers, X. F., Liao, H., Cuijpers, V., Wilson, L. J., Mikos A. G., and Jansen, J. A. (2008). *In vivo* biocompatibility of ultra-short

single-walled carbon nanotube/biodegradable polymer nanocomposites for bone tissue engineering. Bone, 43(2), 362-370.

Sola, A., Bertacchini, J., D'Avella, D., Anselmi, L., Maraldi, T., Marmiroli, S., and Messori, M. (2019). Development of solvent-casting particulate leaching (SCPL) polymer scaffolds as improved three-dimensional supports to mimic the bone marrow niche. Materials Science and Engineering: C, 96, 153-165.

Springer, I. N., Nocini, P. F., Schlegel, K. A., Santis, D. D., Park, J., Warnke, P. H., Terheyden H., Zimmermann R., Chiarini L., Gardner K., Ferrari, F. and Wiltfang J. (2006). Two techniques for the preparation of cell-scaffold constructs suitable for sinus augmentation: steps into clinical application. Tissue Engineering, 12(9), 2649-2656.

Stein, G. S., and Lian, J. B. (1993). Molecular mechanisms mediating proliferationdifferentiation interrelationships during progressive development of the osteoblast phenotype. Endocrine Reviews, 14(4), 424-442.

Storrie, H., and Stupp, S. I. (2005). Cellular response to zinc-containing organoapatite: an *in vitro* study of proliferation, alkaline phosphatase activity and biomineralization. Biomaterials, 26(27), 5492-5499.

Suarez, J. C. M., and Mano, E. B. (2001). Characterization of degradation on gamma-irradiated recycled polyethylene blends by scanning electron microscopy. Polymer degradation and stability, 72(2), 217-221.

Sun, M., Sun, X., Wang, Z., Guo, S., Yu, G., and Yang, H. (2018). Synthesis and Properties of Gelatin Methacryloyl (GelMA) Hydrogels and Their Recent Applications in Load-Bearing Tissue. Polymers, 10(11), 1290.

Suntornnond, R., Tan, E. Y. S., An, J., and Chua, C. K. (2017). A highly printable and biocompatible hydrogel composite for direct printing of soft and perfusable vasculature-like structures. Scientific Reports, 7(1), 16902.

Tasnim, N., De la Vega, L., Kumar, S. A., Abelseth, L., Alonzo, M., Amereh, M., Joddar B., and Willerth, S. M. (2018). 3D Bioprinting Stem Cell Derived Tissues. Cellular and Molecular Bioengineering, 11(4), 219-240.

Thadavirul, N., Pavasant, P., and Supaphol, P. (2014). Development of polycaprolactone porous scaffolds by combining solvent casting, particulate leaching, and polymer leaching techniques for bone tissue engineering. Journal of Biomedical Materials Research Part A, 102(10), 3379-3392.

Thakur, T., Xavier, J. R., Cross, L., Jaiswal, M. K., Mondragon, E., Kaunas, R., and Gaharwar, A. K. (2016). Photocrosslinkable and elastomeric hydrogels for bone regeneration. Journal of Biomedical Materials Research Part A, 104(4), 879-888.

Timmer, M. D., Shin, H., Horch, R. A., Ambrose, C. G., and Mikos, A. G. (2003). *In vitro* cytotoxicity of injectable and biodegradable poly(propylene fumarate)-based networks: unreacted macromers, cross-linked networks, and degradation products. Biomacromolecules, 4(4), 1026-1033.

Tuli, R., Tuli, S., Nandi, S., Wang, M. L., Alexander, P. G., Haleem-Smith, H., Hozack W. J., Manner P. A., Danielson K. G., and Tuan, R. S. (2003). Characterization of multipotential mesenchymal progenitor cells derived from human trabecular bone. Stem Cells, 21(6), 681-693.

Turnbull, G., Clarke, J., Picard, F., Riches, P., Jia, L., Han, F., Li B., and Shu, W. (2018). 3D bioactive composite scaffolds for bone tissue engineering. Bioactive Materials, 3(3), 278-314.

Venkatesan, J., Bhatnagar, I., Manivasagan, P., Kang, K. H., and Kim, S. K. (2015). Alginate composites for bone tissue engineering: a review. International Journal of Biological Macromolecules, 72, 269-281.

Visser, J., Gawlitta, D., Benders, K. E., Toma, S. M., Pouran, B., van Weeren, P. R., Wouter J. A., Dhert J. A., and Malda, J. (2015). Endochondral bone formation

in gelatin methacrylamide hydrogel with embedded cartilage-derived matrix particles. Biomaterials, 37, 174-182.

Wang, J., Wang, L., Zhou, Z., Lai, H., Xu, P., Liao, L., and Wei, J. (2016). Biodegradable polymer membranes applied in guided bone/tissue regeneration: a review. Polymers, 8(4), 115.

Wang, M. O., Etheridge, J. M., Thompson, J. A., Vorwald, C. E., Dean, D., and Fisher, J. P. (2013). Evaluation of the *in vitro* cytotoxicity of cross-linked biomaterials. Biomacromolecules, 14(5), 1321-1329.

Wang, S., Lu, L., and Yaszemski, M. J. (2006). Bone-tissue-engineering material poly(propylene fumarate): correlation between molecular weight, chain dimensions, and physical properties. Biomacromolecules, 7(6), 1976-1982.

Wang, X., Xu, S., Zhou, S., Xu, W., Leary, M., Choong, P., Qian M., Bran M., and Xie, Y. M. (2016). Topological design and additive manufacturing of porous metals for bone scaffolds and orthopaedic implants: A review. Biomaterials, 83, 127-141.

Wang, X., Xu, S., Zhou, S., Xu, W., Leary, M., Choong, P., Qian M., Brandt M., and Xie, Y. M. (2016). Topological design and additive manufacturing of porous metals for bone scaffolds and orthopaedic implants: A review. Biomaterials, 83, 127-141.

Webb, P. A. (2000). A review of rapid prototyping (RP) techniques in the medical and biomedical sector. Journal of Medical Engineering and Technology, 24(4), 149-153.

Wei, K., Li, Y., Kim, K. O., Nakagawa, Y., Kim, B. S., Abe, K., Chen G. Q., and Kim, I. S. (2011). Fabrication of nano-hydroxyapatite on electrospun silk fibroin nanofiber and their effects in osteoblastic behavior. Journal of Biomedical Materials Research Part A, 97(3), 272-280.

Wenz, A., Tjoeng, I., Schneider, I., Kluger, P. J., and Borchers, K. (2018). Improved vasculogenesis and bone matrix formation through coculture of endothelial cells and stem cells in tissue-specific methacryloyl gelatin-based hydrogels. Biotechnology and Bioengineering, 115(10), 2643-2653.

Williams, J. M., Adewunmi, A., Schek, R. M., Flanagan, C. L., Krebsbach, P. H., Feinberg, S. E., Hollister S. J., and Das, S. (2005). Bone tissue engineering using polycaprolactone scaffolds fabricated via selective laser sintering. Biomaterials, 26(23), 4817-4827.

Wu, T., Yu, S., Chen, D., and Wang, Y. (2017). Bionic design, materials and performance of bone tissue scaffolds. Materials, 10(10), 1187.

Wu, W., Liu, X., Zhou, Z., Miller, A. L., and Lu, L. (2018). Three-dimensional porous poly(propylene fumarate)-co-poly(lactic-co-glycolic acid) scaffolds for tissue engineering. Journal of Biomedical Materials Research Part A, 106(9), 2507-2517.

Xia, Y., Zhou, P., Cheng, X., Xie, Y., Liang, C., Li, C., and Xu, S. (2013). Selective laser sintering fabrication of nano-hydroxyapatite/poly-ε-caprolactone scaffolds for bone tissue engineering applications. International Journal of Nanomedicine, 8, 4197.

Xie, H., Wang, Z., Zhang, L., Lei, Q., Zhao, A., Wang, H., Li Q., Chen Z., and Zhang, W. (2016). Development of an angiogenesis-promoting microvesicle-alginate-polycaprolactone composite graft for bone tissue engineering applications. PeerJ, 4, e2040.

Xiong, Z., Yan, Y., Wang, S., Zhang, R., and Zhang, C. (2002). Fabrication of porous scaffolds for bone tissue engineering via low-temperature deposition. Scripta Materialia, 46(11), 771-776.

Yan, J., Li, J., Runge, M. B., Dadsetan, M., Chen, Q., Lu, L., and Yaszemski, M. J. (2011). Cross-linking characteristics and mechanical properties of an

injectable biomaterial composed of polypropylene fumarate and polycaprolactone co-polymer. Journal of Biomaterials Science, Polymer Edition, 22(4-6), 489-504.

Yang, X., Li, Y., He, W., Huang, Q., Zhang, R., and Feng, Q. (2018). Hydroxyapatite/collagen coating on PLGA electrospun fibers for osteogenic differentiation of bone marrow mesenchymal stem cells. Journal of Biomedical Materials Research Part A, 106(11), 2863-2870.

Yaszemski, M. J., Payne, R. G., Hayes, W. C., Langer, R. S., Aufdemorte, T. B., and Mikos, A. G. (1995). The ingrowth of new bone tissue and initial mechanical properties of a degrading polymeric composite scaffold. Tissue Engineering, 1(1), 41-52.

Yeo, M., Simon, C. G., and Kim, G. (2012). Effects of offset values of solid freeform fabricated PCL–β-TCP scaffolds on mechanical properties and cellular activities in bone tissue regeneration. Journal of Materials Chemistry, 22(40), 21636-21646.

Yilgor, P., Sousa, R. A., Reis, R. L., Hasirci, N., and Hasirci, V. (2008, August). 3D plotted PCL scaffolds for stem cell based bone tissue engineering. In Macromolecular symposia (Vol. 269, No. 1, pp. 92-99). Weinheim: Wiley-Vch Verlag.

Yuan, J., Maturavongsadit, P., Metavarayuth, K., Luckanagul, J. A., and Wang, Q. (2019). Enhanced bone defect repair by polymeric substitute fillers of multiarm polyethylene glycol-crosslinked hyaluronic acid hydrogels. Macromolecular Bioscience, 1900021.

Yue, K., Trujillo-de Santiago, G., Alvarez, M. M., Tamayol, A., Annabi, N., and Khademhosseini, A. (2015). Synthesis, properties, and biomedical applications of gelatin methacryloyl (GelMA) hydrogels. Biomaterials, 73, 254-271.

Zhang, Y., Venugopal, J. R., El-Turki, A., Ramakrishna, S., Su, B., and Lim, C. T. (2008). Electrospun biomimetic nanocomposite nanofibers of hydroxyapatite/chitosan for bone tissue engineering. Biomaterials, 29(32), 4314-4322.

Zhao, D., Cui, D., Wang, B., Tian, F., Guo, L., Yang, L., Liu B., and Yu, X. (2012). Treatment of early stage osteonecrosis of the femoral head with autologous implantation of bone marrow-derived and cultured mesenchymal stem cells. Bone, 50(1), 325-330.

APPENDICES

A. L929 ALAMAR BLUE CALIBRATION CURVE

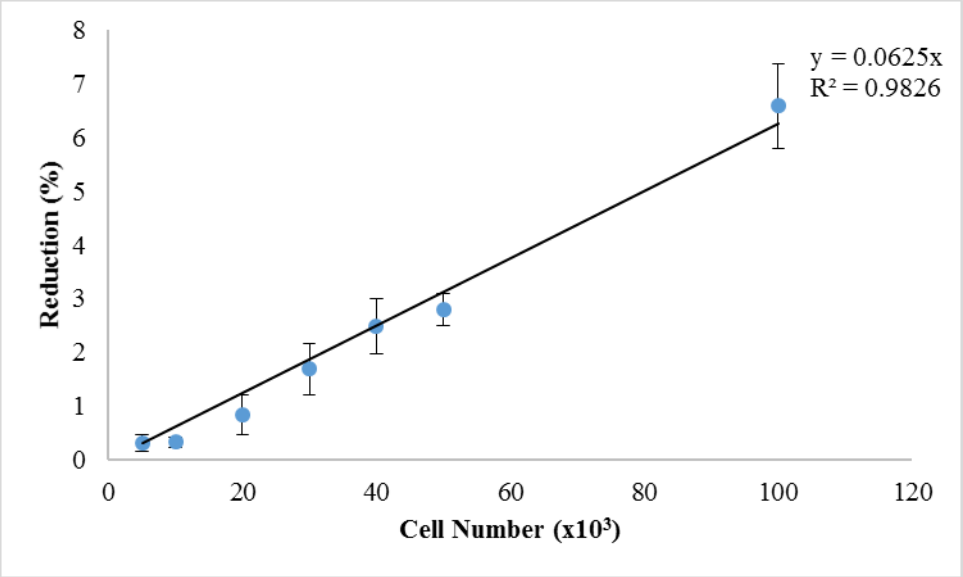

B. BMSCs ALAMAR BLUE CALIBRATION CURVE

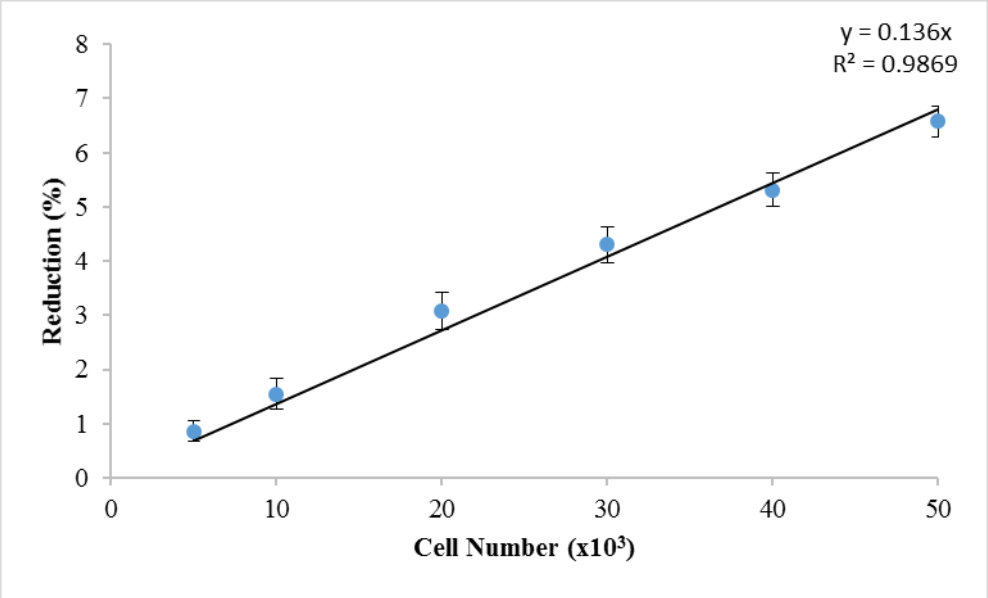

C. ALP CALIBRATION CURVE

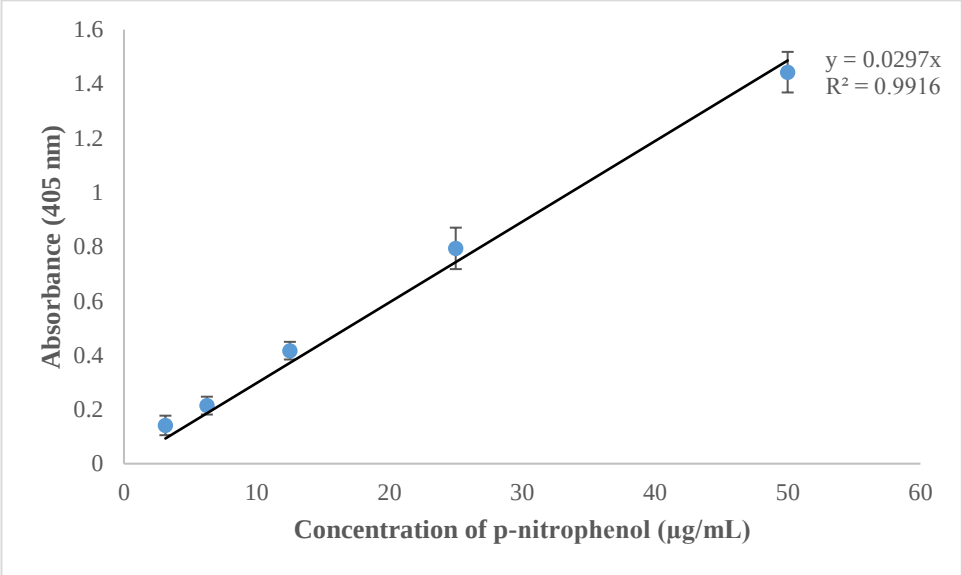

D. ETHICS COMMITTEE REPORT FOR DPSC ISOLATION

UYGULAMALI ETİK ARAŞTIRMA MERKEZİ
APPLIED ETHICS RESEARCH CENTER

ORTA DOĞU TEKNİK ÜNİVERSİTESİ
MIDDLE EAST TECHNICAL UNIVERSITY

DUMLUPINAR BULVARI 06800
ÇANKAYA ANKARA/TURKEY
T: +90 312 210 22 91
F: +90 312 210 79 59
uaam@metu.edu.tr
www.uaam.metu.edu.tr

Sayı: 28620816 / 496

10 EKİM 2017

Konu: Değerlendirme Sonucu

Gönderen: ODTÜ İnsan Araştırmaları Etik Kurulu (İAEK)

İlgi: İnsan Araştırmaları Etik Kurulu Başvurusu

Sayın Prof.Dr. Vasif HASIRCI ;

Danışmanlığını yaptığınız doktora öğrencisi Sanem BÜYÜKSUNGUR'un **"Doku Mühendisliği Yöntemi ile Hastaya Özel Ortopedik İmplant Tasarımı ve Üretimi"** başlıklı araştırmanız İnsan Araştırmaları Etik Kurulu tarafından uygun görülerek gerekli onay **2017-FEN-053** protokol numarası ile **15.10.2017 – 30.12.2018** tarihleri arasında geçerli olmak üzere verilmiştir.

Bilgilerinize saygılarımla sunarım.

Prof. Dr. Ş. Halil TURAN
Başkan V

Prof. Dr. Ayhan SOL
Üye

Prof. Dr. Ayhan Gürbüz DEMİR
Üye

BULUNAMADI
Doç. Dr. Yaşar KONDAKÇI
Üye

Doç. Dr. Zana ÇITAK
Üye

Yrd. Doç. Dr. Pınar KAYGAN
Üye

Yrd. Doç. Dr. Emre SELÇUK
Üye

E. ETHICS COMMITTEE REPORT FOR *IN VIVO* STUDIES

YEDİTEPE ÜNİVERSİTESİ

T.C. YEDİTEPE ÜNİVERSİTESİ, DENEY HAYVANLARI ETİK KURULU (YÜDHEK)

ETİK KURUL KARARI

Toplantı Tarihi	Karar No	İlgi	Proje Yürütücüsü
19.02.2013	313	04.02.2013 tarihl yazı	Prof.Dr.Nesrin HASIRCI

"Doku Mühendisliği Yöntemi ile Hastaya Özel Ortopedik İmplant Tasarımı ve Üretimi " başlıklı bilimsel araştırma Etik Kurulumuzda görüşülmüş olup, çalışmanın etik kurallara uygun olduğuna oybirliği ile karar verilmiştir.

Etik Onay Geçerlilik Süresi 2Yıl

GOREVİ	ADI SOYADI	İMZA
Başkan	Prof. Dr. M. Ece GENÇ	
Başkan Yardımcısı	Prof. Dr. Erdem YEŞİLADA	KATILMADI
Raportör	Prof. Dr. Işıl Aksan KURNAZ	
Üyc	Prof. Dr. Bayram YILMAZ	
Üye	Prof. Dr. Başar ATALAY	
Üye	Yrd.Doç.Dr.Soner DOĞAN	
Üye	Yrd. Doç. Dr. Ediz DENİZ	
Üye	Doç. Dr. C. Narter YEŞİL DAĞLAR	
Üye	Sumru KİRAZ Çı	

CURRICULUM VITAE

PERSONAL INFORMATION

Surname, Name	: Büyüksungur, Senem
Nationality	: Turkish (TC)
Date and Place of Birth	: 3 October 1986, İzmir
Phone	: +90 312 210 5189
E-mail	: senemb@metu.edu.tr

EDUCATION

Degree	Institution	Year of Graduation
PhD	METU, Biotechnology	2019
MS	METU, Biotechnology	2014
BS	Ege University, Biochemistry	2011
High School	Atatürk Anadolu High School, İzmir	2004

WORK EXPERIENCE

Year	Place	Enrollment
2019-Present	BIOMATEN, METU	Scientific Project Expert

FOREIGN LANGUAGES

Advanced English

PUBLICATIONS

Komez A., **Buyuksungur S.**, Hasirci V., Hasirci N. "Effect of chemical structure on properties of polyurethanes: Temperature responsiveness and biocompatibility", Journal of Bioactive and Compatible Polymers, 33(5), 479-497 (2018).

Buyuksungur, S., Endogan, T. T., Buyuksungur, A., Bektas, E. I., Torun, K. G., Yucel, D., Beyzadeoglu T., Cetinkaya E., Yenigun C., Tönük E., Hasirci V., Hasirci, N. (2017). 3D printed poly(ε-caprolactone) scaffolds modified with hydroxyapatite and poly(propylene fumarate) and their effects on the healing of rabbit femur defects. Biomaterials Science. DOI: 10.1039/C7BM00514H.

Polat, G. G., Akgun, O. M., Simsek, B., Saracli, M. A., **Heper, S.**, and Hasirci, V. (2016). Fluoride-Contaınıng Antı-Carıes Ph-Sensıtıve Release System and Its Effect On Streptococcus Mutans. Fluoride 49:458-466

CONFERENCE PROCEEDINGS

Buyuksungur S., Buyuksungur A., Hasirci N., Hasirci V., Kemik Doku Mühendisliğinde 3 Boyutlu PCL/GelMA Hibrit İskeleler, Biomed 2018-TR. 15-16 Aralık 2018 İstanbul. (Presented by AB)

Buyuksungur S., Endogan, T. T., Buyuksungur, A., Bektas, E. I., Torun, K. G., Yucel, D., Beyzadeoglu T., Cetinkaya E., Yenigun C., Tönük E., Hasirci V., Hasirci, N., Polymeric composites with multifunctional properties and 3D bioplotted scaffolds for tissue engineering applications, 28th European Conference on Biomaterials, 4th – 8th September 2017 Athens, Greece. (Presented by NH)

Buyuksungur A., **Buyuksungur S.**, Hasirci N., Hasirci H., 3 Boyutlu Hastaya Özel Biyobozunur Kemik İmplantlarının Tasarımı ve Karekterizasyonu, Micro CT Summer School, 30 -03 June 2016, Malatya, Turkey. (Presented by AB)

Buyuksungur A., Hasirci N., Hasirci H., **Buyuksungur S.** Biyobasım sonrası implant görüntülemesi: Mikro CT, Doku Mühendisliğinde Biyobasım: Polimerik Malzemeler, Biyoseramik Kompozitler, Doku Özdeşleri, 02 November 2016, Kocaeli University, Kocaeli, Turkey. (Presented by AB)

Buyuksungur S., Hasirci N., Hasirci V., (2015). Controlled Doxorubicin Delivery from Photoresponsive Liposomes Carrying Vitamin A Derivatives. 21st Biomaterials Science and Technology Symposium (BIOMED 2015), Antalya, Turkey. (Poster presentation)

Buyuksungur S., Buyuksungur A., Hasirci N., Hasirci V., (2015). 3D Printed, Tissue Engineered Femoral Implant Design and Production. 21st Biomaterials Science and Technology Symposium (BIOMED 2015) Antalya, Turkey. (Poster presentation)

Komez A., **Buyuksungur S.**, Hasirci V., Hasirci N., (2015). Synthesis of Polyurethane for Coating of Neurostimulator. 21st Biomaterials Science and Technology Symposium (BIOMED 2015) Antalya, Turkey. (Poster presentation)

Heper S., Hasirci N., Hasirci V., (2015). Patient-Specific Orthopedic Implant Design and Production with Tissue Engineering Method. FBPS ’15, 11th International Symposium on Frontiers in Biomedical Polymers, Riva del Garda, Italy. (Poster presentation)